Circulation Rate Modelling Of Tumbling Mill Charge Using Positron Emission Particle Tracking (PEPT)

Daramy Vandi Von Kallon
B.Eng(Hons), MScTE

Thesis submitted in fulfillment of the requirement for the degree of Doctor of Philosophy

Center for Minerals Research
Department of Chemical Engineering
University of Cape Town

May 2013

Abstract

This research is focused on developing theoretical understandings of charge circulation trends as observed in tumbling mills at different operating conditions. Of particular interest is the underlying assumptions being made by many mill models that a particle imparts energy for potential breakage only once per revolution of the mill to the charge body – that is, that the circulation rate of mill charge can be assumed to be constant irrespective of the speed at which the mill is run. The trajectory data used in this thesis is derived from positron emission particle tracking (PEPT) experiments conducted at the University of Birmingham positron imaging centre and further experiments were conducted at the iThemba LABS in Cape Town. The experimental approach is highly suited to allow the effective examination of the assumption that the grinding charge in these mills circulates at a constant rate of unity. The work reported herein has led to the development of a model linking the circulation rate of charge particles with physical mill parameters (load fraction, shoulder angle and friction) and hence showing that the circulation rate can vary with clearly measurable mill operating parameters. This finding enabled an analysis of energy distribution in the grinding environment and hence the thesis provides a better understanding of the actual trajectories followed by particles in these mills under different milling conditions.

Statement of Originality and declaration

I, Daramy Vandi Von Kallon, do hereby:

(a) grant the University of Cape Town free license to reproduce this thesis in whole or in part, for the purpose of research;

(b) declare that:

(i) this thesis is my own unaided work, both in concept and execution, and that apart from the normal guidance from my supervisors, I have received no assistance:

(ii) neither the substance nor any part of this thesis has been submitted in the past, or is being, or is to be submitted for a degree at this University or at any other university:

Sign: ……

Date: ……

List of Publications

D.V.V. Kallon, I. Govender and A.N. Mainza. Circulation rate modelling of mill charge using position emission particle tracking. *Minerals engineering*, 24 (2011), pp. 282 – 289.

D.V.V. Kallon, I. Govender and A.N. Mainza. Formulation of grinding media models and their implications for breakage energy assumptions in grinding media mills. *Minerals engineering*. Currently under peer review.

Acknowledgement

It is by the kind grace and mercy of Almighty Allah that I am able to submit this thesis. Praise be to Allah, Cherisher and Sustainer of the worlds. Amen.

The subject of this thesis was originally initiated by Roger Leighton and the thesis was supervised by Dr. Indresan Govender and Associate Professor Aubrey Mainza. Many thanks go to the three of them.

To the staff of the CMR, CERECAM, Birmingham University Positron Imaging Centre and at PEPT Cape Town, I want to say a very big thank you for the use of facilities and the good comradeship.

There is a special place in my heart for my parents Alhaji D. M. Kallon (late) and Mrs. Salma Kallon. For the love, affection and guidance I received from you has brought me to this point in my life and I want to say thank you, thank you and thank you again. May Allah continue to shower you with His mercy and forgiveness and ordain for you a blessed sojourn in this life and the here-after.

The memory of my beloved grandmother, Yea Suba Rogers (late), lives on even eight years after you passed away. You were the first human being I recognized in my life and you will always have that special place in my heart. Thank you for the love. We shall meet again grandma. Till then may Allah grant you eternal resting place in Paradise.

To my siblings Ali, Waliya Baji, Delordson, Tommy, Jamilatu, Mujiru, Kadie I, Kadie II and last but not the least Fiema thank you all for the unity, harmony, peace and joy of being around each other.

To my family and friends the world over, I will always remember the enormous contributions you have all made to my life. You defined who I am today and I want to say thank you from the bottom of my heart.

To my wife, Mrs Ifeoma Massah Kallon, let me say you are the love of my heart and I will forever remember the years you have devoted to me. You made me find love and I will forever be grateful to you. Thank you, your husband loves you even more.

And to my little darling, baby Halimatul, I want to say how much joy and happiness you brought into my life. You gave me reason not only to live but to fight for a better future for you and all those who will come after you. Thank you my baby for being there for Daddy and Daddy love you always.

Dedication

This thesis is dedicated to my Father, the late Alhaj Delordson Moinina Kallon (Sn) and my brother-in-Law, the late Maulana Yousuf Khalid Dowie. May Allah grant them perfect resting place in Paradise. Amen.

Table of Contents

Abstract ……..i
Statement of originality ……ii
List of publications ……..iii
Acknowledgement ……iv
Dedication ……vi
Contents ……...vii
List of figures ……xi
List of tables ……xv

Chapter One: Introduction …… 1
1.0 Introduction …… 1
1.1 Project Aim …… 3
1.2 Key Questions …… 4
1.3 Hypothesis …… 5
1.4 Objectives …… 7
1.5 Methodology …… 9
1.6 Justification …….. 10
1.7 Conclusion ……..11

Chapter Two: Literature Review ……...12
2.0 Introduction ……...12
2.1 Grinding mill charge in tumbling mills .....……...13
2.2 Tumbling mills ……...15
2.2.1 Ball mills ……...15
2.2.2 Rod mills …… ..16
2.2.3 AG/SAG mills …… ..17
2.3 Comminution of tumbling mills …… ..19
2.3.1 Optimization of tumbling mills ……20

2.3.2 Modelling of tumbling mills ...……22
2.4 Positron Emission Particle Tracking (PEPT) …..……24
2.5 Tumbling mill charge motion ..……..…….. 26
2.5.1 Circulation rate ..……..…….. 26
2.5.2 The angle of repose ..……..……...28
2.6 Review of selected papers on charge motion, grinding regions and PEPT …...……...30

Chapter Three: A Particle Tracking Technique ……...50
3.0 Introduction ……...50
3.1 X-ray vision systems ……...52
3.1.1 Advantages of X-ray vision systems ……...53
3.1.2 Disadvantages of X-ray vision systems ……..54
3.2 Positron Emission Tomography (PET) ……...54
3.3 Positron Emission Particle Tracking (PEPT) ……57
3.3.1 The Birmingham Positron Camera ……...57
3.3.2 Labeling tracer particles ……...60
3.3.3 Particle tracking algorithm ……...62
3.3.4 Data processing ……...64
3.3.5 The ergodic theory ……...64
3.3.6 Advantages of PEPT ……...70
3.3.7 Disadvantages of PEPT ……...70
3.4 PEPT at iThemba labs ……...70

Chapter Four: A Particle Tracking Technique ……...73
4.0 Introduction ……...73
4.1 The Experimental Rig ……...73
4.2 PEPT Experiments at University Of Birmingham (UB) ……75
4.2.1 Experimental Matrix ……...75
4.2.2 The Experimental Mill Speed……...76
4.2.3 The Mill Load……...77

4.2.4 Torque Sensor Calibration……78
4.2.4 Trajectory Data……79
4.3 Experiments at PEPT Cape Town……...85
4.3.1 Experimental Matrix……86

Chapter five: Analysis of the Experimental Data…….88
5.0 Introduction……..88
5.1 Operational Definitions Used……..91
5.1.1 Mill Speed……92
5.1.2 Load fraction……93
5.1.3 Circulation Rate……94
5.1.4 The Equilibrium Surface and the Centre of Circulation (CoC) ……107
5.1.5 Centre of Mass (CoM)……109
5.1.6 Angle of Repose (AoR)……..110
5.1.7 Toe and Shoulder (TaS)……..113
5,2 Conclusion……116

Chapter six: Tumbling Charge Motion……...117
6.0 Introduction……117
6.1 Charge Motion in the 2D Plane……118
6.1.1 Slipping Motion……..118
6.1.2 Cascading Motion……...119
6.1.3 Cataracting Motion……127
6.2 Summary of Tumbling Charge Motion……129

Chapter seven: Modelling the Circulation Rate of Tumbling Mill Charge…….131
7.0 Introduction……131
7.1 Transition Zones Revisited……132

7.1.1 Slipping to Cascading Transition……132
7.1.2 Cascading to Cataracting Transition……...142
7.2 Two-Cycle Description of Tumbling Charge Motion……...147
7.2.1 The Oscillating Cycle ($O - S^3$)……...147
7.2.2 The Circulating Cycle ($C - RC^3$)……150
7.3 A Circulation Rate Model……..152
7.4 Conclusion……157

Chapter eight: Energy Distribution in the Grinding Environment of Tumbling Mills from a continuum approach ……...159
8.0 Introduction……159
8.1 Review of Power Draw Models……161
8.1.1 The Morrell Power Draw Model……161
8.1.2 The Heuristic Power Draw Model……..166
8.2 The CoC and the Quasi-plug Flow Region……168
8.3 The Mechanical Energy Model……..169
8.4 A continuum Based Energy Model of Tumbling Mills……174
8.4.1 The Continuity Equation……178
8.4.2 The Momentum Equation……...179
8.4.3 The Energy Model……..182

Chapter nine: Conclusions and Recommendations……188
9.0 Introduction……188
9.1 Recommendations……..189
9.1.1 Fourier Methods……..189
9.1.2 The Centre of Circulation (CoC) Location……189
9.1.3 The Departure Shoulder Angle……...190
9.1.4 Power Draw……191
9.2 Conclusion……191

References ……..196

Appendix A: Glossary ……..212

Appendix B: Nomenclauture ……..215

Appendix C: Data processing ……..217

\

List of Figures

Number	Description	Page No.
1	Ball mill with cut away section showing feed and discharge ends	16
2	Rod mill with rotating drum causing friction and attrition between rods and ore particles	17
3.	SAG mill	19
4	Particle tracking system in PEPT	25
5	The relation between critical speed and ball-containing fraction	33
6	Schematic of the bed cross-section and moment balance around the cylinder axis	37
7	Force balance around particles in different quadrants of the cylinder cross-section	40
8	Grinding regions in rotary grinding mills	46
9	The biplaner angioscope at the University of Cape Town, be Govender [23]	52
10	The positron camera at the PEPT unit, University Of Birmingham	59
11	Triangulation – events recorded by scattered and random pairs rejected by algorithm	63
12	The ECAT 'EXACT3D' PET camera at PEPT Cape Town consisting of 48 rings of 576 BGO detector elements.	71
13	Experimental mill employed in positron emission particle tracking experiments	74
14	Torque sensor on shaft connecting mill and motor. UB.	75
15	Rosin-Rammler fit to size distribution of blue stone employed in PEPT experiments of tumbling mills.	78

16	Torque sensor calibration	79
17	Illustration of the tracer particles employed in the PEPT experimental work.	80
18	Positron emitting glass bead employed as location marker in tracing out the mill shell	81
19	Front view trajectory field of a 4mm rock particle in a mill charged with a 35% dry load. Lifter bars are 19mm high, 20mm wide with a 60° face angle.	82
20	Front view trajectory field of a 2mm rock particle in a mill charged with a 15% dry load. Lifter bars are 5mm high, 20mm wide with a 90° face angle.	83
21	Front view trajectory field of a 1mm particle in a mill charged with a 40% loading and 30% solids. Lifter bars are 5mm high, 20mm wide with a 90° face angle	84
22	The experimental mill in the ECAT EXERT3D camera system at PEPT Cape Town	86
23	A typical circulation path followed by the ball, showing the various distinct zones	90
24	Setting the mill speed with an optical switch	93
25	Load fractions determined by mass	94
26	Variation of circulation rate with experimental mill speed	99
27	Variation of circulation rate with mill fraction	100
28	Power spectral plots showing circulation rates obtained from the first peak or an average of nearer peaks	104
29	Power spectral plots showing circulation rates obtained from the first peak or an average of nearer peaks	105
30	Plot of power spectral peaks (harmonics or circulation rates) as a function of mill speed.	107
31	(a) Angular location of the CoC, Govender [23], (b) relationship between mill speed and the repose angle	112

32	Identifying the toe and shoulder regions	113
33	Variation of departure shoulder with mill speed	115
34	The upper , mean and lower angles of repose during charge slumping drawn after Mellmann [15]	120
35	Radial location of the (CoC) at low mill speeds.	124
36	Occurrence of the S-shape in rotary mills, Tabelet et al [19]	126
37	A hollow space forms in the charge while the charge cascades within speed range 40% to 65%.	127
38	Cataracting motion occurred between speed range 70% to 85%	128
39	Partial centrifuging seen occurring at around 90% mill speed	128
40	Delineating tumbling charge motion	130
41	Illustration of the mill geometry at low speeds by Mellmann [15]	133
42	Relationship of wall friction coefficient with experimental mill speed	138
43	Illustration of the mill geometry at high speeds showing the Davis circle by Mellmann [15]	143
44	Comparing model and PEPT experimental mill speeds	146
45	The upper , mean and lower angles of repose during charge slumping by Mellmann [63]	148
46	Variation of angular velocity gradient across charge layers with mill speed by Govender [23]	149
47	Shoulder and toe estimates according to Powell & McBride and Cleary et al for the H7-W9-A90-S70 configuration. Small arrows: Cleary et al; Large arrows: Powell & McBride	152
48	Circulatino rate of tumbling mill charge from X-ray	153

	particle tracking experiment by Govender and Powell [6]	
49	Validating the circulation rate model.	157
50	Charge geometry showing the shoulder and toe angles. Redrawn after Morrell [54]	162
51	Basic geometry of charge used in the torque-arm implementation of power draw [144]	167
52	The torque-arm approach [23].	169
53	The torque-arm approach applied about the charge center of circulation	170
54	Energy transfer to milling environment	171
55	Power drawn by the charge in an experimental tumbling mill	173
56	Experimental power measurements using lab-view signal express	174
57	Applying the conservation laws at the microscopic level to tumbling mills	177
58	Applying the conservation laws at the macroscopic level to tumbling mills, redrawn after Morrell [54]	181

List of Tables

Number	Description	Page No.
1	Experimental matrix at UB	76
2	Experimental mill speed	77
3.	Experimental matrix at PEPT Cape Town	87
4	Fixed and non-fixed parameters	90
5	Circulation rates of all particle sizes at different load fractions and mill speeds	98
6	The CpM, CoC and repose angle values for all particle sizes	112
7	The circulation rate, mill speed and the departure shoulder angle	114
8	Motion forms and their subdivisions	118
9	List of Froude numbers at different mill speeds	123
10	Power draw for (0mm) lifters	172

Chapter One: Introduction

1.0 Introduction

Comminution is a mechanical process of reducing coarse materials to finer particles. Such a process is often used to produce materials with a specified size distribution from a coarser feed. On this basis comminution devices are classified based on the sizes to which they can reduce particles. The known common ranges are those that produce relatively coarse materials (crushers) to those that produce finer material (grinders such as AG/SAG mills). Common industrial applications can be found in pharmaceutical drug size reduction processes, chemical and ceramic industries, cement production, production of food and in the processing of waste. In the minerals industry these devices are widely used in extractive metallurgy operations, including the beneficiation of metalliferous and industrial minerals, iron ore, coal, precious metals and diamonds and in the preparation of quarry rocks. At present the wide range of comminution devices used in the minerals industry for the crushing and grinding of rocks and ores can reduce material from sizes of up to 100mm to much finer particles.

The first stage in mineral extraction is comminution, a process that accounts for large energy consumption in current mineral extraction and processing stages. In

its current context the physics of particle size reduction is not well understood. Careful measurement of energy input to a single particle during reduction has revealed that some comminution devices typically use only 1 - 5 per cent of the total energy supplied for particle breakage resulting in a very high operating cost [1]. Recent attempts at process optimization have focused on characterization of grinding mechanisms [2 – 5], quantifying power draw [6, 7] and understanding their consequences for downstream operations [8 – 12]. These optimization strategies require detailed investigation into grinding mechanisms encountered in industrial operations with a view to achieving improved energy efficiency.

The performances of comminution devices are affected by many variables such as production capacity, total energy consumed during milling as well as liner design and life. The greatest challenge facing mineral researchers today is achieving high specification product in the most efficient and consistent manner through the development of improved comminution circuits designs that will achieve energy efficiency and at the same time improve feed to downstream metallurgical processes. This may ultimately improve operating conditions and classification processes that may have a significant influence on milling efficiency and stability.

Much progress has been made over the years with new empirical models developed (Salazar et al) [3], high performance numerical simulation studies undertaken (Cleary and Morrison) [4] and scale-up studies (Cho and Austin) [5] carried out that have contributed significantly to understanding particle dynamics in these mills. The inferences from these studies are drawn from a wide range of theoretical, experimental and numerical approaches and are often based on the particular experiences of the process operator or researcher. Though none of these reports have provided a satisfactory description of charge kinematics in these mills, yet their work has contributed significantly to the elucidation of the complex relationship between energy input to the charge and the corresponding particle size reduction observed.

In this study numerical description of the motion of circulating charge at different mill operating conditions for tumbling mills is assessed. A model linking the circulation rate of charge particles with physical mill parameters (load fraction, shoulder angle and friction) was developed and tested using experimental data derived from Positron Emission Particle Tracking (PEPT). Theoretical descriptions of the energy acquired by the charge particles during milling are provided using a continuum approach. The models reported herein extend the ideas of Bird [13], Bird et al [14], Mellmann [15], Powell and Nurick [16], Rose & Sullivan [17] and Watanabe [18] among others.

1.1 Project Aim

The following aims provided the relevant motivation for undertaking this research:

1.1.1 To provide qualitative descriptions of media circulation trends observed in tumbling mills for different operating conditions,

1.1.2 To develop and test a mechanistic model of circulation rate using data obtained from PEPT trajectory fields,

1.1.3 To investigate the influence of the circulation rate model on power draw for conventional tumbling mills.

1.2 Key Questions

1.2.1 What measurable mill operating variables influence circulation rate?

There is a notable lack of information on the actual trajectories followed by particles in tumbling mills. In these mills the speed of circulation of the charge particles relative to mill rotation, otherwise known as the circulation rate, is assumed to be unity by many mill models. This assumption allows for simple mathematical manipulation of the models leading to power quantification and prediction of breakage kinetics in these mills. However, the wide disparity in the reports suggests experimental techniques employed in these investigations could not provide adequate information of particle trajectory in these mills. The mill rotational speed and the mill internal design induce rotational motion in the charge and the particles are reported to follow a distinct trajectory whose total length may be shorter than the mill circumference [6, 16]. These reports suggest circulation rate can be a function of measurable mill parameters such as mill speed, load fraction and angle of repose, etc. More remains to be done in establishing the key mill operating parameters that influence charge circulation rate. A major output from the research was to model the circulation rate of the charge based on charge kinematics in the various regions of the mill, relating it to measurable operating parameters such as load fraction and mill speed.

1.2.2 How does circulation rate influence power draw in tumbling mills?

Traditional power models for characterising energy utilisation in tumbling mills rely on the coordinates of the charge centre of mass and the mill speed [6, 20 - 22]. This approach has facilitated the understanding of energy transferred to the grinding media, however, the discrepancy between experiment and theory remains large, particularly at low speeds. We note that the difference reduces with increasing mill speed indicating that the actual energy acquired by the charge is

not fully captured in the traditional approach. This research includes an analysis of energy distribution in the grinding charge and the comparison with experimental results to provide numerical descriptions of power draw in these mills as influenced by circulation rate.

1.3 Hypothesis

The following hypotheses were tested in the study:

1.3.1 The *circulation rate* of the charge in a tumbling mill *decreases* with *increasing mill speed* due to an *increase* in the *centrifugal forces*.

The trajectory of a circulating particle is affected by the rotational kinetic energy imparted to it by the mill rotation. A complete circulation of a particle around the centre of circulation (CoC) can be significantly shorter than the mill circumference causing the particles to circulate faster than the mill rotation even at low mill speeds. At higher mill speeds the ratio of the speed of circulation of the charge to that of the mill rotation (known as the circulation rate) tends towards unity in part due to the longer trajectory paths covered by the circulating particles. This observation is supported by an increase in the centrifugal force effect felt on the individual particles with increasing mill speed. This hypothesis will test the relationship between circulation rate of the mill charge with that of mill speeds used in all experiments.

1.3.2 The *circulation rate* of the charge in a tumbling mill has a *non-linear* relationship with mill *load fraction* due to the variations in the *limiting static friction*.

Friction in grinding media mills arises from particle-mill wall interaction which may be static or kinetic friction [23]. Govender [23] derived an expression for grinding media-wall friction coefficient and concluded that the constant fluctuation in this friction effect is caused by the changing number of overlying layers in the *en masse* region as the charge cataracts. Provided the charge does not slip, reduction in the number of overlying layers will lead to a corresponding increase in the limiting static friction and vice-versa. Hence the higher the load fraction the higher the limiting static friction [23. 24] and the lower the circulation rate since particle kinetic energy is dissipated in overcoming the increased load and friction. As mill load is increased further, however, the total inertial effect of the mill charge contributes to lowering the circulation rates at the same mill rotational speed. This hypothesis will test the relationship between circulation rate of the mill charge with that of mill load fractions used in all experiments.

1.3.3 The *total energy acquired* by the circulating charge in tumbling mills will be *less than* the *energy transferred* to the charge due to *work done* in overcoming *friction*.

This hypothesis simply implies that the total energy transferred to the circulating charge goes partly as energy acquired by the charge and partly as energy lost during grinding. The different modes of this energy loss are (i) particle to mill wall friction and (ii) friction between particle layers (shear stress dissipation). This hypothesis will test the relationship between energy transferred to the circulating charge and that of the actual energy acquired by the charge.

1.4 Objectives

The following objectives were formulated to test the hypothesis:

1.4.1 Investigate transverse charge motion in tumbling mills and characterize its transitions

In order to visualize the dynamics of charge motion in the opaque environment of industrial tumbling mills required a study of known descriptions of motion in a plane described by charge circulation. The transition of this motion from one form to another has been widely investigated [15 - 18]. This objective provides detailed descriptions of the known categories of these motion forms and their sub-types. The study also discusses the conditions, during milling, that lead to a transition between these categories of motion. An attempt is made at consolidating existing mathematical models in order to include the details of granular systems in the description (geometry, shape, angles, etc.) that allows for a meaningful classification into distinct flow regimes (rolling, cascading and cataracting).

1.4.2 *Develop numerical methodology for calculating circulation rate from PEPT trajectory fields*

This objective is focused on developing a computational methodology for the experimental determination of circulation rate using data derived from particle tracking experiments. Powell and McBride [24] defined circulation rate as the average number of circulations made by the charge per revolution of the mill, equation (1). A key outcome of this objective was the characterization of charge circulation rate with a view to developing experimental procedures for their measurement and computational methodologies for their evaluation. These two approaches were then compared for correlation.

$$\text{Circulation rate } C = \frac{\text{Speed of circulation of the charge}}{\text{Speed of rotation of the mill}} \quad (1)$$

1.4.3 Develop a model of circulation rate based on mathematical transverse forms of charge motion

The motion of the charge in the rotational plane is analysed in order to formulate a mathematical model of circulation rate whose parameters are directly measured from PEPT experiments. These parameters integrate a wide range of physical and geometric milling conditions such as load fraction, mill speed, internal wall friction coefficient, mean and critical angles of repose, departure shoulder angle and the impact toe angle.

1.4.4 Investigate current power draw models with a view to assessing the influence of circulating trends on power draw

The charge in a tumbling mill does not dictate its own direction of flow. The direction of flow is imparted to it by the effect of the mill rotation and the shape of the free (cascading) surface. The motion of the mill is transferred to the content of the device, termed charge, and the resultant mechanical action applied to the ore particles leads to their damage and potential breakage [16]. However, at very high speeds the particles are seen to form upward tails that significantly reduces the total number of impact events [17, 20 - 23]. Such a situation is industrially undesirable and several studies have been devoted to investigating the mechanism of power transfer to the grinding environment and its utilization during milling. Of particular interest is the rotational speed that maximizes impact events in mills that typically run below critical speed such as tumbling mills and most industrial flow systems. The distributions of residence time, transverse velocity, charge

acceleration and power draw in the grinding charge is analysed and the trends used to describe energy acquired by the charge during milling.

1.5 Methodology

The research methodology employed both a numerical and an experimental approach.

A numerical approach was used to:

- develop a charge motion model that linked the circulation rate of the charge to physical and geometric parameters of the mill operation,

- develop a continuum-based granular flow model for characterizing the bulk (dissipated) energy distribution in typical tumbling mill configurations.

By taking a continuum approach to power modelling allows for a meaningful delineation of the power distribution into aspects of breakage, flow, heat, etc. The model reported in this thesis is a mechanistic model of power draw that predicts the distribution of energy in the grinding environment of tumbling mills based on a continuum approach.

Experimentally, detailed PEPT experiments were conducted at two laboratories and the data so obtained used in this research. The first set of data is derived from the experimental program conducted by the Centre for Minerals Research (University of Cape Town) at the Positron Imaging Centre, University of Birmingham (UB) in 2009. Recent experiments (2011) were conducted at the iThemba LABS near Cape Town to extend the range of mill speeds used in the first set of experiments. For the various models reported herein, parameters are

obtained directly from the *in-situ* flow field of the PEPT tracer particles. The use of in-situ flow field measurements (via PEPT) allows for unique insights into the flow field and constitutes the key ingredients for developing and validating the models reported in this thesis.

1.6 Justification

At presently many comminution models describing material transport and particle breakage in tumbling mills are empirical. Although these models are highly tweaked for the current operating parameters, they are limited *apriori* by the machine boundary conditions. Consequently, the ability to extrapolate does not exist. This limitation does not meet the current needs in mineral processing – current operations are not comfortably viable given the constraints imposed by depleting ore bodies and ever tightening regulation. To improve profitability, it is essential that models are able to predict new (and viable) operating boundary conditions. To best achieve this, it is essential that the models of material transport and particle breakage provide more accurate quantitative predictions about wear rates and distributions, collision forces, dynamic loads on boundaries, power consumption, torque and flow rates, sampling statistics, mixing and segregation rates and many other quantities encountered in mineral processing operations. Recent non-empirical reports include the works of Herbst [145], Powell [118] and Tavares [146] who have developed mathematical models of tumbling mills using approaches such as DEM. With PEPT providing an in-situ perspective of the kinematics of the charge in the mill these predictions can now be made with some degree of accuracy.

1.7 Conclusion

The motivation for the development of the models reported herein were based on Mellmann's [15] classifications of media rotating motion modes from slipping to cascading to cataracting. The descriptions provided in this thesis improve on models presented by Mellmann [15], Rose & Sullivan [17], Watanabe [18] and others who provided purely geometrical descriptions of the transverse charge motions in rotating kilns. These models are extended to include physical parameters such as mill speed, mill load, mill tangential velocity, mill internal wall friction coefficient, polar coordinates of the centre of mass (CoM), the departure shoulder angle, critical angle of repose of the entire charge and the mean charge deflection. Of value is that mill speed (which is always known) is now related to geometric parameters of the charge that are not easily measured. These models are used in the formulation of a charge circulation rate model that compares well with experimental values for the range of mill speeds used.

Chapter two: Literature Review

2.0 Introduction

In comminution modelling three fundamental processes are often investigated: breakage, mixing and segregation [11]. In the minerals industry particle breakage can be avoided, limited or encouraged depending on whether it is desirable or not, making it an important phenomenon in a wide range of industrial applications. Mixing and segregation studies are closely inter-related. Due to the varying size and specific gravity of particles mixing occurs almost simultaneously with segregation because gravitational forces acting on mixing particles tend to segregate them into size and density ranges. Research into these three processes is greatly influenced by advances in measurement technology.

This literature review takes a look at charge motion in rotary grinding mills with particular focus on the rotational motion mode. We provide a review of general literature on charge motion in industrial tumbling mills and their implication for characterizing charge circulation rate in these mills. The term circulation rate is at best conceptual and to date no detailed description has emerged to inform grinding kinetics and charge kinematics in mills typically encountered in industrial operations. The most relevant descriptions so far have been provided by Powell and Nurick [16], Govender [23] and Powell and McBride [24].

The modelling of tumbling mills has followed both an empirical and numerical approach with a view to mill performance optimization. Empirical models are computer-based modelling methods using different software tools developed on the concept of Observation, Dependency and Agency (ODA). In the numerical sense a time-stepping graphical procedure is used to predict the model's behaviour over time leading to a mathematical solution. This review discusses a number of investigations on grinding processes in tumbling mills reported and how they predict particle breakage in these mills. The important phenomenon of angle of repose which determines particle segregation and mixing kinetics is discussed. The discussions also includes a number of key paper reviews ranging from studies on the critical speed required to centrifuge the charge to the novel positron emission particle tracking technique which provides an *in-situ* perspective of the charge in the opaque environment of industrial mills and is a divergence from the end-window filming technique.

2.1 Grinding Mill Charge in Tumbling Mills

Granular materials form the bulk of the charge found in most industrial tumbling mills. They range from coarse materials to microscopic grains with varying sizes, densities, surface toughness and hardness and when mixed with water form slurry or paste [1]. These granular materials are characterized by a loss of energy during particle interaction, a phenomenon similar to that described by Coulomb's law of friction. Powders are of particular importance due to their fineness and cohesiveness allowing the formation of suspensions. Fine powders have unique properties and can exhibit solid, liquid or gas-like characteristics depending on the average energy per grain.

Most tumbling mills are fed from either primary/secondary jaw crusher products or from the run-of-mine as in South Africa. [1]. Feed ore characteristics vary from

mill to mill. For ball mills the filling may remain approximately steady over time. However feed ore contributes significant quantities of rocks to the charge in Autogeneous/Semi-autogeneous Grinding (AG/SAG) mills with variations in hardness and size distributions having significant consequences for other mill parameters such as mill speed, torque, the angle of repose, toe and shoulder variations and the milling power draw [1].

Tumbling mill feeds are either fluidized such as sand or compact such as rocks, depending on their densities, with each having its own physics which controls the mechanical behaviour of the mill. Mechanical properties which characterize the mill charge include [1]:

- Particles:
  - Size,
  - Shape and
  - Mass.

- Mill:
  - Velocity,
  - Acceleration,
  - Filling liner design and
  - Filling degree.

- Energy transfer:
  - Cumulative abrasion and impact energy transfer,
  - Normal impact forces and
  - Tangential impact forces.

The trajectory of particles in a tumbling mill follows a distinct path. Due to the action of lifters and the mill rotational motion charge at entry are lifted upward towards the departure shoulder. Between entry and discharge there is a whole

range of rotational and translational charge motion modes that are affected mostly by friction and the aggressive mill rotational motion. This research discusses the rotational modes of charge motion or circulation rates of the mill charge.

2.2 Tumbling Mills

In general a tumbling mill is a cylindrical or cylindro-conical drum that rotates about a horizontal axis causing its contents – charge – to undergo a distinct circulatory (or tumbling) trajectory. Its operating conditions are affected by such parameters as rotational speed, liner type as well as size and shape of the tumbling charge. Common types are ball mills, rod mills, pebble mills, tube mills and autogenous/semi-autogenous grinding (AG/SAG) mills.

2.2.1 Ball Mills

Ball/pebble mills are used as single stage grinding or as second stage in a two stage grinding circuit to achieve product sizes of 35 mesh or finer [1]. While ball mills may use steel and other metallic media pebble mills often use ceramic or rock media. Both mills can be operated in open or closed circuits depending on whether regrinding is necessary or not. These mills have been optimized primarily through experimental procedures and their performance is evaluated by the amount of electricity consumed per ton of product [37 - 39]. In a recent publication Wang et al [40] developed an algorithm for minimizing power utilization in ball mills and concluded that a non-linear relationship exist between electric consumption and process parameters leading to a non-linear power draw model.

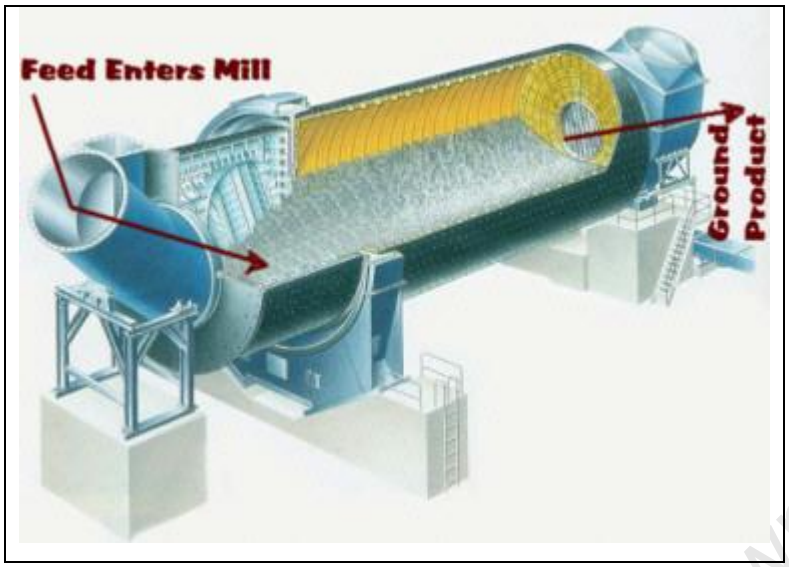

Fig 1: Ball mill with cut away section showing feed and discharge ends.. Picture taken from Mine-Engineer website: http://www.mine-engineer.com/mining/ballmill.htm.

2.2.2 Rod Mills

When rods replace grinding balls or rocks the mill is referred to as a rod mill. Rod mills use long rods as grinding media (35 – 65% of charge) with the length to diameter ratios adequately selected to prevent rod charge tangling. They are designed in such a way that the rods tumble and spin in roughly parallel alignments that simulate a series of roll crushers. Rod mills can be of the overflow, end peripheral discharge or central peripheral discharge type depending on the discharge mechanism. In the minerals industry only the overflow mills are in common use mostly for wet grinding of ores. The mills must operate at lower speeds than that encountered in ball mills allowing for better contacts between the rods and mill charge. The main challenge to operating rod mills is the risk of wear to rods and mill liners. This, coupled with the problem of misalignment and rod tangling, means rod mills require greater operator attention that most other grinding mills. Hence much of the research into these mills has been focused on its design parameters, circuit efficiency and mill performance.

Laplante et al [41], conducted detailed error analysis for the use of bond work index in rod mills and concluded that the fineness of the feed ore can have significant effect on mill performance and hence circuit efficiency. Hosten and Ozbay [42] used a rod mill to ground five size fractions of chromite ore and found no relationship exist between particle shape and size as compared to piston die press method.

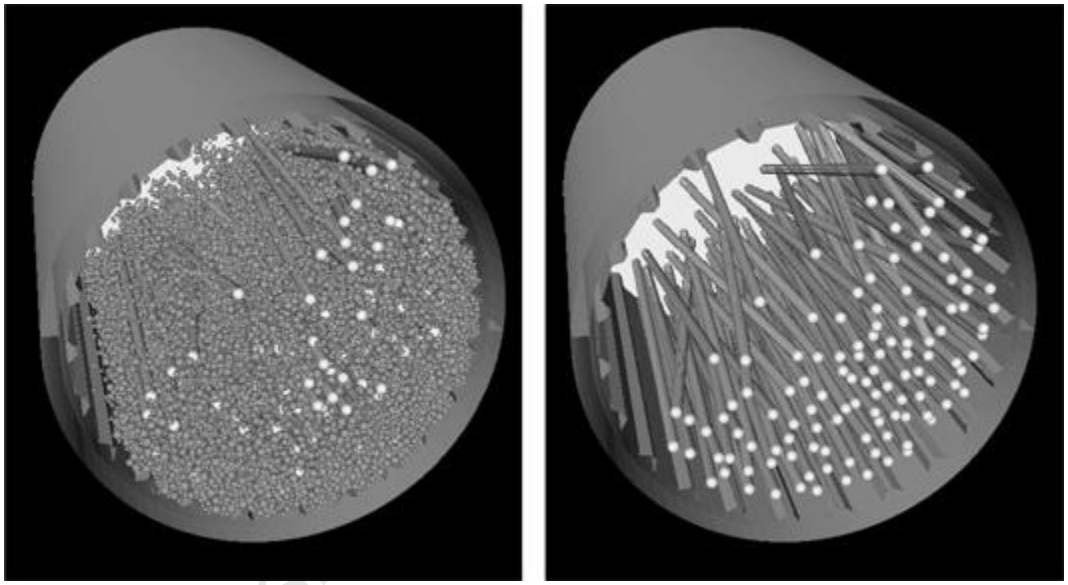

Fig 2: Rod mill with rotating drum causing friction and attrition between rods and ore particles. Picture taken from Emerald website: http://www.emeraldinsight.com/journals.htm?articleid=1455507&show=html.

2.2.3 AG/SAG Mills

Autogenous and semi-autogenous grinding (AG/SAG) mills are known to have a major advantage in terms of capital cost and the ability to treat a wide range of ore types [43]. Due to the equipment size of conventional circuits which presents some complexity in terms of their operation and control, AG/SAG mills are now the most widely used alternatives in the field of mineral size reduction [1, 3]. Their numerical advantage is underscored by their comparatively higher

processing capacity, lower physical space requirement and lower investment and maintenance cost [3]. Concha et al [44] suggested these numerical advantages are critical in guaranteeing mineral processing plant profitability.

Among the numerous studies carried out on these mills is the work of Valery Jr. and Morrell [45] who developed a dynamic model for AG/SAG grinding. They found the size distribution from a breakage event to be dependent upon both the ore type and the specific energy associated with the breakage event, while the breakage rate function is governed by the mill load particle size distribution and mill speed. On the basis of this function a breakage parameter (t_{10}) can be defined as the fraction of broken product which is smaller than one tenth of the original particle size and according to Whiten [46] this parameter can be related to the entire product size distribution. The model of Valery Jr. and Morrell [45] can be used to predict charge mass, charge size distributions and the product size distributions. Knowing the charge mass, mill dimensions and mill speed the power draw can be estimated.

Other studies on AG/SAG mills include the measurement of mill parameters [47 - 49], control of SAG mills [50], development of dynamic models [51, 52] and the prediction of mill power draw [53, 54] among others. In these studies prediction of comminution behaviour within the particle bed is characterized by the breakage probability and breakage function. The breakage probability is defined as the mass fraction of the progeny smaller than the lower bound of the initial size fraction and the breakage function describes the particle size distribution of the broken progeny. [33].

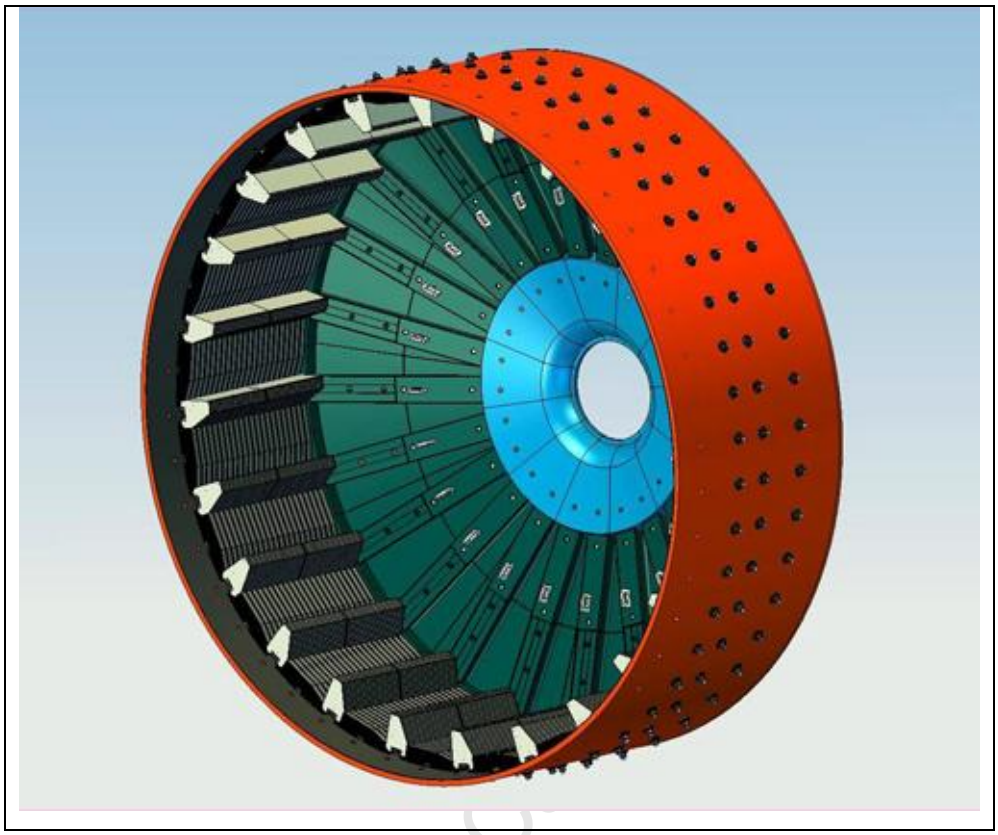

Fig 3: SAG mill. Picture taken from Wear Minerals website: http://www.weirminerals.com/products__services/mill_lining_systems/mill_liners/ag__sag_mill_liners.aspx.

2.3 Comminution of Tumbling Mills

Much of the work on comminution in tumbling mills has been focused on optimization studies and the development of representative models through simulation. Optimization is a mathematical process of maximization or minimization of a given function subject to constraints. The method is a "linear programming technique" that can be discrete or continuous or a combination of both. The most important simulation technique widely employed is the discrete element method (DEM). The technique has been widely used in the development of power models but is yet to be successfully used in simulating breakage kinetics in industrial mills.

2.3.1 Optimization of Tumbling Mills

A comminution device is equipment that converts input of energy into mechanical motion. This motion is transferred to the content of the device - charge - and the resultant mechanical action applied to the ore particles leads to their damage and potential breakage [16]. The primary purpose of comminution is rock breakage and rocks can be reduced from the coarse to known particle sizes.

Several publications have detailed the development of tests that address the relationship between the applied energy and the resultant size reduction achievable [1, 16, 25 - 27]. These studies have shown that the power consumed during comminution can be directly related to the amount of energy required for particle size reduction and through that to the cost of operation. Rittinger [25] proposed a theory which states that the energy required for size reduction is proportional to the newly created surface area. The formulation of this widely acknowledged energy distribution theory was reinvestigated by Bond [27], on the basis of which Schonert [28] showed that the energy efficiency of grinding processes lies in the range of 4 – 8%. Kick [26] used a specific energy approach in defining the energy-particle size relationship and suggested that the energy required to break a particle of a certain material is proportional to its mass or in other words the specific energy (energy per unit mass) required for breakage is constant. This approach is often referred to as the breakage theory of comminution and recent work by Tavares and King [2] as well as Stamboliadis [29] has shown that this theory is true only for relatively large particles.

Rock production, as the first stage of comminution, is often accomplished by blasting and crushing [2] and the product is one of the main materials used in the construction of infrastructures such as roads, railroads and buildings [30]. In the mining as well as rock mechanics sectors rock test are very often undertaken on specimens of known geometry under strictly defined loading conditions [11]. The

breakage of ore particles during milling on the other hand is determined by the mechanical environment applied to them [16]. For example Liu et al [21] investigated the inter-particle breakage process under confined compression in mechanical crushing in order to optimize the design of fragmentation devices and found two breakage modes can be identified – single particle and inter-particle breakage. Single particle breakage occurred when the distance between the chamber walls were smaller than the particle size. Inter-particle breakage occurred when the particle had contact points shared with other surrounding particles and this is believed to be an important breakage mode in mechanical crushing.

The product size distribution achievable in comminution devices are of paramount importance since either very fine or coarse products will have considerable implications for downstream processes leading to increased cost, waste and lowered efficiency of the mineral recovery process [1, 11, 16]. The comminution in the various particle size ranges characterizes the grinding behaviour of the materials used [27] and determines the evolution of their size reduction process [31, 32]. To date different grindability tests have been carried out with limitations in the accuracy of predictions.

Bearman et al [33] examined the relationship between rock strength parameters, power consumption and the resultant product size in crushing and found the tensile based parameters showed a highly significant correlation with crusher performance. Yekeler et al [22] investigated coal grinding using the Hardgrove index (HGI) and suggested that an equilibrium condition can be achieved when the size distributions of the particles within the charge of the mill no longer change with continued grinding. Working with ball mills, Tansathikulchai et al [34] showed that the best grinding conditions in these mills are produced by a slurry density making wet grinding more efficient than dry grinding. Braun et al [35] conducted a series of test on the hicom mill using dry calcium carbonate and concluded that fine and altra-fine grinding can be achieved with good energy

efficiency in these mills. Austin et al [36] showed that ball milling of iron ore involves grounding, pelletizing and sintering process that gives the material considerable porosity which can vary as the material becomes finer depending on the size distribution of the pores.

One important conclusion that can be drawn from these researches is that for a given feed material and energy input the best comminution device is one which could provide the correct fracture energy to each target product particle size distributions (PSDs), bearing in mind the advantage of power efficiency.

2.3.2 Modelling of Tumbling Mills

Qualitative flow phenomena are not only describable from experiments but can also be reproduced through numerical simulations of assemblies of frictional, inelastic spheres and non-spherical particles. The rapid development of computing power, interactive computer graphics and topological data structure has ensured that the use of computer simulation techniques has become the most powerful tool for obtaining useful inter-particle breakage clarifications [21]. A range of techniques have been developed over the years for modelling the behaviour of large numbers of particles in different situations. These range from treating the material being studied as a continuum, with the physics averaged out over all the particles [46], through to treating each particle as a discrete element (Discrete Element Modelling – DEM) [12]. An essential aspect of DEM simulations is that collision interaction of particles with each other and their environment are detected and modelled using contact force laws. Equations of motion are then solved for the particle motions and for the motion of any boundary objects with which the particles interact [12, 56]. There are three key aspects of DEM simulations;

- Use of a search grid to construct a particle near-neighbour interaction list

- The collision forces for each interaction are estimated for each pair of particles in the near-neighbour list.
- Summations of all the collision and other forces acting on the particles with integration of the resulting equations of motion.

DEM is computationally intensive but is becoming more popular as computer processing power has increased. In DEM of granular flows, the trajectories, orientations and spins of all the particles and objects in the system are calculated and their interactions with other particles and with their environment are predicted. It is necessary to simulate particles of many different sizes and densities interacting with complex shaped objects moving in different ways [12, 55].

Conducting DEM simulation of mills can provide useful data needed to study the dynamic nature of the media leading to prediction of their breakage kinetics. However, to date DEM simulations use simplified particle geometries that make it difficult to successfully simulate ore breakage [55].

Examples of DEM studies on tumbling mills include a 142mm laboratory-scale tumbling mill [23, 56] as well as the work of Herbst [145], Powell [118] and Tavares [146]. In these studies, a number of characteristics including charge behaviour, torque and power draw for a range of rotation rates (between 50 - 130 per cent of the critical speed for mills) have been analysed. Other aspects of such studies include an examination of the sensitivity of the results to material properties and size distributions [56] and a comparison of simulated flow rates with those observed using high speed X-ray photography [23]. A more recent technique for particle tracking, known as Positron Emission Particle Tracking (PEPT), is now available.

2.4 Positron Emission Particle Tracking (PEPT)

For more than a century now comminution modelling has been heavily reliant on the end-window filming technique. An important component in the optimization of comminution processes is the development of representative models whose primary purpose is to guide the highly non-linear behaviour to the desired objectives of mineral processing plants. However, the aggressive nature of the milling environment does not afford direct access to the mechanical environment. This is the environment in which the end window technique gained impetus. The end-window filming technique is a method that involves estimating mill product size distribution as a function of mill feed size and hardness and mill operating conditions [44, 45, 47 - 49]. It allows for robust descriptions of highly tweaked models that are used for trouble-shooting most problem scenarios in industries. In consequence the available literature lacks the creativity in helping elucidate the fundamentals governing charge motion in rotary grinding mills.

In recent years novel technologies have emerged that provide an *in-situ* perspective of particle dynamics deep within the charge body. Positron Emission Particle Tracking (PEPT) and X-ray imaging techniques are specialized systems that aid in the 3D time-dependent particle tracking with PEPT particularly allowing for the use of real charge within a scaled laboratory mill.

Positron Emission Particle Tracking (PEPT) is a unique technique which was first implemented at the University of Birmingham (UK). The purpose is to track the trajectory of a radioactive particle in complex flow systems. A radioactive tracer – which can be made of resin, alumina or glass beads - is produced using an in-house cyclotron for use in experiments. Common radioisotopes used may include F-18, Cu-64, and Ga-68 [57].

The tracer is then placed in the system of study within the field of view of a positron camera, see figure (4), which shows the configuration in the Birmingham camera system. The decaying nucleus releases a positron which combines with a free electron in an annihilation process that results in the emission of two anti-parallel 511keV photons. The gamma rays are detected in a pair of positron detectors (in the PEPT camera system at UB) and the very high number of photons emitted allows the tracer position to be found by triangulation. The process can be repeated a few thousand times per second making it possible to track the tracer. Knowing the tracer position over time allows the visualization of charge motion and hence other information such as the velocity, the occupancy, the dispersion, etc, can be calculated [57].

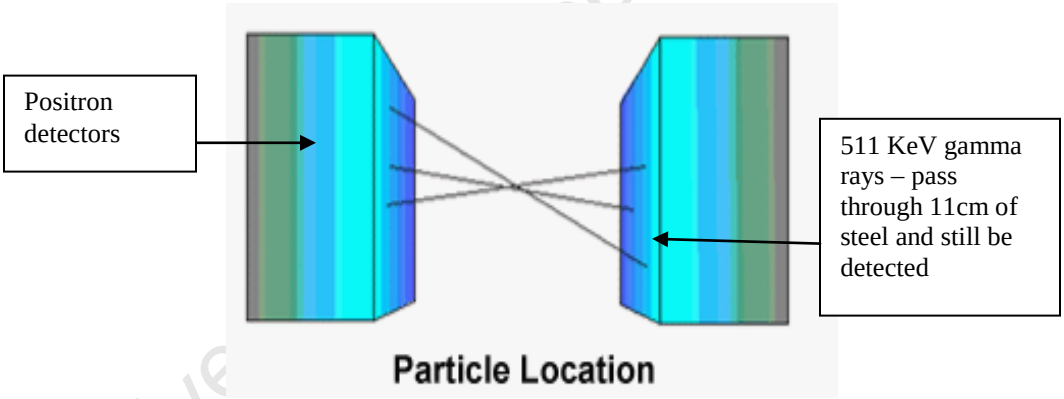

Fig 4: Particle tracking system in PEPT - (UB)

Thus PEPT is capable of providing detailed kinematic histories of real rock and slurry, the charge found in most industrial application. This paradigm shift has been particularly important in the validation of discrete element method (DEM) due to its capability to compare trajectory fields of real rock and slurry particles with that of spheres and superquadrics currently achieved by DEM [58]. Through PEPT experiments and DEM simulations one can obtain a better insight into charge kinematics in rotary grinding mills – with particular emphasis on understanding charge motion in a plane that defines its circulation.

2.5 Tumbling Mill Charge Motion

The particles in a tumbling mill can undergo various kinds of motion including spin, rotational and translational. Translational motion is often referred to as material transport and defines motion along the axis of the mill between entry and discharge. Due to the mill rotational motion however most charge motion is in the transverse (charge circulating) plane and this plane is important in the description of grinding kinetics. This section looks at studies on tumbling charge motion and addresses the important phenomenon of angle of repose.

2.5.1 Circulation Rate

Studies on charge motion in rotary grinding mills have spanned a wide range of ideas with efforts made on setting out simple grinding theories [25 – 27, 35, 61, 62], studies on liner designs undertaken [63 - 65], quantitative descriptions of energy transferred to the charge attempted [20, 29, 51, 59, 66, 67] and work on the development of empirical and numerical models reported [9, 20, 21, 22, 30, 33 – 36, 43 – 45, 60, 68, 69]. These reported studies present excellent results obtained from an end-window filming technique that, however, does not provide clear descriptions of the interaction of particles in the grinding environment of these mills. There is a notable lack of information on the trajectories followed by particles in these mills. Bachmann [70] considered the charge in a vibrating mill as a fully plastic body resting on a horizontal plane which oscillates circularly, while the bulk motion model presented by Mishra et al [69] remains to be verified against experimental observation. The speed of circulation of the charge particles otherwise known as the circulation rate has never been directly investigated but is merely assumed to be unity by many mill models. This apparently allows for

simple mathematical manipulation of the models leading to quantification of power draw and prediction of breakage behaviour in these mills.

The motion of a tumbling mill is translated into mechanical energy acquired by the charge in the form of rotational motion [16]. This charge motion arises from the mill internal design and mill speed and this determines the power draft, stressing intensity and stressing probability, mixing kinetics inside the mill, material transport and the performance of a mill [7]. The subsequent work done on the charge can increase its potential energy, linear kinetic energy, rotational kinetic energy and temperature. According to Powell and Nurick [16] an important parameter in the description of charge motion, and hence an understanding of circulation rate of the particles, is the Center of Circulation (CoC).

The CoC is a unique point about which the entire charge appears to circulate and when accurately located gives a measure of the geometric location of the entire charge [24]. The path of the balls in the *en-masse* region form concentric rings of decreasing radii that converge at the CoC [16]. One circulation of the charge is then a complete revolution of the charge about the CoC and when divided by the time of revolution gives a measure of the circulation rate [16, 23, 24]. This definition of circulation rate is further extended through normalization by dividing the circulation rate of the charge by the mill revolution [23]. This definition is an improvement on the traditionally known definition which simply states that the circulation rate is the number of revolutions of the charge per second. The limitation of the traditional definition can be seen through an analysis of the radial position of the CoC at various speeds as investigated by Powell and Nurick [16]. The CoC will have a minimum radial position when a single layer of the balls begin to cascade down the surface of the charge. At higher speeds when cascading disappears and the descending charge is all cataracting the CoC moves into a central hollow space of the charge and at the point of centrifuging the CoC coincides with the center of the mill.

2.5.2 The Angle of Repose

The angle of repose has been defined simply as the maximum angle of a stable slope determined by friction, cohesion and shape of the particles [16]. It has been found by Botz et al [71] to be a function of:

- medium material properties,
- charge shape and dimensions,
- maturity state,
- surface friction properties and
- deformation ability.

The engineering significance of the repose angle can be explained by the "Talus slope", which is the steepest slope a pile of granular material will take. The limiting angle achieved determines whether or not a slope will collapse. This phenomenon is often used in classical contact mechanics theory to study adhesion in "sandpiles" and other spherical particle packing behaviour. Zhao et al [72] conducted detailed analysis of the grinding properties of ginger powders and concluded that increasing the angle of repose results in reduced powder flowability of ginger, while the formation of aggregates means the angle of repose decreases with decreasing particle size. Their work was closely correlated by Santomaso et al [73] who investigated powder flowability and density ratios, as well as by Ileleji and Zhou [74] who studied the angle of repose of bulk corn stover particles. These reports show that the angle of repose can be used to provide a realistic reflection of the dynamic conditions in mills as compared to predictions.

A variance to the repose angle which is of significance in the study of grinding media mills is the "dynamic angle of repose." Segregation and hence liberation of particles in these mills can be explained by the difference in the dynamic angle of

repose of the various size fractions. According to Herrmann [75] the size fraction with the lowest dynamic angle of repose will be the natural first fraction to be liberated from the *en-masse* and this process continues till the *en-masse* is completely depleted of that size fraction. De Gennes [76] suggested that small perturbations caused by a difference in the dynamic angle of repose of the different size fractions will tend to send some particles out of the *en-masse* and into the adjacent liberated or segregated phase. Among the most recent work on the angle of repose is the work of Govender [23], Powell and McBride [24] and Powell and Nurick [16].

Govender [23] employed the dynamic angle of repose in describing a charge surging mechanism observed in most industrial mills. He suggested the dynamic angle of repose provides the natural slope path along which the charge body in a tumbling mill undergoes oscillation and this is important when describing the torque exerted by the charge and consequently the power draw. The key indicator is the constant fluctuation of the power draw. He used a block and inclined plane to explain the mechanism of surging, deriving an expression for the case of zero acceleration and showing that this occurs when the charge goes through the mean angle of repose.

Powell and McBride [24] investigated the relationship between the centre of circulation (CoC) and the repose angle (two important geometric locations0 and suggested that "the tangent to the equilibrium surface at the (CoC) is perpendicular to the radial line passing through the (CoC). This condition is uniquely defined because the equilibrium surface has a different curvature to that of the mill shell, so only one point on the surface can have a tangent perpendicular to a radial line." According to Govender [23], one important implication of the Powell and McBride definition is that the angle of repose of the charge in a mill is simply the angular position of the (CoC) taken from the downward vertical.

Powell and Nurick [16] then used this angular location of the (CoC) in describing the influence of the angle of repose on the motion of grinding charge in AG/SAG mills. According to these authors, at very low speeds the charge will be lifted up the side of the mill – by the action of the lifters and with sufficient friction - until it reaches the angle of static equilibrium of the charge. This allows a single layer of the balls to cascade down the surface of the charge, giving the least initial radial location of the (CoC) and hence the lowest angle of repose of the charge – known as the "static angle of repose." The angle of repose increases with mill speed from this static value, determined by the composition of the charge body, towards the horizontal as the charge centrifuges. Hence at the point when the entire charge centrifuges the (CoC) must coincides with the mill center and the angle of repose (angular location of the CoC) tends towards 90^0 which is the upper limit.

2.6 Review of Selected Papers on Charge Motion, Grinding Regions and PEPT

In this section we review a number of selected papers first on charge motion, then grinding regions and finally on the Positron Emission Particle Tracking (PEPT) experimental technique. The mill speed required to centrifuge the charge is described by Watanabe [18], while the recent work of Mellmann [15] has contributed to understanding charge motion transition zones. His work describes charge motion changing from one form to another. The review also includes novel work carried out by Powell and McBride [24] on the formation and intensity of grinding regions in AG/SAG mills which can be used to improve milling efficiency. A report by Govender et al [60] on PEPT of charge particles in a scaled industrial tumbling mill is also discussed.

2.6.1 Critical Rotation Speed for Ball-Milling - Watanabe [18]

A. Introduction

The critical rotation speed for dry ball-milling was studied by Watanabe [18] both experimentally and through numerical simulation using the Discrete Element Method (DEM). The behaviour of balls in a ball mill is very complicated. Previous researchers had found that with increasing mill speed, distinct avalanche, continuous avalanche, cascading motion, cataracting motion and centrifuging motion appear sequentially. Ross and Sullivan [17] then investigated the critical rotation speed required to arrive at centrifuging motion. However after the work of Rose and Sullivan [17] the critical rotation speed was not investigated further.

B. Experimental Work

In a previous work by the same author the critical rotation speed was re-examined experimentally in which he showed that it varies non-linearly with ball-containing fraction. To determine this dependence Watanabe [18] measured the critical rotation speeds at various ball-containing fractions ranging from 0.3 to 0.95 (%) stepped by 0.05(%). Using an asymptotic solution he showed that as the ball-containing fraction approaches unity the critical rotation speed approaches a value given by Ross and Sullivan's equation [17], see equation (2).

$$N_c = \frac{1}{2\pi}\sqrt{\frac{2g}{D-2r}} \tag{2}$$

In equation (2), (D) is the inner diameter of the mill and (r) is the radius of the balls. The parameter (N_c) then represents the critical mill rotation speed.

C. Discrete Element Method of Ball Mill

In the study under review Watanabe [18] used the Discrete Element Method (DEM) to analyse the behaviour of ball-milling more microscopically. The result from this numerical simulation is shown in figure (5). Open circles represent experimental values while open triangles represent results from DEM simulation. With the concentration and diffusion coefficients both been equal to zero he assumed that the axial motion makes no significant contribution to centrifugal motion which allowed the numerical simulation to be implemented in two dimensions – that is, the dimensions that define the circulating plane of the balls. This assumption thus allowed Watanabe [18] to analytically derive the determinant equation for defining centrifugal motion as given by equation (3).

$$N_c = \frac{1}{2\pi}\sqrt{\frac{g}{R\sin\theta_c\sqrt{1-\alpha}}} \tag{3}$$

In equation (3), (θ_c) is the critical angle of repose of the material and (α) is the volume-containing fraction. From equation (3) Watanabe [18] concluded that when the outermost layer of the balls form concentric rings with the mill shell the critical rotation speed is reached.

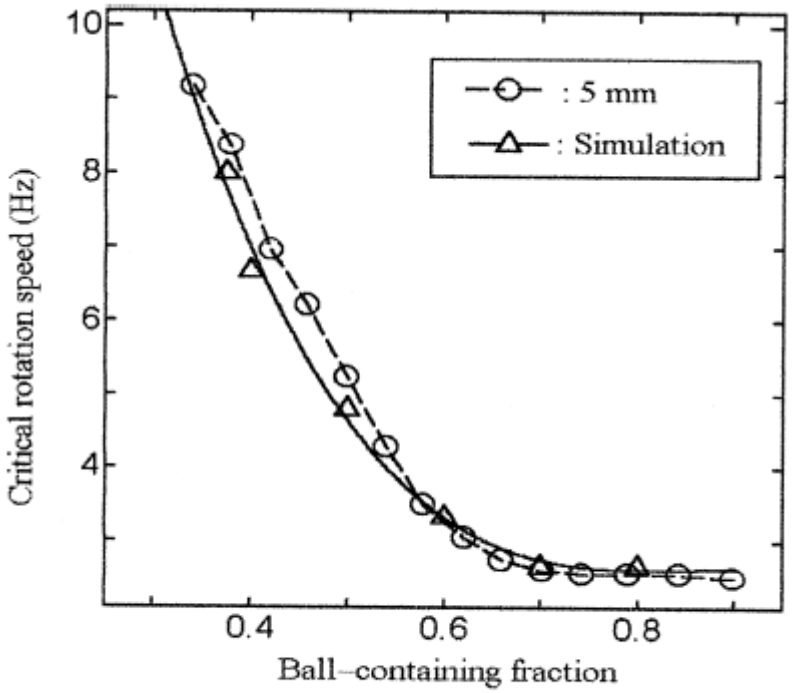

Fig 5. The relation between critical speed and ball-containing fraction – Watanabe [18]

D. Strong and Weak Points

Following the work of White [61] and later Davis [62], Rose and Sullivan [17] introduced the dimensions of circulating particles in the charge motion model, see equation (2). Watanabe's model, equation (3) gives the centrifuging speed as a function of load fraction. This is clearly an improvement on the Rose and Sullivan model of critical mill speed but does not take into account a real load fraction. The model of Watanabe lacks the details of granular systems (geometry, shape, angles, etc.) that allows for a meaningful classification into distinct flow regimes (rolling, cascading, cataracting). A major omission is the Froude number, a widely accepted scaling, that characterizes types of flows allowing the identification of inertial driven flows that is typical in mineral tumbling mills.

2.6.2 Charge Motion and Transition Zones – Mellmann [15]

Mellmann [15] extended the work of these earlier researchers by introducing the Froude number and hence successfully delineating charge flows into distinct regimes of slipping, cascading and cataracting. He further identified seven sub-types of transverse charge motion.

A. Forms of Charge Motion - Slipping

Generally slipping motion, which can be either sliding or surging, occurs at both low and high speeds when internal mill-liner friction is low. During sliding the charge constantly slips down the walls of the rotating mill and thus appearing to be in a resting position at a small angle of deflection. As friction is increased to surging the charge begins to adhere to the mill wall up to a certain angle of deflection before falling back. This range of charge motion, which can occur even at high speeds, is industrially undesirable and can be prevented through good liner designs.

B. Forms of Charge Motion - Cascading (tumbling)

This range of motion covers charge slumping, rolling and cascading types. When mill-liner friction is increased to the point where the charge can move at the speed of the mill wall in lifting, motion changes to cascading (or tumbling) motion. At lower rotational speeds continues slumping of the charge slanting surface (avalanching) can be observed. This phenomenon Mellmann [15] termed a "slump cycle" and found it to be dependent on rotational speed, particle size and cylinder diameter. As mill speed is gradually increased some particles may begin to roll down the nearly static charge surface with more charge in the *en-masse* (plug-flow region) replacing them in a cyclic motion about the "*eye*" (CoC) of the

charge. The unset of cascading is observed when the charge assumes a kidney shape whose height increases at increasing mill speed. The author found that cascading, however, occurs mostly at very high speeds.

C. Forms of Charge Motion – Cataracting

With sufficient friction and at relatively high speeds the motion of the charge in grinding media mills is observed to change from cascading to cataracting. This motion range is characterized by particle projection into free fall at the departure shoulder until they impact the mill shell at the toe region. In cataracting the particle trajectory is shorter than the circumference of the inner mill inner wall and there exist a net outward force that tends to centrifuge the charge. Centrifuging is, therefore, characterized by particle attachments to the mill shell. The author discusses the difference between partial and complete centrifuging: partial centrifuging occurs when the outermost balls of the charge stick to the mill shell while complete centrifuging is said to be achieved when the entire charge form concentric rings with the mill wall. He noted further that complete centrifuging only occurs at extremely high speeds.

D. Charge motion Transition Zones

Mellmann [15] presented a primary picture of the transition behaviour between the various forms of charge motion. He developed new mathematical models while critically analysing existing calculations.

I. The Idea of An Agitated Bed

Studying particles undergoing cascading motion Mellmann establishes the Froude number (F_r), which is a characteristic criterion that delineates charge motion in rotary mills into its salient classifications and allows for a better study of their boundaries. The Froude number is the ratio of the centrifugal force to that of gravity, equation (4).

$$F_r = \frac{\omega^2 r}{g} \tag{4}$$

One implication of this criterion is that a particle lying in the outermost orbit will have its radial position $r = R$, the radius of the mill and is therefore centrifuging. This defines a critical Froude number $F_r = 1$ indicating that the centrifugal and gravitational forces acting on the particle are in equilibrium. Accordingly Mellmann proposed that the mill rotational speed assumes a critical value as defined in equation (5).

$$n_c = \frac{30}{\pi}\sqrt{\frac{g}{R}} \approx \frac{42.3}{\sqrt{D}} \tag{5}$$

Equation (5) is today a widely employed model for determining the operational speed in most grinding mill industries. Mellmann [15] also established the relationship between the Froude number and the critical mill rotational speed as in equation (6).

$$F_r = \left(\frac{n}{n_c} \right)^2 \tag{6}$$

II. Transition from Slipping to Cascading Motion

Mellmann [15] suggests Froude number (F_r) plays no role in the transition from slipping to cascading motion. According to him this range of charge motion is affected mainly by the filling degree. He uses a moment balance around the cylinder axis in which a wall friction moment (M_2) is called into play to offset the effect of burden caused by the mill load slip (M_1) as shown in figure (6).

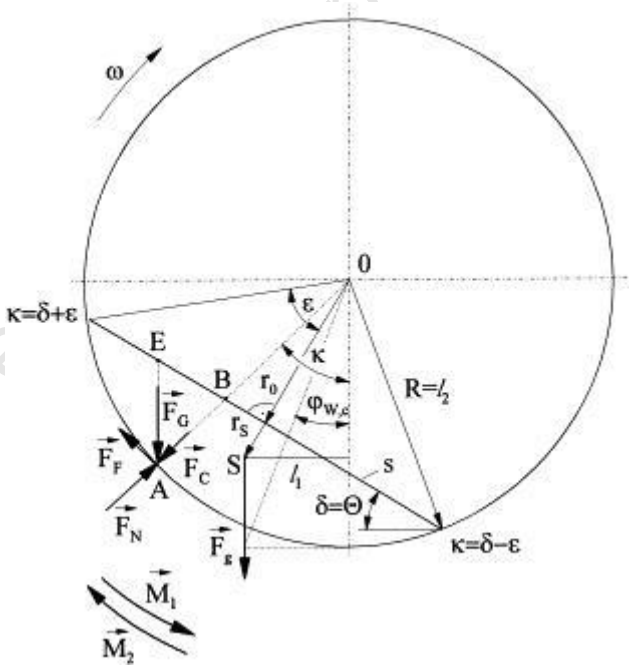

Fig 6: Schematic of the bed cross-section and moment balance around the cylinder axis – Mellmann [15]

From figure (6) transition to cascading occurs when:

$$M_2 > M_1 \tag{7}$$

With:

$$M_1 = \frac{2}{3}\rho_b g R^3 \sin^3 \varepsilon \sin \delta \tag{8}$$

And:

$$M_2 = \mu_w \rho_b g R^3 \ 1 + F_r \quad \varepsilon - \sin \varepsilon \cos \varepsilon \tag{9}$$

In equations (8) and (9), (δ) is the angle of repose, (ρ_b) is the bulk density, (ε) is the filling angle and ($\mu_w = \tan \varphi_w$) characterizes the effective frictional coefficient of the bed material to wall over the entire solid covered wall. Combining equations (7) to (9) the transition condition is obtained as the wall friction coefficient given in equation (10).

$$\mu_w > \frac{2 \sin^3 \varepsilon \sin \delta}{3 \ 1 + F_r \quad \varepsilon - \sin \varepsilon \cos \varepsilon} \tag{10}$$

According to Mellmann [15] when the condition as set out in equation (10) is met charge motion changes from the range of slipping to the range of cascading.

III. Transition from Cascading to Cataracting

The detachment of particles from the mill shell, describable by considering the radial equilibrium of forces, is regarded a minimum requirement for particles throw-off into the gas space (free-flight) and determines the transition to cataracting motion. In figure (7), when the component of the gravitational pull at (P_2) along the radial line balances the centrifugal force, radial equilibrium exist and the line of detachment is described by equation (11).

$$\frac{\omega^2 r}{g} = \sin\zeta \tag{11}$$

According to Thales' Principle this line of detachment describes a circle with diameter (g/ω^2), which corresponds to the perpendicular distance of the pole of forces from the axis of rotation (OP). The orbital radius (r) then becomes a function of the angle (ζ) which determines the point of detachment and hence the transition point from cascading to cataracting. Mellmann establishes this transition criterion as in equation (12).

$$\frac{\omega^2 r}{g} > \sin\zeta \tag{12}$$

Figure (7) shows the Davis circle [62] superimposed on the mill centre and its point of intersection with the mill profile forms a logarithmic line (*OP*). This logarithmic line indicates that particles in the proximity of the mill wall (that is, particles with $r = R$) will be thrown off into free fall first. Hence Mellmann concludes centrifuging occurs when the outermost balls of the charge form a concentric ring with the mill shell. This is expected to be achieved at the point where $\zeta = 90°$. The angle (ζ) is referred to as the departure shoulder angle and is an important geometric location in the determination of power draw in industrial tumbling mills.

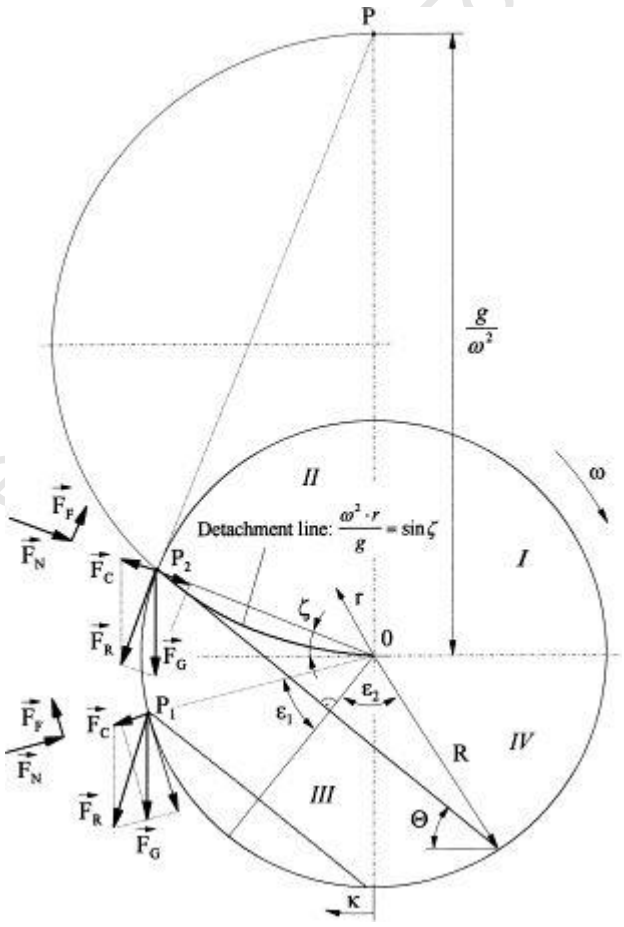

Fig 7: Force balance around particles in different quadrants of the cylinder cross-section – Mellmann [15]

E. Strong and Weak Points

The work of Mellmann [15] was perhaps the first significant step towards linking wall friction coefficient (μ_w) to mill filling angle (ε) and the Froude number (F_r), equation (10). With the onset of cascading motion a dynamic angle of repose (θ) which determines the new position of the centre of gravity of the charge is brought into play giving a critical wall friction coefficient that is a clear improvement on earlier reports. However we found his model to be valid only for low speeds due to its dependence on over-simplified charge geometry. Mellmann's transition to cataracting model is also based on the assumption of a Froude number of unity ($F_r = 1$) at the point of charge centrifuging. This assumption does not take into account the effect of friction at the mill wall (mill liner design) which plays a significant role in increasing the angle at which the charge deviates from the mill profile.

2.6.3 Grinding Regions in Rotary Grinding Mills – Powell and McBride [24]

The key theories of comminution remain largely conceptual when related to charge geometry and motion in tumbling mills. Relying on numerous assumptions these theories are, nonetheless, not well defined and this may explain why they are inconsistently addressed in the literature. In the literature, different authors use differing definitions of the various grinding regions in tumbling mills, however, they mostly do not hold over a full range of possible operating conditions. An example is the definition of the angle of repose which was formally assumed to be the line joining the toe and shoulder of the charge. A simple deficiency of this definition is the fact that at high mill speeds (of over 80% of the critical) this definition becomes meaningless. Through characterizition of the grinding regions of the charge in a tumbling mill, Powell and McBride [24]

discussed the influence of varying the operating conditions on charge motion and the formation and intensity of different grinding regions. Their discriptions can be used to improve milling efficiency.

A. Grinding Regions (zones) in Industrial Tumbling Mills

The authors developed numerical schemes for determining the grinding regions in tumbling mills as shown in figure (8). These regions are now briefly described.

I. En Masse

This is the bulk region of the charge moving in an upward direction. This region lies between the equilibrium surface and mill shell and is also referred to by some authors as the plug-region. Charge in this region remains in contact with the mill shell till at the point of departure. The grinding mechanism in this region is by abrasion and attrition which affects the shear stress dissipation and hence the power draft of the mill.

II. Equilibrium Surface

This is the surface that separates the rising *en-masse* charge from the descending charge (free/cascading charge). This surface is usually identified by the turning point of the charge trajectories. The authors determined this surface by joining the horizontal and vertical equilibrium surfaces to form a continuous surface. The *eye* (CoC) of the charge is located along the equilibrium surface. According to these authors when the circulation plane of the mill is divided into families of horizontal, vertical and radial control surfaces, a cumulative count of particles

passing through any point along these control surfaces would yield a local maximum when the particles pass through the centre of circulation (CoC).

III. Centre of Circulation (CoC)

This is the axis about which all charge in the mill circulates and is a point of zero velocity of the particles. According to the authors it can be determined by the intersection of the horizontal and vertical equilibrium surfaces. The path of the particles in the *en-masse* region form concentric rings of decreasing radii that converge on the CoC.

IV. Centre of Mass (CoM)

This represents the equilibrium point to which all the mass of the charge can be condensed. It is that point at which, if the total mass of the charge were to be placed, will exert the same torque about the centre of the mill as the full tumbling charge. This point was determined by statistical averaging.

V. Rate of Circulation

The authors define the charge circulation rate as the number of circulations a particle makes per mill revolution. In order to establish this, they tracked particles from a given angular position relative to the CoC. A complete circulation is seen when the particles return to their original position forming a complete circuit of the CoC. In this way the number of charge circulations could be compared to the number of mill revolutions giving a normalized value which they termed "circulation rate" of the charge, see equation (1).

VI. Angle of Repose (AoR)

This is the cascade angle of the charge and has also been defined as the angular position of the CoC [23. 24]. In comminution the angle of repose is commonly employed to describe the torque exerted by the charge and consequently the power drawn. Powell and McBride [24] presented the most user-independent definition for the repose angle by noting that "the tangent to the equilibrium surface at the CoC is perpendicular to the radial line passing through the CoC. This condition is uniquely defined because the equilibrium surface has a different curvature to the mill shell, so only one point on the surface can have a tangent perpendicular to a radial line." According to Govender [23] closer inspection of the geometric implications of the Powell and McBride definition reveals that the angle of repose of the tumbling charge is simply the angular position of the CoC.

VII. Departure Shoulder

This is the uppermost point at which the particles begin to deviate from the mill shell. According to the authors it can be determined as the point where the sum of the radial distance of the particle and its radius is less than the radius of the mill. The significance of this definition is underscored by the fact that the charge may still travel along the surface of a lifter bar, or may still be travelling in an upwards direction, prior to entering cascading/cataracting motion.

VIII. Head Shoulder

This is the highest point of the charge trajectory or the maximum y-coordinate of all particles. The authors proposed the concept of a departure and head shoulder in describing a shoulder region. This region starts at the departure shoulder and ends at the head shoulder which position may not lie along a lifter bar or the mill shell.

IX. Bulk Toe

This is defined as the point of intersection of the tumbling charge with the mill shell. The bulk toe is determined from the intersection of the equilibrium surface with the mill shell when all direct impact events are excluded. The authors determined the bulk toe as the point where the extension of the horizontal equilibrium surface from the inflection point (defined as the point at which the horizontal equilibrium surface moves in an upwards direction towards the impact toe) intersects the shell.

X. Impact Toe

This is the region where the cataracting charge impacts on the mill shell or the highest point at which cataracting material impacts the mill shell. The authors determined its location as the point at which the horizontal equilibrium surface intersects the mill shell.

B Strong and Weak Points

Powell and McBride [24] used the definitions of the various grinding regions to validate DEM by comparing the output from DEM simulations to the output from

experimental work. The comparison of DEM predictions with experimental measurements where conducted in a quantitative manner with standard statistical techniques applied to assess the accuracy of the predictions. A possible application of their work is in lifter designs where the definitions of the bulk and impact toe angles can aid in the quantification of the incidence and severity of impacting. Hence their work provides an improved capability to test the output of computational models and to provide an analytical comparison of different milling conditions. However, besides the relationship between the angle of repose and the CoC the authors failed to provide any other connecting relationships between the other geometric parameters as described by them. The link between breakage and grinding zones in these mills is usually through the mill power draft. This dependence was not investigated in their work.

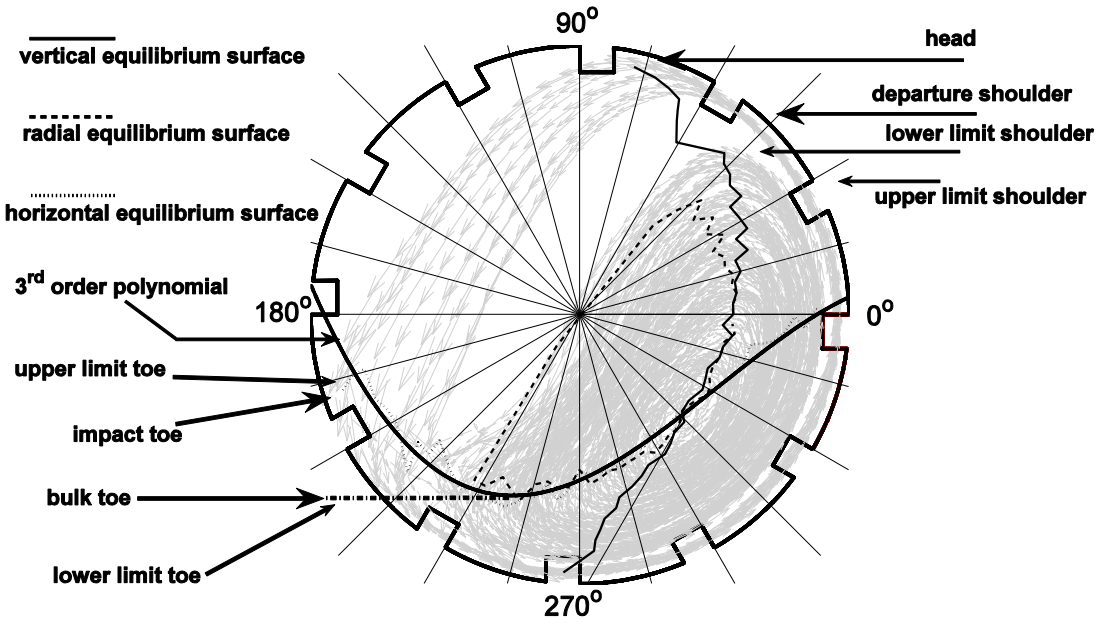

Fig 8: Grinding regions in rotary grinding mills – based on the definitions by Powell and McBride [24]

2.5.4 Positron Emission Particle Tracking of Charge Particles in a Scaled Industrial Tumbling Mill - Govender et al [58]

A. Introduction

The aggressive environment in most milling operations has been largely responsible for the increasing use of the end-window filming technology by many mill models. The specialized nature of such highly tweaked empirical models negates *apriori* the ability to extrapolate beyond the mode of operation for which they were determined. However, limited resources and environmental constraints make it difficult to develop greater predictive capabilities.

B. Positron Emission Particle Tracking (PEPT)

The authors discussed the use of a technique developed at the University of Birmingham for tracking the motion of a radioactive tracer that emits positrons while decaying. These positrons can combine with electrons and annihilate producing two anti-parallel gamma-rays that can be detected by positron cameras. The position and hence the motion of the tracer can then be determined by triangulation.

They conducted a series of experiments with tracers as small as 1mm which were tracked in a 300mm diameter tumbling mill rotating at speeds of up to 90% of critical mill speed. Glass and rock particles were activated using a 36MeV (^{3}He) beam which converts a small fraction of oxygen atoms to (^{18}F), a positron emitter with a 110minute half-life. Copper particles were labelled with (^{64}Cu), (with half-life 12.7 hours) by irradiation with 14 MeV neutrons.

C. Experimental Work

The experimental rig consisted of a mill constructed from High Density Polyethylene (HDPE), which was specifically chosen because of its low gamma ray attenuation. The mill set up used a DC drive with step-down gear box, torque sensor and a reticulating pump for wet experiments that recirculated the slurry. The grate and mill cover were manufactured from clear acrylic, so that the discharge dynamics of the mill could be observed using video and photographic cameras. Conditional blue stones of specific gravity 2.75 made up the mill load and the size distribution of the mill load conformed to typical comminution practices. Wet runs contained 30% slurry solids by volume. Using static loading for calibrating the torque sensor allowed them to develop characteristic power curves for varying load and speed.

D. **Trajectory Data**

The mill geometry was generated by using position markers (positron emitting glass spheres) placed on the mill shell and optical switches placed on a given lifter bar. The mill shell and the position of the lifters could then be constructed by slowly rotating the drum and these were then synchronized with that of the tracer. The trajectory fields derived from PEPT were typically noisy and required some pre-filtering before any meaningful analysis could be performed. The researchers, therefore, used a piecewise smoothing spline to construct trajectory data for typical PEPT runs (no slurry) and wet runs with re-circulating slurry.

E. Strong and Weak Points

The researchers found that the power draw varied linearly with mill load but non-linearly with the mill speed. At a load of (40%), typical to industrial practices, the

power curve peaks at around the characteristic (75%) of critical speed. Their work provides an explanation for the limitations of empirical models and other robust descriptions as due to lack of detailed measurements or poor measurement techniques. Numerical descriptions based on Darcy's law and Ergun's equations were found to be insufficient to fully realize flow dynamics. Charge dynamics such as transport through the mill, porosity, circulation rate and viscosity require accurate quantification in the dynamic context of a rotary mill before they can be efficiently utilized. In this context PEPT data is well suited to extracting these descriptions and hence open up a whole new avenue that has hitherto not been considered. However the authors did not present detailed analysis of how PEPT data could be used to model power draw, breakage and the mechanisms of material transport and discharge in these mills.

Chapter Three: Particle Tracking Techniques

3.0 Introduction

In recent years the need for novel technologies to surpass the end-window filming system has become essential. As an optimization tool computer simulation has been widely employed in aiding an understanding of milling performance measures such as size distribution, charge motion and mass flow rate. The use of novel technologies such as X-rays and tomography has not only greatly enhanced the visualization of particle dynamics in these mills, but also contributed to the validation of computer simulation as basic tools for predicting mill performance. In this chapter we discuss three experimental techniques which have recently been employed in the comminution studies. These are X-ray photogrammetry, Positron Emission Tomography (PET) and Positron Emission Particle Tracking (PEPT).

Since its accidental discovery by Rontgen [77] in the late 18^{th} century X-ray imaging technology has been widely used for diagnostic radiography and crystallography. X-rays, used to create images for medical diagnosis, are the second most commonly used medical test [78]. However, application of the technology to non-medical use has been slow. This may be due to projection errors associated with X-ray images arising from refraction in the material medium. Hence another radiation that has been widely used in medical as well as

non-medical research is the gamma-ray emitted from radioactive nuclei. These rays are known to traverse material media without the trouble of refraction associated with X-rays. With these gamma-rays, tomography methods can be used to map the equilibrium distribution of a working fluid that has been labelled with a radionuclide that decays by either electron capture or positron emission. Positron emission tomography (PET) is still widely used in medicine as a non-invasive technique but its use in non-medical areas has limited success due to the large number of equipment used and their associated storage space requirement and cost. Position emission particle tracking (PEPT) was developed to track the motion of a single particle labelled with a radionuclide, rather than a labelled working fluid. An important aspect of PEPT has been its successful application to non-medical areas [57, 58]. This has come about because PEPT allows the visualization and characterisation of particulate kinetics and kinematics within aggressive industrial environments, such as tumbling mills, flotation cells and powder mixers.

These three techniques have allowed researchers an *in-situ* perspective of particle dynamics deep within the charge of experimental mills. Of these techniques, the biplanar X-ray filming method [23] and PEPT have similar capabilities in that they can be used to track the motion of a single positron emitting tracer particle. However, unlike the X-ray imaging system PEPT allows the use of real charge within a scaled industrial tumbling mill. Data derived from PEPT experiments conducted at the University of Birmingham and at the iThemba LABS have been used in this thesis. The fundamentals of X-ray vision analysis, positron emission tomography (PET) and positron emission particle tracking (PEPT) are discussed herein.

3.1 X-Ray Vision Systems

In the spectrum of electromagnetic energy are radio waves, visible light and X-rays. X-rays can be absorbed, reflected or refracted depending on the material medium. Images can be produced if the refracted X-rays can be detected by suitable equipment [78]. An X-ray vision system is therefore equipped with an X-ray generator and an optical X-ray detector [23, 78]. Such a system is the Biplanar Angiographic Equipment (BAE) at the Chemical Engineering Department, the University of Cape Town. This equipment is designed primarily for medical diagnosis and is used to assess the condition of a patient's heart valves by introducing a contrasting medium (a semi-opaque dye) into the patient's heart valves. The development of such a remarkable technology has been one of the most important advances in medical history.

Govender [23] discussed the setup and operation of this equipment and a brief summary is given here.

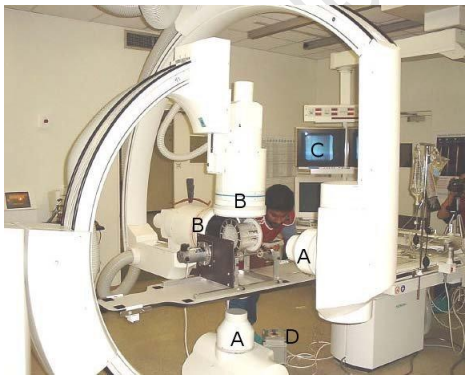

Fig 9: The biplaner angioscope at the University of Cape Town - picture by Govender [23]

X-rays produced within a contained unit, marked with the letter *A* in figure (9), pass through the patient (in this case a Perspex mill) resulting in scintillations of varying contrast on the input screen of the image intensifier, denoted by the letter

B in figure (9). The scintillations are then recorded by a high speed digital camera, positioned directly behind the image intensifier, which is eventually sampled at effective rates of 12, 25, 50 or 75 frames per second depending on the requirements of the cardiologist. The sampled images are also relayed to an on-line television screen, indicated by the letter *C* in figure (9), providing a quick in-situ diagnosis of the heart valves. The usual procedure following the angiographic assessment is to download the relevant X-ray image scenes to a personal computer for further diagnostics, including writing the data to compact disc [23].

This technology has recently been harnessed for non-medical purposes. Powell and Nurick conducted a series of studies in which they used a similar X-ray equipment to track the motion of particles in an experimental mill [79 - 80]. In these studies they tracked steel, lead and glass balls of varying sizes in a Perspex mill (diameter Ø190 mm and length 97 mm). The mill was fitted with lifters ranging from 1.8 to 10 mm and charged with 6 mm plastic beads to investigate charge motion. The most important outcome of their investigations included the description of an equilibrium surface, a technique for uniquely obtaining the centre of circulation (CoC) and an estimate of the angle of repose that was found to be valid for all mill speeds. Others such as Govender [23] and McBride et al [81] have reported studies in which an X-ray vision system was employed to reconstruct the 3D motion of particles in an experimental mill.

3.1.1 Advantages of X-Ray Vision Systems

Advantages include:

- High accuracy (0.15mm error),
- Low density systems (plastic, perspex, wood),
- Well suited to idealised studies of fundamental charge motion.

3.1.2 Disadvantages of X-Ray Vision Systems

Disadvantages include:

- Cannot study real systems,
- 3D data cumbersome to process,
- Experiments limited to approximately 100 seconds,
- Scale is an issue (140x140x140)mm is max.

3.2 Positron Emission Tomography (PET)

The use of Positron Emission Tomography (PET) in medical research has been well documented [82 - 85]. As the first non-evasive technology, PET was developed primarily to track the intake of a metabolic fluid labelled with a radionuclide that decays by beta plus (β^+) decay emitting a positron [84]. The emitted positron rapidly annihilates with an electron producing a pair of 511KeV photons which are known to travel in almost opposite directions to each other. Simultaneous detection of both gamma-rays – in detectors placed on either side or around the body - defines a line passing close to the tracer's position. The first set of gamma-cameras was designed by Hal Anger in 1957 which used a set of vacuum tube photomultiplier (PMT) [84]. More recently PET detectors are designed on the cristal-photonmultiplier technology ("head" on gantry) that allowed the tracer activity within the body to be detected and its trajectory can be reconstructed when a large number of such instantaneous events are detected at different angles [85]. According to Herman [86] this reconstruction is usually achieved by backprojection followed by deconvolution. This method correlates the detected high-energy annihilation photons with their points of origin.

The annihilated 511 keV photons from PET experiments were known to have considerable penetration of structural materials and for many years it was considered vital to harness the technology for industrial use. However, the

technology had a number of disadvantage which included among others: cost - it required a large number of small crystal-photomultiplier gamma detectors which could be expensive; mobility – many items made the system relatively immobile; data - extremely large quantities of data were required to achieve reasonable reconstruction; field of view - required extended field of view achieved by scanning the subject along an appropriate axis which was clearly inappropriate for dynamic studies; timescale - conventional PET imaging produces a 2D image on a timescale of around a minute, or a 3D image in around one hour, and it is thus only suited to observing steady-state conditions or slow transients [57]. Adapting the technology to industrial applications, therefore, presented some complications and this was exacerbated by the difficulty in accommodating several items. The answer to this problem then was to produce a pair of detectors based on multiwire technology with a higher spatial resolution but at lower cost.

Motivated by its manifest industrial importance the University Of Birmingham, in 1984, working closely with the Rutherford Appleton Laboratory in London, The UK, designed and constructed a positron camera based on a relatively cheaper form of Multiwire Proportional Counter (MWPC). The system uses conventional tomographic methods to map the equilibrium distribution of a labelled working fluid placed within the field of view of the cameras. The Birmingham positron camera is capable of reconstructing both 2D and 3D PET images over a large field of view with a spatial resolution of 8mm [57].

A number of publications have detailed the successful application of positron emission tomography (PET) with the Birmingham cameras [57, 87 - 94]. The descriptions provided give an insight into the steps taken in addressing the disadvantages of the crystal-photomultiplier – listed above - used in medical PET.

Placing the medium within the field of view of the two positron sensitive cameras allows for both 2D and 3D images to be obtained. By backprojecting each detected event along its line of sight unto an imaginary plane assumed to lie

midway between the detectors the images can be reconstructed and the internal distribution of the emitting radionuclide obtained. However, gamma-ray scattering of the annihilated photons produces blurred images and the problem of attenuation are often observed along different lines of sight of the backprojected events [93]. Suitable weighing methods are used to correct this attenuation through careful measurement of the total observed attenuation along different lines of sight. Deconvolution of the backprojected events from a point source is applied to remove the tails from the resulting backprojected image [86].

The Birmingham positron camera allows for all azimuthal angles of emission within the field of view of the detectors to be detected with some probability [57]. However, it is a known fact that the sensitivity of the detectors increases as one approach the axis of rotation whilst the spactial resolution decreases with distance from the camera face. Therefore an "angle limit" can be specified such that events corresponding to the lines of sight cutting the plane at angles greater than this limit are accepted. This removes the problem of the varying sensitivity of the cameras arising from the large field of view or solid angle over which both annihilation photons are detectable – although this is often achieved at the expense of discarding a large quantity of data [87].

Obtaining useful images require a large quantity of data to be randomly collected – sometimes in the order of 10^5 detected events may be required which may contain both genuine and random coincidences (near-simultaneous events on two opposite detectors). The genuine and random coincidences are reconciled through normalization by subtracting the random images from the real images. This normalization process can also compensate for the effect of dead-time, and for the decay of the radiolabel with time [86].

The Birmingham positron camera has a data logging rate of approximately 3000 events per second leading to slow flow processes [57]. For 2D activity distribution collecting data in the order of 10^5 events can take up to 30s. However,

obtaining sufficient data to achieve reasonable reconstruction of the 3D activity distribution can often take more than an hour.

The Birmingham positron cameras were found to have very low detection efficiency - about 15% - and low coincidence recognition rate which made them unsuitable for medical use due to dose considerations. However, this limitation did not affect its application to non-medical studies and the first pilot scale studies were successfully completed in 1987, which involved a study of lubrication in aero-engines and gearboxes [88].

3.3 Positron Emission Particle Tracking (PEPT)

Bemrose et al [89] developed an algorithm for tracking multiple particles in positron emission particle tracking (PEPT) and concluded that reasonable reconstructions of the trajectory of an emitting radionuclide can be achieved, with only a small number of detected events, if a single positron-emitting particle is used instead of a working fluid. They suggested that, provided such a particle motion follows that of the surrounding fluid, the anti-parallel 511KeV photons would be emitted from a point source (the tracer) whose location would be the point of intersection along the lines of sight of the two annihilated photons. This point is obtained by triangulation and according to Parker et al [57] can be determined to within the resolution of the Birmingham positron camera if a large number of such events are recorded.

3.3.1 The Birmingham Positron Camera

Parker et al [57, 94] and Hawkesworth et al [93] have provided detailed descriptions of the Birmingham positron camera and these descriptions are summarized hereIN – see figure (10). According to these authors a sensitive field

of view can be achieved with a pair of 40x50 cm^2 multiwire proportional chambers. These chambers are filled with isobutane and Freon maintained at atmospheric pressure. Each chamber has 21 cathode planes separating a stack of 20 anode wire planes held at a potential of 3.5 kV. The cathode planes, which are 50 μm strips each 2.2 mm wide with 8 mm gaps, are made of lead plated onto standard glass-reinforced plastic electric circuit boards which acts as the principal photon convertor, and provides the relevant positional information. A gamma-ray interacting in the lead by photoelectric absorption or Compton scattering releases a fast electron into the gas, which initiates a Townsend avalanche adjacent to the neighbouring anode wire, and this can be detected as a voltage pulse on this anode and its two neighbouring cathodes [94]. The strips on successive cathodes are orthogonal, so that the two cathodes either sides of each anode provide the 2D (x, y) coordinates of the ionizing events. These coordinates are read using the delay line principle. According to Parker et al [57], in each detector, a number of cathode planes are placed such that their strips run in the same direction allowing them to be read out via a single delay-line. This gives a total of four delay lines of 300 ns long serving the two detectors. Hence at singles rate of above 10^5 (s^{-1}) there is a significant probability of multiple events occupying one of the delay-lines simultaneously. This problem is remedied by discarded events if more than one pulse occupies the delay line of one of the detectors simultaneously, though this effectively limits the useful coincidence logging rate to a maximum of around 3000 events per second.

The timing signal for coincidence recognition is provided by the fast pulse from the anodes and the total efficiency for detection of 511 keV gamma-rays is about 7% [94]. The overall detection efficiency for a pair of annihilation gamma-rays is reduced by a geometrical factor dependent on detector separation. The maximum reported efficiency is as low as 0.5%, at chamber separation of maximum 75 cm [93]. The timing resolution of the Birmingham camera is approximately 15 ns and its detection efficiency is also highest at the centre of the camera and reduces outwards. According to Parker et al [94] for conventional limited-angle

tomographic imaging (with the detectors stationary) the resolution of the Birmingham camera is defined as the Full Width at Half Maximum (FWHM) of the backprojected image of a point source (the Point of Spread Function PSF). For a central point source in this geometry the resolution is about 8 mm in the x- and y- directions and 18 mm in the z- direction (along the mill axis).

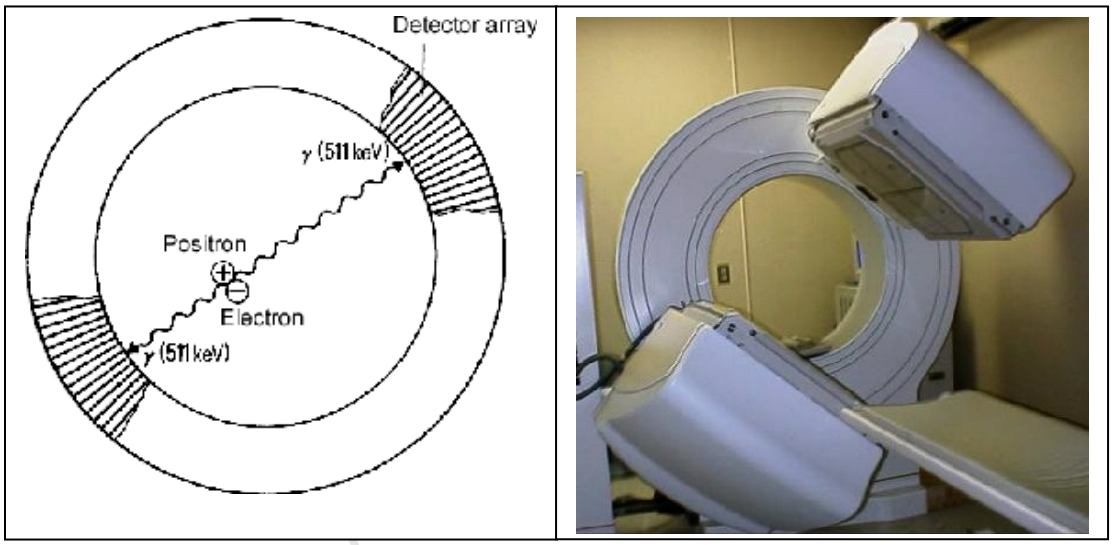

Fig 10: The positron camera at the PEPT unit, University Of Birmingham, showing the location algorithm

The speed and accuracy of tracking depends on the activity of the tracer and the amount of material which the gamma-rays have to traverse to reach the detectors. The data collected from PEPT experiments are stored in list mode on a computer since this gives good flexibility, allowing for subsequent processing. The most important data include: the camera orientation angle, the detection coordinates of the two photons (usually 6 bytes of positional data for each valid event recorded corresponding to the x- and y- coordinates and the anode plane numbers in each of the two detectors); the instantaneous real time and live time (measured in 100 ns units); and any other important parameters describing the state of the system under study. Algorithms for tracking the motion of the particle can be developed

to select events from this list and the trajectories are grouped together in time and space.

3.3.2 Labelling Tracer Particles

Tracer particles for PEPT studies can be labelled either directly or indirectly. In the indirectly method a suitable radionuclide can be attached to the surface of the tracer, giving a large activity, though this activity is liable to erode in wet or abrasive conditions. In the direct method selected particles for labelling are placed directly under the beam from a Cyclotron. Using direct activation, the limit on activity per particle is determined by the heating which the particles can withstand due to energy deposited by the cyclotron beam [84, 94]. If too high a beam current density is used the particles disintegrate. Since for a given current density the activity produced is proportional to the cross-sectional area of the particles, there is a lower limit to the size of particle which can be satisfactorily labelled in this way for high speed tracking. The lower activity produced in a small particle gives a lower event rate from the positron camera but accurate tracking is still possible at low speeds [57].

Hence the most important factors that determine the choice of tracer particle include: the emitter must be chemically compatible with the fluids and other materials involved; sufficient activity to give useful images in an acceptable time; a long enough half-life to cover the duration of the study, but not too long as to leave residual activity in the test objects after completion of the study [57, 84, 94].

Radionuclides that have been used in many recent PEPT studies include ^{68}Ga, ^{18}Fe, ^{22}Na and ^{64}Cu with half-lives ranging from 68 minutes to 2.6 years.

Gallium-68 (^{68}Ga) is produced from a ^{68}Ge/^{68}Ga in-house generator without requiring the use of an onsite cyclotron which makes ^{68}Ga the most important

positron emitter used for labelling peptides in nuclear medicine [84]. The parent, Germanium-68 (^{68}Ge), is accelerator produced and decays by electron capture with a half-life of 270.8 days. It has a strong affinity for metal oxides or organic materials making it unsuitable for use as radiolabels. However, its long half-life allows the generator to be used for a long time – sometimes up to a year – providing a continuous supply of ^{68}Ga at reasonable cost [85]. According to Schuhmacher et al [85], ^{68}Ga decays by 89 % through emission of 1.29 MeV positrons and by 11 % an orbital electron capture and has a great potential for radiopharmaceuticals. However the half-life of 68 minutes serves ^{68}Ga both an advantage and a disadvantage. While its half-life may be compatible with the pharmacokinetics of many peptides, it is generally agreed that this half-life is too short for most engineering related tracking purposes.

Fluorine-18 (^{18}F) is a good positron emitter with half-life of 110 minutes that can be produced by being placed directly in the beam from the Birmingham MC40 Radial Ridge Cyclotron [57, 94]. The particles are activated using a 36MeV ^{3}He beam, which converts a small fraction of the oxygen atoms to ^{18}F according to the following reactions [57]:

$$^{16}O\ (^{3}He, p) \rightarrow {}^{18}F \quad \text{and} \quad {}^{16}O(^{3}He, n)^{18}Ne \rightarrow {}^{18}F \tag{13}$$

According to Stewart et al [88] this process can produce enough quantities of ^{18}F to supply 10mCi (3.7×10^{9} Bq) daily for studies on operating aero-engines at the Rolls-Royce test bed at Staverton, 50 miles from Birmingham, in the United Kingdom. However, the relatively short half-life of ^{18}F means a new label has to be prepared for each day's study.

In a similar way to ^{18}F, Sodium-22 (^{22}Na) with a half-life 2.6 years can also be produced using the Birmingham cyclotron. It can normally be obtained as a

powder in NaCl and can be sealed inside metal capsules or glass beads to provide readily available labelled particles. Its long half-life makes it useful for calibration purposes and also for sealing into beads and pellets for particle tracking studies, where the source can be subsequently retrieved [87]. However, positron emission from a tracer labelled with ^{22}Na will be accompanied by the emission of a gamma-ray of energy 1274 keV, which is difficult to distinguish from the 511 keV annihilation photons, resulting in a spurious trajectory [94].

Copper particles are labelled with ^{64}Cu (half-life 12.7 hours) by irradiation with 14MeV deuterons.

3.3.3 Particle Tracking Algorithm

The approximate location of the particle should ideally be a point in space where all uncorrupted gamma-ray trajectories meet to within the resolution of the camera. This is normally regarded as the point that minimizes the sum of the perpendicular distances to the various trajectories, and is known as the minimum distance point for a set of trajectories [94]. According to Parker et al [94], for (N) detected events, this minimum distance point can be calculated from the mean distance relationship in equation (14).

$$\bar{d}_N = \frac{1}{N}\sum_i d_i \,, \tag{14}$$

However, as well as reducing the detection efficiency, interaction with the intervening material generates a background of scattered gammas. This phenomenon is often referred to as “Compton Scattering” and only 10-30% of detected events remain uncorrupted– see figure (11). This background is removed

by an iterative algorithm whereby an initial estimate of location is calculated from the sample of N detected events, then the events lying furthest from this location (that is all paths with $d > \bar{d}_N$) are discarded and the estimate is recalculated, and this process continues until only a predetermined fraction of the original events remains. Typically, 100,000 events are used in the initial sample, of which anywhere between 50% and 90% are then discarded, giving a final location which is accurate to around 1-2 mm (in 3D), provided the tracer does not move too far during the location interval [57, 84, 94]. With a tracer of optimum activity the Birmingham positron camera is capable of generating 100,000 events per second so that the tracer can be located up to 1000 times per second, enabling accurate tracking at speeds of several metres per second [94].

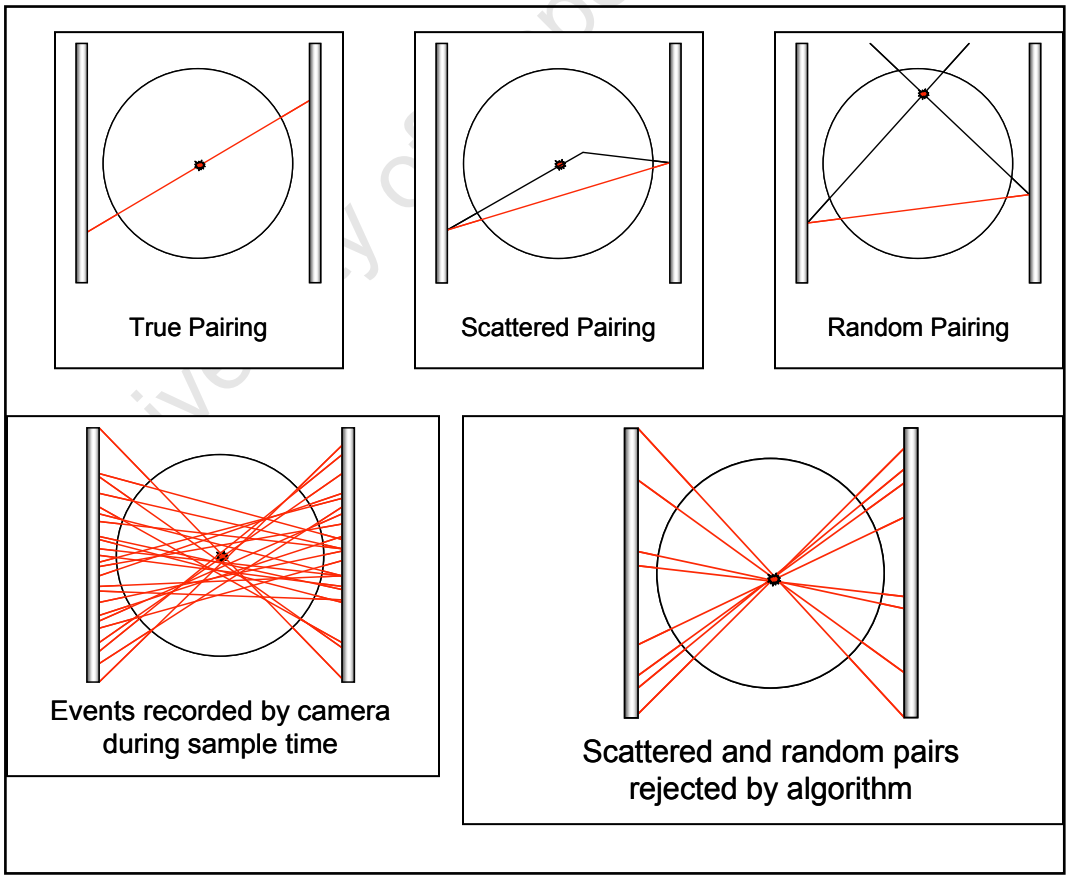

Fig 11: Triangulation – events recorded by scattered and random pairs rejected by algorithm

3.3.4 Data Processing

The anti-parallel high-energy gamma-rays will have pairs of orthogonal coordinates giving six coordinates denoted by (x_1, y_1, z_1, x_2, y_2, z_2) [57]. If the attenuation across the field of view is un-uniform then an "angle-limit" is applied and corrected for the attenuation along different paths. Tails on the point of spread response function (PSF) give the 3D backprojected images a blurred appearance due to scattering. This background can be removed to some extent by Fourier deconvolution of the 3D PSF [86], although this deconvolution is only partially successful.

Due to the effects of radiolabel decay over the period of study and camera dead time, the final images must be renormalized before they are presented as colour maps which can be overlaid with a simplified engineering drawing of the appropriate plane of the subject.

3.3.5 The Ergodic Theory

The ergodic principle relates to the equiprobability of microstates. For conserved classical systems the statistical time averaging of microstates at the same energy levels is taken as proportional to the volume occupied by the microstate. Of central importance is the time to achieve ergodic breaking and its relationship with the state-space average. In this regard systems that evolve for a long time become equidistributed as microstates on the subset revisit the set. Hence for most systems ergodicity is exhibited by the time averaging of their properties over the entire state-space.

The experimental technique, PEPT, was developed to track the trajectory of a single particle, placed within the material medium, which decays by beta plus (β^+)

decay. Results from PEPT experiments can provide details on time averaged velocity, occupancy and mixing Indices. However, this requires an assumption that the time averaged behaviour of a single particle is equivalent to the ensemble average of the bulk. Furthermore, successive visits to each volume element are treated as if they are simultaneous. An important question that arises then is to what extent can the trajectory of a single tagged particle reflect the behaviour of the ensemble *quantitatively*? The answer to this question can be found in the ergodic theory of statistical mechanics.

Statistical mechanics describes the long-time behaviour of mechanical systems which has a dynamics specified in terms of the Hamiltonian equations of classical mechanics [95]. The results of the Hamiltonian equations of motion are that when a system of many particles is isolated long enough it approaches equilibrium whose behaviour can be described by probabilistic methods [96]. The ergodic hypothesis was developed on the Boltzmann and Gibbs formulations of classical (equilibrium) statistical mechanics. This hypothesis describes a microcanonical ensemble by any or all of three approaches: its micro and macro variables, a density function approach and the equal to a priori probability approach [97].

The ergodic theory provides solutions to the problems of microscopic equilibrium and the application of a constant density function to the ensemble. The theory is, therefore, based on mathematical analysis to understanding invariant measures in dynamic systems – measures that are preserved by some function under certain conditions on the function and space under consideration. These invariant measures are considered suitable generalizations of equilibrium points and periodic orbits of dynamic systems which can perform micro-macro connections via time averages [97]. Hence the ergodic theory yields two important definitions; that of the microscopic equilibrium and micro-canonical ensemble [95 - 98].

Definition I: The microscopic equilibrium (ensemble) of a dynamic system (τ^t) are its invariant measures.

Definition 2: Let (T^t) denote a Hamiltonian flow. The micro-canonical ensemble is the invariant measure $(d\xi)$, where $(d\xi)$ is the natural volume measure.

In order to fully understand the significance of these two definitions we may need to return to the operational definitions of quantum statistical mechanics which is concerned with determining the averages of certain operational variables. According to Dter Haar [98], if $\langle\alpha|X|\alpha\rangle$ is the average of (X) in the quantum state $|\alpha\rangle$ then the average of (X) in a situation of statistical equilibrium is given by the Gibbs average:

$$\langle X\rangle = \sum_{\alpha}\langle\alpha|X|\alpha\rangle\rho(\alpha) \tag{15}$$

Where $\rho(\alpha)$ is the probability of observing the system in the state $|\alpha\rangle$ and is given by:

$$\rho(\alpha) = \frac{\exp(-\beta E_{\alpha})}{Z(\beta)} \tag{16}$$

Here (β) is proportional to the inverse temperature and $Z(\beta)$ is the partition function which is a normalizing factor. Since the total probability always sums up to unity we may then have:

$$Z(\beta) = \sum_{\alpha}\exp(-\beta E_{\alpha}) \tag{17}$$

Equations (15) to (17) are fundamental to quantum statistical mechanics and together form the basis for the mathematical digression of the ergodic hypothesis. Using these equations one can develop four governing equations of the ergodic theory as applied to PEPT [95 - 98].

A. The Hamiltonian equations of motion of classical mechanics:

$$\dot{q} = \frac{\partial H}{\partial p}, \dot{p} = \frac{\partial H}{\partial q} \tag{18}$$

Where

$q = (q_1, q_2, \ldots q_nN)$ are vector positions,

$p = (p_1, p_2, \ldots p_nN)$ are momenta coordinates and hence:

$H = H(q, p)$ is the time-independent Hamiltonian operator.

B. The time average functions;

In the limit as $t \rightarrow \infty$

$$f(\xi) := \lim_{t\to\infty} \frac{1}{t} \int_{t_0}^{t_0+t} f(T^s \xi) ds \tag{19}$$

This limit coincides with the average value of (f) over the phase space (Γ) since the time interval is large enough (microscopically) to allow the system to visit all sets of this phase space during the measurement process. Hence:

$$\langle f \rangle := \int_{\Gamma} f(\xi) d\xi \qquad \text{and therefore} \qquad f^{*}(\xi) = \langle f \rangle \tag{20}$$

C. The density function

The density function at time t is given as:

$$\int_{\Gamma} f(\xi)\rho_{\tau}(\xi) d\xi \qquad \text{where} \qquad \frac{d\rho_{\tau}(\xi)}{dt} = 0 \tag{21}$$

The explicit time derivative gives a condition for equilibrium similar to the Liouville equations. It gives a solution of ρ_t = constant, which is equivalent to the Lebesgue natural volume measure ($d\xi$).

D. Equal a priori probability function

This equation attempts to include the Liouville theorem into the density function given in the last section, without which the condition for equilibrium given in equation (15) would be incorrect. If ($T^t\, d\xi$) is ergodic then:

$$\int_{\Gamma} f(T^{t}\xi)\rho_{0}(\xi) d\xi = \int_{\Gamma} f(\xi)\rho_{0}(T^{-t}\xi) d(T^{-t}\xi) = \int_{\Gamma} f(\xi)\rho_{0}(T^{-t}\xi) d(\xi) \tag{22}$$

Equation (22) leads to the general statement of the ergodic hypothesis of classical statistical mechanics: ***The microcanonical ensemble ($d\xi$) is ergodic with respect to the Hamiltonian dynamics***.

If the ergodic hypothesis holds true for these systems then one has a precise mechanical definition of the microcanonical equilibrium ($d\xi$) as given in definitions (I) and (II). It must be noted that there are some classes of two-particle mechanical systems for which the Hamiltonian is the sum of the kinetic energy (K) and potential energy (U) and these are the most realistic models in statistical mechanics where the ergodic theory has been rigorously established to be true [95 - 98].

The behaviour of a single isolated particle within a tumbling mill has been investigated by Dong & Moys [99] using multi-exposed photographs with a stroboscope as the light source. Tracking the single isolated particle in time and space allowed the values of the coefficients of restitution and friction to be determined for subsequent incorporation into a DEM simulation study. Their work was, however, limited to two-dimensions which required the user to discern the particle trajectory path from a photograph thereby limiting the amount of data that can be gathered from an experiment. This limitation meant they were unable to effectively capture the behaviour of an assembly of particles within the bulk charge. Baumann et al [100] used the ergodic theory to show that the motion of a single particle is "ergodic" in the sense that the statistical properties of a trajectory in a (1: 1) mixture of big and small particles are very similar to those of the whole assembly. A detailed discussion of this work is beyond the scope of this research.

However it must be noted that not all Hamiltonian systems are ergodic. For a system of independent (non-interacting) particles to be ergodic requires the interactions among its particles be fundamental [98]. There has, however, been no satisfactory description of these interactions. While some argue that the postulates

of the equal to a priori probability can be considered a logical conclusion others think only experimental results can give a final conclusion on this argument. It is however clear that the theory of ergodicity has not presented definitive answers to the problems of statistical mechanics. Some have therefore suggested that it is necessary to limit mixing and ergodicity to suitable variables such that equation (20) holds true for a finite set of observable (f). In this way it may be possible to investigate an ergodic-like behaviour only for a finite set of observables which may vary from system to system. This is the premise of tracking a single particle in positron emission particle tracking (PEPT) and generalizing it to the ensemble.

3.3.6 Advantages of PEPT

Advantages include:

- Moderate accuracy (> 0.5mm error),
- Can study real systems,
- Well suited to industrial systems,
- Tracking 3D data is relatively simpler.

3.3.7 Disadvantages of PEPT

Disadvantages include:

- Experiment duration depends on half-life (½) of particle (such as 110 minutes for ^{18}F),
- Scale is also an issue (0.5x0.5x1.2)m is max.

3.4 PEPT at iThemba LABS

A recent PEPT laboratory was opened in 2009 and situated at iThemba LABS, an Accelerator-Based Science national laboratory, Faure, South Africa. The iThemba

LABS operates a (k = 200) separated sector cyclotron, and a 6 MV van de Graaff accelerator. The cyclotron routinely produces both light and heavy particles for nuclear physics research and medical PET use. The PEPT laboratory within the iThemba LABS is called "PEPT Cape Town" and houses the ECAT 'EXACT3D' (Model: CTI/Siemens 966) positron emission tomography (PET) camera, see figure (12),

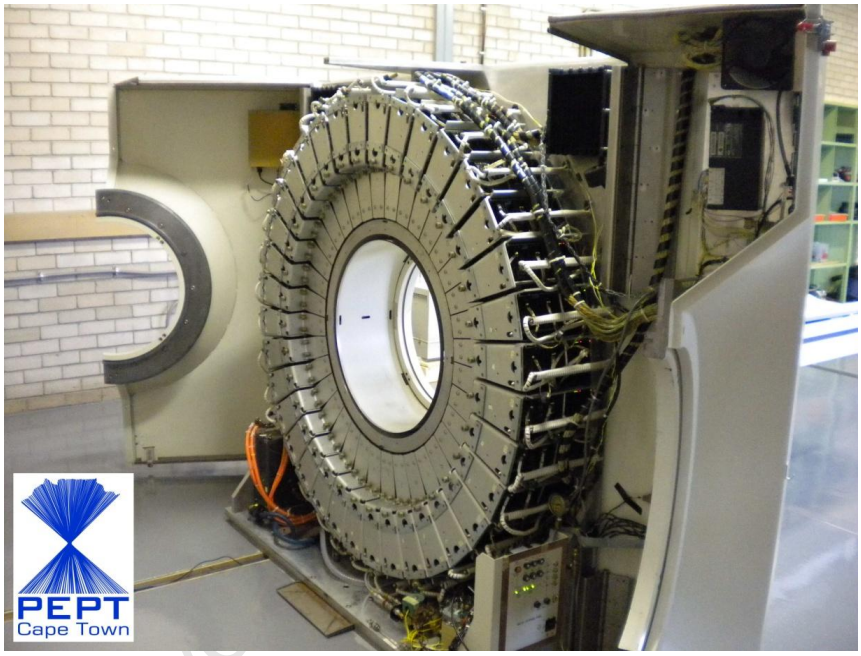

Fig 12: The ECAT 'EXACT3D' PET camera at PEPT Cape Town consisting of 48 rings of 576 BGO detector elements.

The scanner has been in use for medical research at the Hammersmith Hospital (UK) from where it was donated to the University of Cape Town. The ECAT 'EXACT3D' was originally designed with the aim of achieving high sensitivity and high resolution for PET-based research [101, 102]. The PEPT scanner consists of 48 rings of standard bismuth germinate detector elements (each 4.39 mm transaxial × 4.05 mm axial × 30 mm deep, grouped in blocks of 8 × 8). With a ring diameter of 82 cm, which can produce an axial field of view of 23.4 cm, the

camera is significantly larger than other ‘standard’ ring geometry PET cameras. A small Cs-137 source moving under hydraulic pressure in a small helical tube carries out attenuation. The data hardware system can maintain a sustained data acquisition rate of about 4 million coincidence events per second. The mean spatial resolution of the scanner for PET imaging has been measured [102] to be 4.8 ± 0.2 mm FWHM (transaxial, 1 cm off-axis) and 5.6 ± 0.5 mm (axial, on-axis).

Chapter four: The Experimental Work

4.0 Introduction

Detailed particle tracking experiments were conducted at two novel laboratories and the data so obtained is used in this research. The first set of data is derived from the experimental program conducted at the PEPT unit, University of Birmingham (UB). Recent experiments were conducted at PEPT Cape Town, situated at the iThemba labs outside Cape Town.

4.1 The Experimental Rig

The experimental rig used in both sets of experiments, figure (13), consisted of a mill constructed from High Density Polyethylene (HDPE), a DC drive with step-down gear box, torque sensor and a reticulating pump for wet experiments that re-circulated the slurry. The details of the mill are as follows: internal length of 270 mm, internal diameter 300 mm, number of lifters 20 and discharge grate open area ~ 30%. The mill shell, the lifters and the pulp lifters are manufactured from HDPE which has a specific density of 0.95. HDPE is chosen specifically for this type of experiment because of its low gamma ray attenuation. The grate and the mill cover are manufactured from clear acrylic, so that the discharge dynamics of

the mill can be observed using video and photographic cameras. Initial experiments at UB covered milling configurations spanning 6 sizes of the tracer particle between 2mm and 8mm, 5 loads between 12.5 and 50 percent of the mill volume and 5 speeds between 55 and 100 percent of the mill critical rotation speed. Further experiments at the iThemba LABS were designed to extend the range of mill speeds from 20% to 90%, stepped by 5%, with two lifter profiles used. The effective grinding length (EGL) of the mill is the same as the internal length of the mill for all loads since the mill is flat ended.

For the various models reported in this thesis, parameters are obtained directly from the *in-situ* flow field of the PEPT tracer particles.

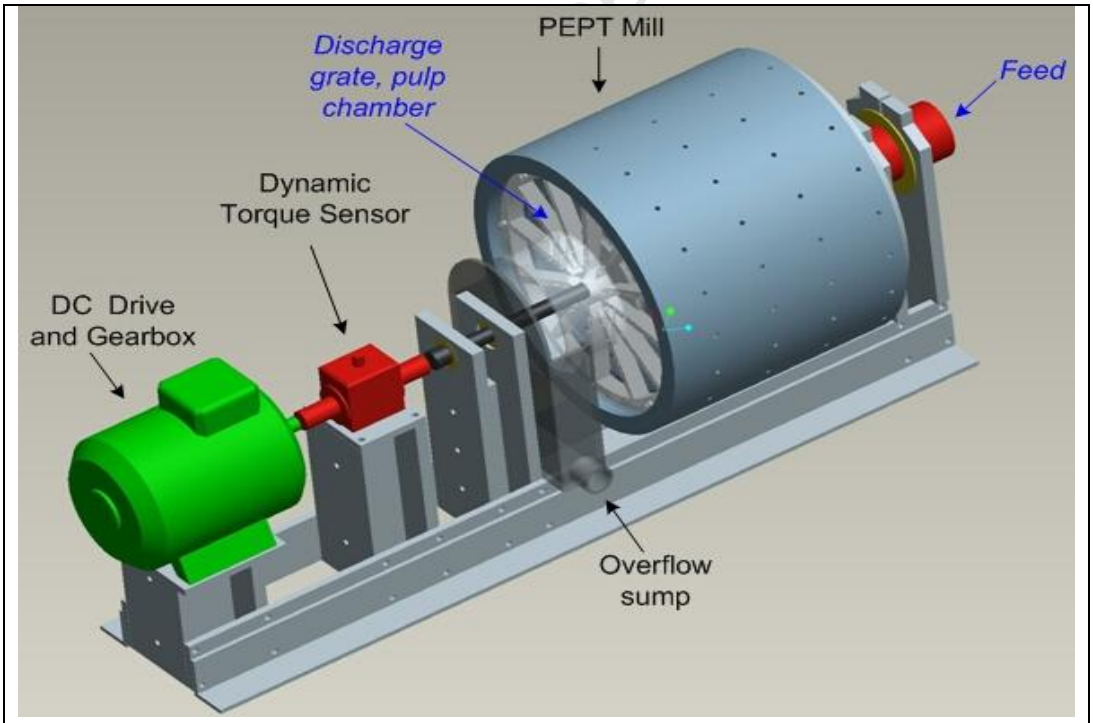

Fig 13: Experimental mill employed in positron emission particle tracking experiments

4.2 PEPT Experiments at University Of Birmingham (UB)

The experimental tumbling mill setup at the Birmingham positron imaging centre was driven axially with a torque sensor (T20MN supplied by HBM Instrumentation) placed between the DC drive and mill to measure the dynamic fluctuation of the mill load, figure (14). This improved the reliability of the torque readings as direct measurements were taken from the mill shaft rather than the mill shell. The torque sensor was calibrated using static loading and torque readings were captured using an analogue-to-digital converter. The DC drive has a power delivery capacity of 0.55kW with a 24.6 gear ratio which is well suited to frequency control of the motor speed leading to good process control mobility, energy-savings, precision, and a high degree of automation.

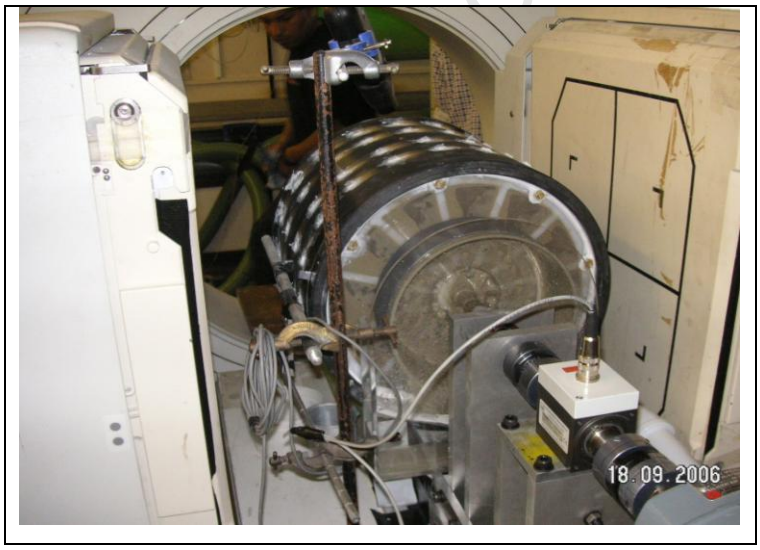

Fig 14: Torque sensor on shaft connecting mill and motor at the UB.

4.2.1 Experimental Matrix

A total of 150 experiments were conducted and the experimental matrix was as shown in table (1) below. Rows represent mill speeds in percentage of critical, see

section (4.2.2), while columns represent the mill load fraction in percentage determined as in section (4.2.3). The intersection of rows and columns represent the experiment number.

Table 1: Experimental matrix at UB

1 mm tracer particle							**2 mm tracer particle**					
%	**12.5**	**25**	**31.25**	**37.5**	**50**		**%**	**12.5**	**25**	**31.25**	**37.5**	**50**
90	1	6	11	16	21		**90**	26	31	36	41	46
80	2	7	12	17	22		**80**	27	32	37	42	47
75	3	8	13	18	23		**75**	28	33	38	43	48
70	4	9	14	19	24		**70**	29	34	39	44	49
60	5	10	15	20	25		**60**	30	35	40	45	50
3 mm tracer particle							**4 mm tracer particle**					
%	**12.5**	**25**	**31.25**	**37.5**	**50**		**%**	**12.5**	**25**	**31.25**	**37.5**	**50**
90	51	56	61	66	71		**90**	76	81	86	91	96
80	52	57	62	67	72		**80**	77	82	87	92	97
75	53	58	63	68	73		**75**	78	83	88	93	98
70	54	59	64	69	74		**70**	79	84	89	93	99
60	55	60	65	70	75		**60**	80	85	90	95	100
6 mm tracer particle							**8 mm tracer particle**					
%	**12.5**	**25**	**31.25**	**37**	**50**		**%**	**12.5**	**25**	**31.25**	**37.5**	**50**
90	101	106	111	116	121		**90**	126	131	136	141	146
80	102	107	112	117	122		**80**	127	132	137	142	147
75	103	108	113	118	123		**75**	128	133	138	143	148
70	104	109	114	119	124		**70**	129	134	139	144	149
60	105	110	115	120	125		**60**	130	135	140	145	150

4.2.2 The Experimental Mill Speed

In setting the experimental mill speeds the definition of critical mill rotational speed proposed by Rose and Sullivan [17] was employed, equation (23). Thus the critical speed was calculated from equation 23.

$$N_c = \frac{1}{2\pi}\sqrt{\frac{2g}{D-2r}} \tag{23}$$

Table (2) shows the mill speeds used in the experiments conducted at the University of Birmingham PEPT unit.

Table 2: Experimental mill speed

Critical speed in rev/min	**Experimental mill speed**		
	Rev/min	**Rev/sec**	**% of critical**
77.2	69.5	1.1583	90
77.2	61.9	1.0317	80
77.2	57.9	0.9650	75
77.2	54.1	0.9017	70
77.2	46.3	0.7170	60

4.2.3 The Mill Load

The mill load consists of conditioned blue stone with a specific gravity of 2.75. The size distribution of the charge was chosen to conform to a Rosin-Rammler distribution, see figure (15), where *y* is the cumulative fractional distribution and *x* the particle size in millimetres. Wet runs comprised slurry with 30% solids by volume that completely fill the interstices of a stationary charge. Five (5) mill loads ranging from 12.5% to 50 % were used in a total of 150 experiments.

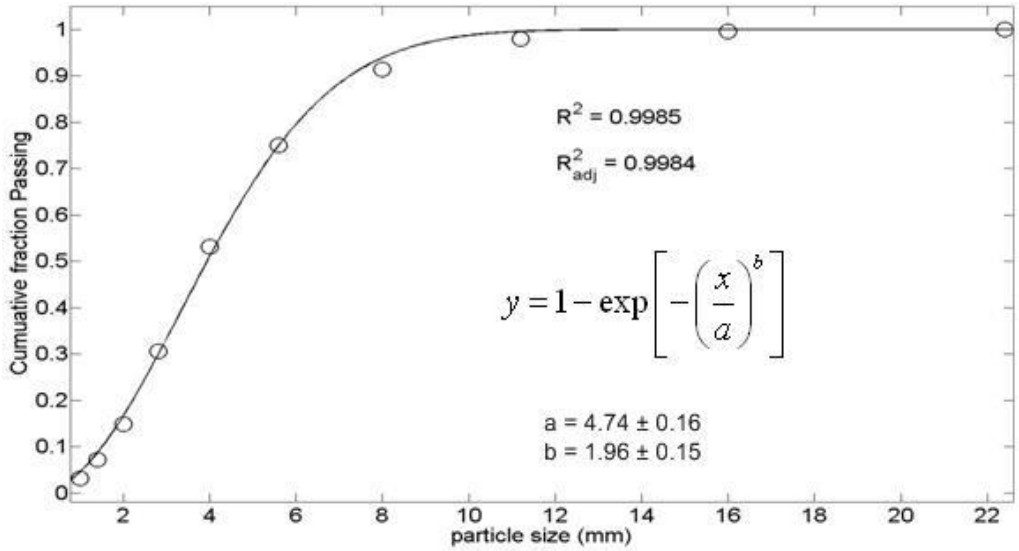

Fig 15: Rosin-Rammler fit to size distribution of blue stone employed in PEPT experiments of tumbling mills.

4.2.4 Torque Sensor Calibration

Before each set of experimental runs "no load" torque measurements were taken in order to measure the power absorbed by the mill inertia. Readings with load were then taken and a linear relationship between the measured voltage and the torque was established with a 0.1% error, see figure (16).

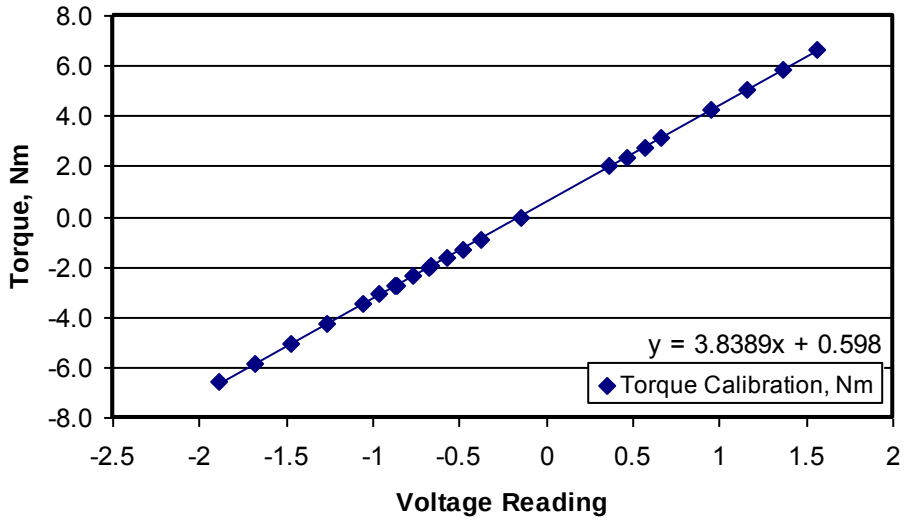

Fig 16: Torque sensor calibration

4.2.5 Trajectory Data

The tracers employed in these experiments were 1mm, 2mm, 3mm, 4mm, 6mm and 8mm rock particles. Figure 17 shows the 1mm, 2mm and 4mm sizes. At the UB the tracers were directly labelled (see section 3.3.2), the selected particle being placed directly in the beam from the Birmingham MC40 Cyclotron. Glass and rock particles were activated using a 36MeV (^{3}He) beam, which converts a small fraction of the oxygen atoms to (^{18}F), a positron emitter with a 110 minute half-life. Copper particles were labelled with (^{64}Cu) (half-life 12.7 hours) by irradiation with 14MeV deuterons.

Fig 17: Illustration of the tracer particles employed in the PEPT experimental work at UB.

The initial trajectory field is obtained in the Lagrangian coordinate system of the PEPT unit [94, 102]. The transformation to the Eulerian system of the tumbling mill is achieved by placing location markers (positron emitting glass spheres) on the front, back and length of the mill. Slowly rotating the drum then yields three circular traces of the mill shell. By noting their relative positions the mill shell can be reconstructed. Figure (18) illustrates two of the location markers fixed to the shell with masking tape.

An optical switch, coupled to the mill and synchronised with the PEPT unit locates the position of a given lifter bar. By noting the position of the optical switch, the rotation of the given lifter, and hence all the lifters, can be reconstructed and synchronised with that of the tracer.

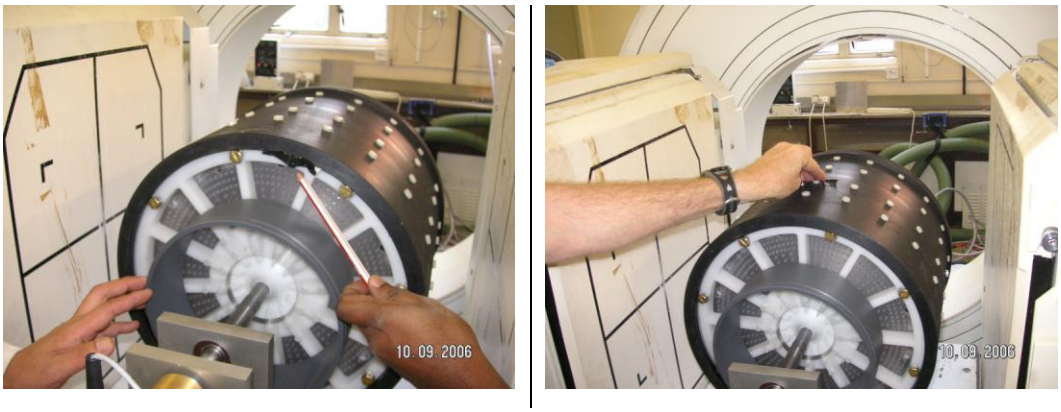

Fig 18: Positron emitting glass beads employed as location markers in tracing out the mill shell

The trajectory fields derived from PEPT are typically noisy and require some pre-filtering before any meaningful analyses can be performed. To achieve this, an algorithm employing piecewise smoothing-splines yielded the most appropriate smoothing – see appendix (C) for details. The result of employing smoothing splines is a partial successful reconstruction of the PEPT trajectory data illustrated in figures (19) to (21) below. These occupancy plots are used to compare real rock charge run in dry and wet conditions. Figures (19 and 20) show the reconstructed trajectory data for typical PEPT runs (no slurry) while figure (21) illustrate typical wet runs with a re-circulating slurry. The trajectory fields are noticeably different between the dry and wet runs.

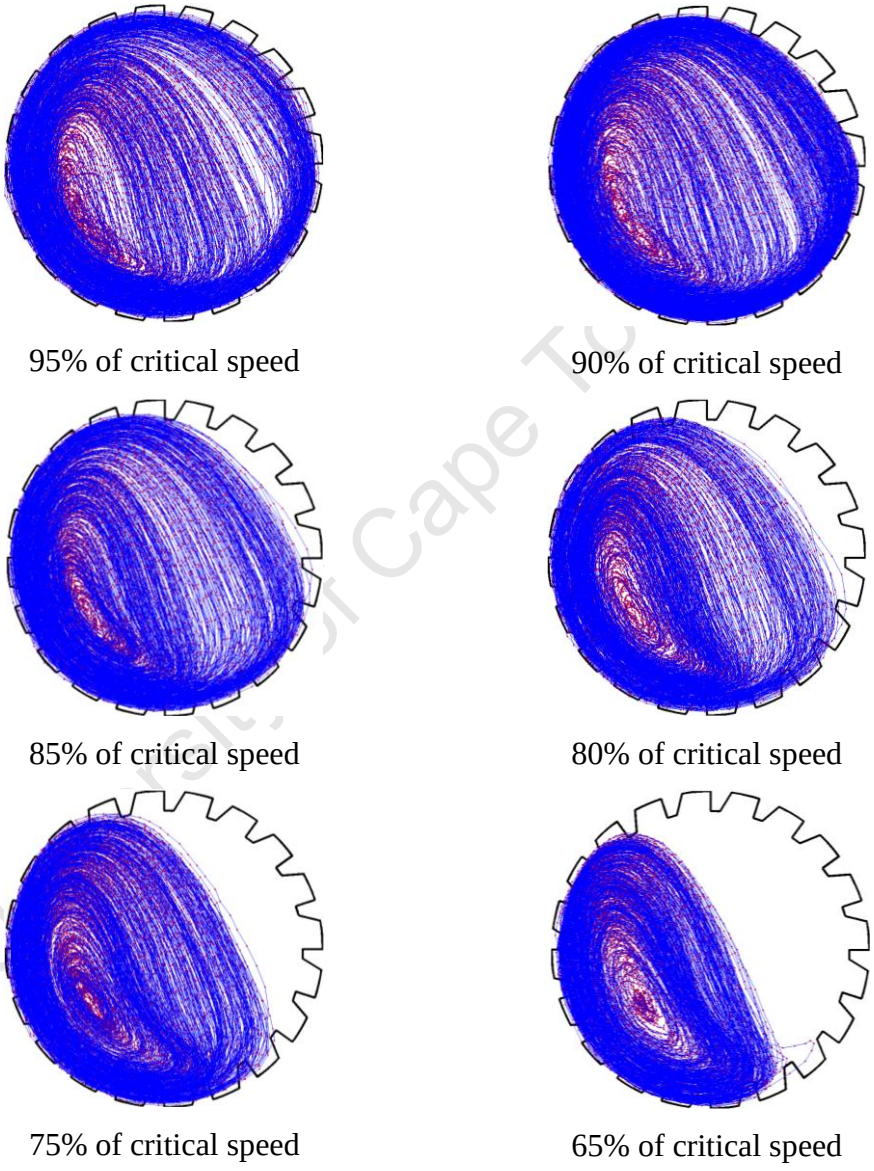

Fig 19: Front view trajectory field of a 4mm rock particle in a mill charged with a 35% dry load. Lifter bars are 19mm high, 20mm wide with a 60° face angle.

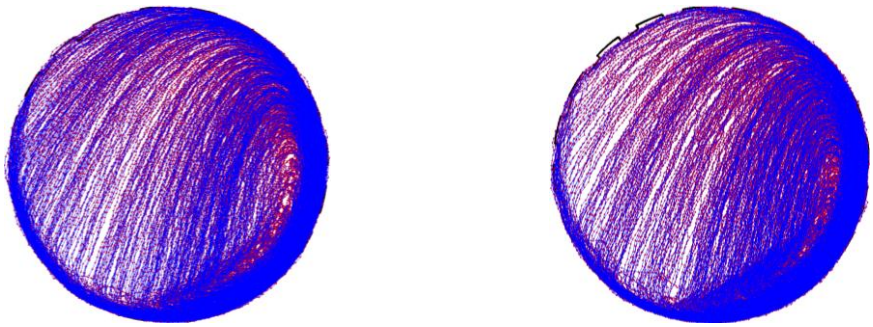

95% of critical speed

90% of critical speed

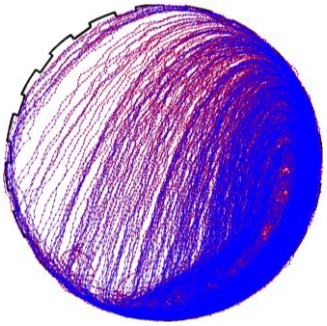

85% of critical speed

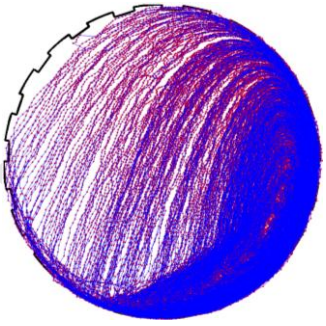

80% of critical speed

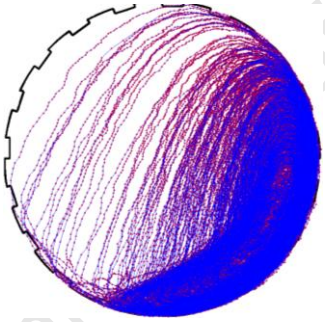

75% of critical speed

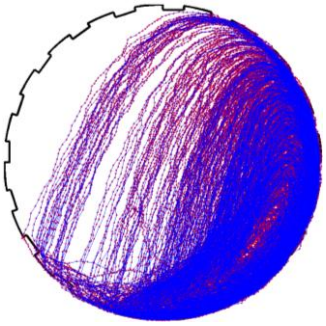

65% of critical speed

Fig 20: Front view trajectory field of a 2mm rock particle in a mill charged with a 15% dry load. Lifter bars are 5mm high, 20mm wide with a 90° face angle.

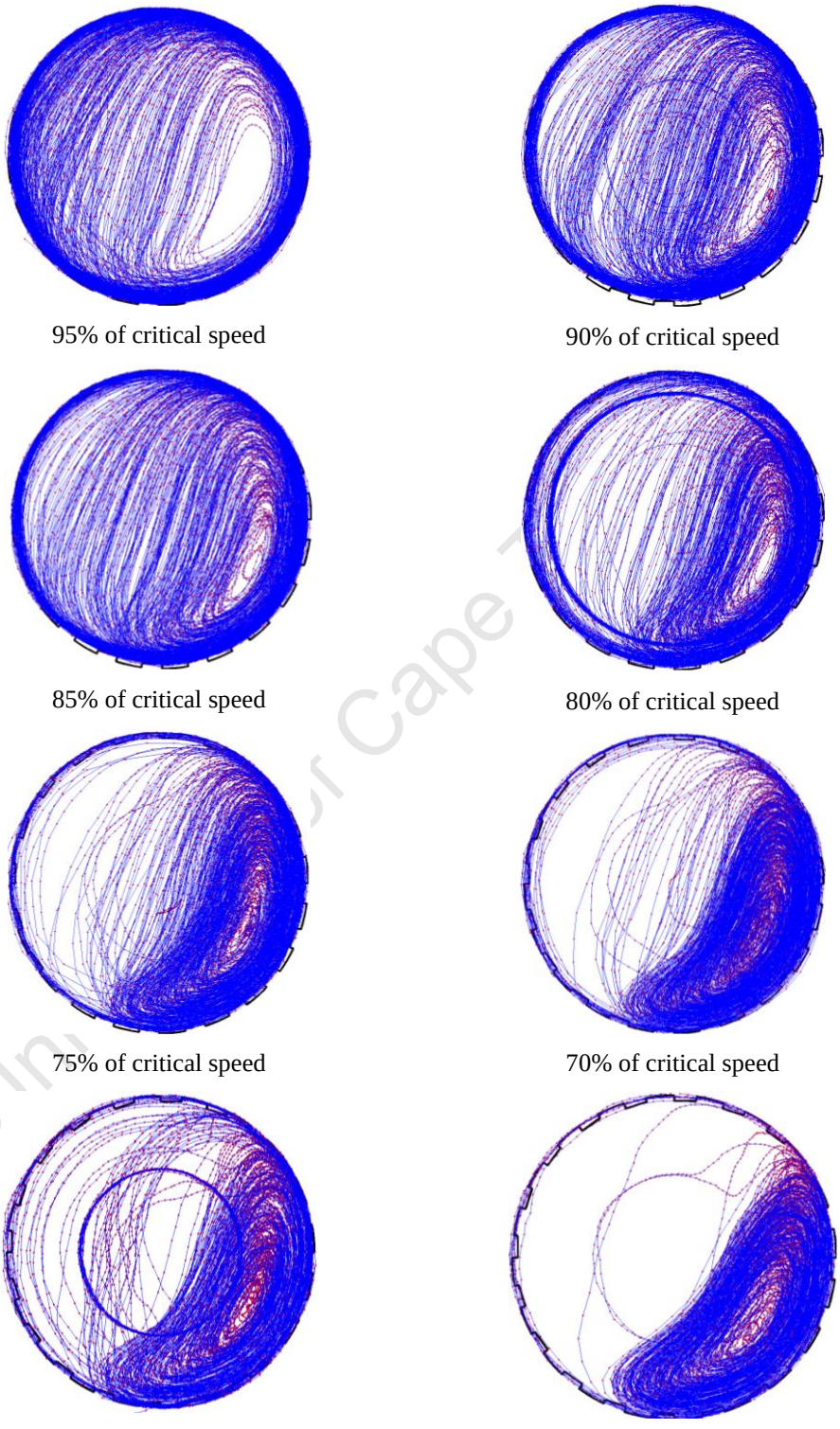

Fig 21: Front view trajectory field of a 1mm particle in a mill charged with a 40% loading and 30% solids. Lifter bars are 5mm high, 20mm wide with a 90° face angle.

4.3 Experiments at PEPT Cape Town

Following the successful analysis of the trajectory data from the experiments conducted at UB a circulate rate model was developed and tested successfully, see section (7.3). The transition conditions from one form of the tumbling charge motion to another is developed, in section (7.1), but required further validation. Essentially experiments were required to extend the range of mill speeds to include lower speeds. These experiments were designed to achieve the following goals:

- Examine steady state conditions in typical tumbling mills.
- Investigate different angular orientations of the departure velocity (velocity at the departure shoulder).
- Test grinding media models developed in thesis for validity.
- Examine influence of mill internal design on energy losses in the grinding environment.
- Model energy losses in the grinding environment and integrate into a power model.

For these experiments mono-sized particles were used (5mm glass beads) with a single tracer of the same size. Two loading conditions at 40% and 0% filling by volume were used with 3mm and 0mm lifter bars. Mill speeds ranged from low (20 – 40 %) to medium (45 – 65 %) to high (70 - 90) stepped by 5% of the critical mill speed as set in section (4.2.2). The details of the mill is as outlined in section (4.1) and the experimental procedure followed closely with the details as outlined in sections (4.2.2) to (4.2.5).

Fig 22: The experimental mill in the ECAT EXERT3D camera system at PEPT Cape Town.

4.3.1 Experimental Matrix

Total of (44) experiments were conducted at PEPT Cape Town with no charge discharge or recycle. Table (3) shows the experimental matrix for the tests at the iThemba labs. In the table, H represents the lifter sizes and Ω is the mill speed in percentage of critical mill rotational speed.

Table 3: Experimental matrix at PEPT Cape Town

Load fraction α = 40%							Load fraction α = 0%					
Ex No	**H (mm)**	**Ω(% cri)**	**Ex No**	**H (mm)**	**Ω(% cri)**		**Ex No**	**H (mm)**	**Ω (% cri)**	**Ex No**	**H (mm)**	**Ω (% cri)**
1	3	90	12	0	90		23	3	90	34	0	90
2	3	85	13	0	85		24	3	85	35	0	85
3	3	80	14	0	80		25	3	80	36	0	80
4	3	75	15	0	75		26	3	75	37	0	75
5	3	70	16	0	70		27	3	70	38	0	70
6	3	55	17	0	55		28	3	55	39	0	55
7	3	40	18	0	40		29	3	40	40	0	40
8	3	35	19	0	35		30	3	35	41	0	35
9	3	30	20	0	30		31	3	30	42	0	30
10	3	25	21	0	25		32	3	25	43	0	25
11	3	20	22	0	20		33	3	20	44	0	20

Chapter five: Analysis of the Experimental Data

5.0 Introduction

The work of White in 1906 [61] and later Davis 1919 [62] brought to the fore, the significance of physical and geometrical parameters associate with industrial tumbling mill operations, in any discussion of charge motion. White [61], somehow indirectly, presented a description of what is today known as the shoulder and toe regions; important geometric parameters in any discussion of the tumbling charge motion. Davis [62], formulated a similar mathematical description for a single particle moving along the mill shell. However, their assumption of no slip led to an over-prediction of the "equilibrium point" (when compared to experiments) which White, in particular, argued was due to insufficient ball loading. Essentially, a higher charge filling increases the normal force exerted on the mill lining which in turn increases the frictional force – an important physical parameter - between the balls and lining. The insufficient loading explanation led to the conclusion of undue liner wear caused by slip and direct impacts. However, the work of these earlier researchers in comminution clearly highlights the value of mathematical modelling of charge motion while making clear the shortcomings of simplified assumptions.

Since then there has been a gradual development in the understanding of charge motion in rotary mills. Gow et al [103] and Fahrenwald and Lee [104] refined the work of Davis and White by including friction in the force balance. But they encountered problems in reproducing the experimental trajectories, especially in short length laboratory mills due to the interference of the end walls. Barth [105] took a similar mathematical approach which led to the prediction of an "equilibrium surface" – a geometric parameter. In a tumbling mill this surface seems to keep particles in a dynamic equilibrium under the action of centripetal, gravitational and frictional forces. Rose and Sullivan [17], investigating the behaviour of the tumbling charge as mill speed – a physical parameter - increases to a critical value, concluded that at this critical speed the outermost layer of balls centrifuge and are said to be stationary with respect to the inner wall of the drum. McIvor [63] conducted a theoretical analysis of single particle behaviour inside a rotating drum and developed an improved model from the existing ones that implicitly included lifter effects – a physical parameter. The conclusion that a particle's trajectory is independent of the mill size [63] is valuable because it implies that the critical speed at which a mill operates is independent of the mill size. Other interesting conclusions, though not directly revealed in his calculations, were that particle trajectory and power draw varied with lifter height and profile respectively [63].

The main aim of this research was to develop a mechanistic model of circulation rate as a function of both physical and geometric parameters in tumbling mills. Physical parameters of typical tumbling mill operations include the mill speed, mill load fraction and mill internal friction. Geometric parameters may include those of the centre of circulation (CoC), the centre of mass (CoM), the angle of repose, (AoR) and the toe and shoulder angular locations. The physical parameters (which are often experimentally measurable) are termed here as fixed parameters and geometric parameters that can be projected as functions of the fixed (physical) parameters are termed non-fixed parameters as in table (4). Schemes were developed and implemented mostly on MATLAB for extracting

these parameters from the experimental data and analysed for trends. Of particular significance are the computational methodologies developed for calculating circulation rates of the charge from PEPT trajectory fields.

Table 4: Fixed and non-fixed parameters

Fixed parameters	**Non-fixed parameters**
Mill speed (Ω)	CoC = CoC(α, Ω, R, Centx, Centy)
Load fraction (α)	CoM = CoM(α, Ω, R, Centx, Centy)
Internal design (μ_w)	$C_{charge} = C_{charge}$ (α, Ω, R, Centx, Centy, ζ, θ_c,μ_w)
Mill radius (R)	$\zeta = \zeta(\alpha, \Omega, R, Centx, Centy, \theta_c, \mu_w)$
Mill centre (Centx, Centy)	

In order to fully appreciate the relationship between these parameters and circulation rate of the charge (C_{charge}) we may need to divide the circulation plane into a number of distinct zones as proposed by Powell [106], figure (23).

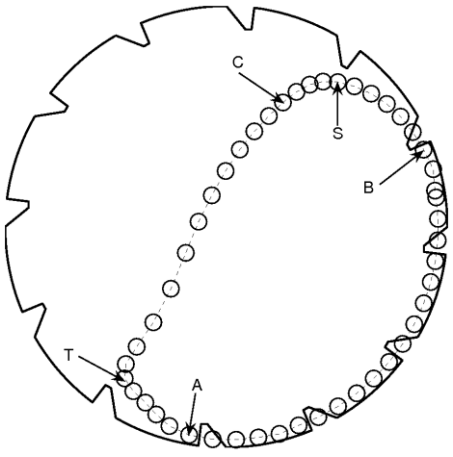

Fig 23: A typical circulation path followed by the ball, showing the various distinct zones

- The circular path in the *en-masse* region, where the ball is lifted up by the rotary motion of the mill - from *A* to *B*. This zone is often referred to as the *quasi plug-flow* region and is used to calculate the slip between layers of the charge.

- The shoulder zone - *B* to *C* - where the ball falls away from the circular path, passes through the maximum height *S*, and then begins to fall down towards the toe region.

- Cascading/cataracting zone - from *C* to *T* - where the ball tumbles down the other descending balls (cascading) or falls freely (cataracting), until it impacts at the toe region. This zone is affected by the shape of the free (cascading) surface.

- The toe region - *T* to *A* - where the ball impacts on the charge and is drawn into the rotary motion of the mill. This is an active region of the charge, and where the interactive forces are greatest as critical mass builds up in this region.

These key zones define a typical trajectory of a circulating particle in a tumbling mill influenced by the operating physical and geometric parameters of the mill.

5.1 Operational Definitions Used

Relevant to the collection and analysis of data for this research was the development of terminology related to the scope of the research and the subsequent schemes for their determination. Based on these terminologies algorithms for calculating charge motion features from trajectory fields obtained via PEPT experiments were developed. In chapters six and seven we formulate

mathematical descriptions of these charge motion features. The theoretical results are then validated against experimental observations.

5.1.1 Mill Speed

The contribution of mill speed in comminution research can be explained by its influence on the energy-particle size relationship [1, 2, 5, 7, 25 - 30, 47 - 49, 59, 60]. According to these researchers any description which relates energy input to the size reduction achievable is essentially empirical and must take into consideration certain conditions. Among these conditions is the operating speed of the mill whether experimental or industrial scale. According to Powell and Nurick [16], different levels of breakage can be achieved by varying the mill speed alone and it is well known that in order to achieve satisfactory breakage one has to run the mill at speeds sufficiently below that of the critical. However, we noted that many of the empirical models that have been developed on charge motion are based on low speeds and as such are not sufficient to aid an understanding of these fundamental relationships in comminution. The rigorous nature of PEPT experiments allows for statistically quantifiable behaviour that can be used to improve current models. Of particular note are the relatively higher speeds used in our experiments, most of which are prominently encountered in the aggressive environments associated with industrial tumbling mill operations.

The critical mill speed model by Rose and Sullivan [17] provides a common basis for comparing different size mills. In a scheme developed for the data analysis the critical mill speed is set at 77.2 revolutions per second, as calculated from equation (23) in section (4.2.2). Mill speeds used, mostly below this value, were projected as a percentage of this critical value (see table 2) and can be manually tweaked, in the MATLAB program between experimental runs, see Appendix (C).

Fig 24: Setting the mill speed with an optical switch at PEPT Cape Town.

5.1.2 Load fraction

Hitherto any discussion on the charge in the comminution of ores has mostly dealt with their influence on breakage descriptions [25 – 27, 47 - 49], circuit design [1] and mill types [1, 54]. The general conclusion is that the range of stresses that can be applied to particles as well as their frequency of application varies with the type of mill, the stage of comminution and the size reduction desired. These factors determine to some extent whether or not grinding media is used in these mills. In high pressure grinding rolls (HPGR) extreme pressures causes the rocks to fracture [107, 108]. Hence they are commonly used as intermediates to supply feed for the later stages of comminution. Ball mills typically use balls, usually of stone or metal, which grinds the materials by impact and/or friction and are commonly used in the manufacture of cement [22, 66, 67]. Attrition in the charge

bed caused by large rocks in autogenous mills leads to fine grinding, which is also called the ”run of mine” grinding, as in South Africa [1, 6, 8, 45, 51].

Fig 25: Load fractions determined by mass at PEPT Cape Town

The load fraction was determined as in section (4.2.3), see figure 25. The total mass of the particles (such as glass beads) is used in the computational scheme for the analysis, see Appendix (C).

5.1.3 Circulation Rate

The rate at which a particle circulates relative to the mill rotation is assumed to be unity by many mill models for the purpose of mill modelling [55, 69, 109 - 114]. This assumption has never been experimentally verified but will appear to imply that the particles impart energy only once per revolution of the mill, irrespective of the mill speed. For such a mill the particles will centrifuge and move with the

mill in rotation giving no chance for useful impact or abrasion that may lead to breakage. However, in a real mill with lifters, a size distribution of particles and a slurry experiments have shown that even if the mill is run at the critical mill speed the circulation rate of the particles will still be greater than unity [6, 12, 15, 16, 18, 23, 24, 58, 61, 79 – 81, 145 - 147]. According to these researchers circulation rate has to be considered as a function of some mill operating parameters. Govender [23] obtained a plot of circulation rate against mill speed showing that it decreased linearly with mill speed. These observations are contrary to current notions regarding energy transfer per mill revolution. It may be argued that the circulation rates of industrial mills are different from that of the Perspex mill used in these experiments. But the general motion of the charge is the same (as confirmed by looking through end-windows of pilot mills and down the trunnion of an industrial mill), so the range should be similar.

In order to extract circulation rates of the charge from the *in-situ* flow fields of the tracer particle two computational methodologies were developed and implemented in a MATLAB program. The first method is based on circulation count of the tracer and the second is a Fourier analysis method. Method 1 was developed on data obtained from the first experiments in Birmingham. Due to the spurious nature of the data obtained from the iThemba LABS, which rendered their analysis cumbersome, we found that this method could not be applied with reasonable degree of success to the second set of experimental data. Because of this a Fourier methodology (method 2) was developed and applied to data from the second set of experiments from the iThemba LABS.

A. Method 1: Circulation Count

Circulation rate has been variously defined as the average number of circulations made by the charge per revolution of the mill [3, 23, 24, 58]. This definition provides a good normalization procedure that eliminates the time dependency of

the charge rotational frequency (circulation rate0. Equation (24) is a mathematical representation of this definition where it is taken as a ratio of the speed of circulation of the charge to the speed of rotation of the mill.

$$\text{Circulation rate of charge } (C_{charge}) = \frac{\text{Speed of circulation of the charge}}{\text{Speed of rotation of the mill}} \qquad (24)$$

Using equation (24) a computational method was implemented based on the circulation count of the tracer particle. The general procedure is as follows:

- Use orientations of trajectory from PEPT
- Get circulation count as (N_c)
- Get the time taken for these circulations from PEPT files as (T)
- Calculate the number of revolutions made by the mill to this end time as (N_m)

- Then

  - N_m = [(No of revolutions) / 60] * [T] (25)

- Then

  - Circulation rate of charge $(C_{charge}) = \frac{N_c}{N_m}$ (26)

From equations (25) and (26) it is seen that circulation rate has units (s^{-1}). This simple but robust method produced good circulation rate values but needed

further smoothing. Appendix C describes a piece-wise smoothing spline method that was developed to tackle this problem. The smoothing made it possible to obtain discrete counts of the tracer circulation when it returned to its original starting orientation (a chosen point). Results were generally satisfactory and the circulation rate values showed clear trends. Table (5) gives circulation rate results for all particle sizes and at different mill speeds and load fractions used in the experiments at UB.

A plot of charge circulation rate against mill speed is obtained, figure (26). An empirical line is fitted to the data with a high coefficient of determination (R^2 = 0.89568). The graph shows the circulation rate declining near linearly with increasing mill speed and this can be explained thus: at low mill speeds the trajectory path followed by the particles, figure (23), is relatively shorter in comparison to the mill shell circumference. Hence the ratio of the speed of circulation of the charge to that of the mill rotational speed - otherwise known as the charge circulation rate (C_{charge}) - is observed to be high. At higher speeds, however, the effect of centrifugal forces tends to increase the particle trajectories hence reducing the circulation rate towards the characteristic value of unity (achieved at full centrifuging).

Table 5: Circulation rates of all particle sizes at different load fractions and mill speeds

Load	Mill speed		Circulation rate
(%) of mill volume	**Revolutions per minute**	**(%) of critical**	**Per second**
12.5	69.5	90	1.242184
12.5	61.9	80	1.314350
12.5	57.9	75	1.325383
12.5	54.1	70	1.379833
12.5	46.4	60	1.543283
25	69.5	90	1.271850
25	61.9	80	1.346750
25	57.9	75	1.345783
25	54.1	70	1.424550
25	46.4	60	1.519700
31.25	69.5	90	1.308722
31.25	61.9	80	1.344361
31.25	57.9	75	1.380050
31.25	54.1	70	1.407950
31.25	46.4	60	1.499417
37.5	69.5	90	1.296650
37.5	61.9	80	1.327033
37.5	57.9	75	1.323667
37.5	54.1	70	1.343133
37.5	46.4	60	1.440450
50	69.5	90	1.226400
50	61.9	80	1.241580
50	57.9	75	1.223800
50	54.1	70	1.300662
50	46.4	60	1.389117

Figure (27) shows the relationship between the charge circulation rate and the mill load fraction. An empirical line is fitted to the data and the trend shows that increasing the mill load beyond a quarter filling will have significant effect on the charge circulation rate. In particular the circulation rate drops to a low value at half mill filling. This can be explained by the inertial effect of the particles at higher mill filling coupled with the resulting increasing porosities [115].

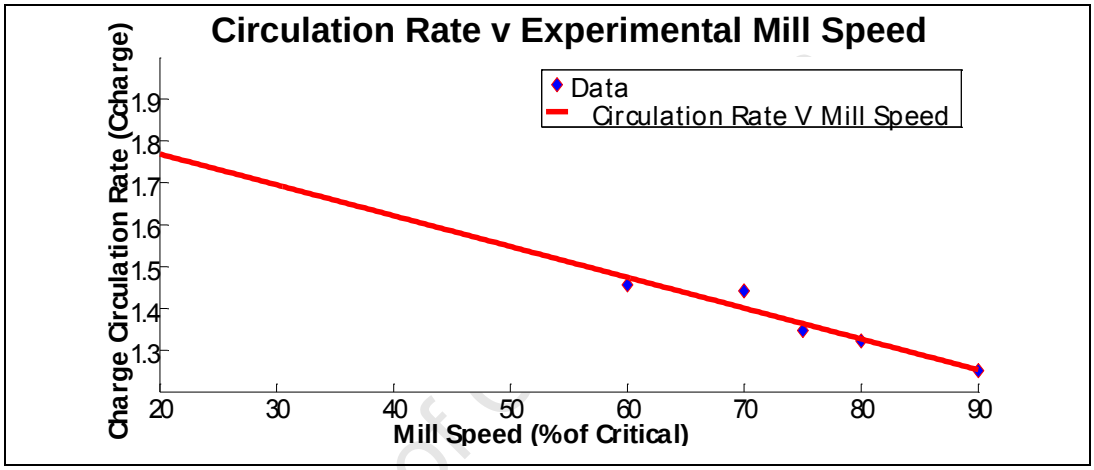

Fig 26: Variation of circulation rate with experimental mill speed.

Investigators have found that the mill volumetric filling can influence grinding mill performances such as the fineness of product grind, grinding media wear rates, throughputs and power draw [12, 21, 28 – 34, 54]. Hence by way of implication is an indirect relationship between circulation rate and mill operating cost. This observation will have serious ramifications for mill models that assume charge circulation rate is constant at unity and hence has no direct relationship with mill operating variables.

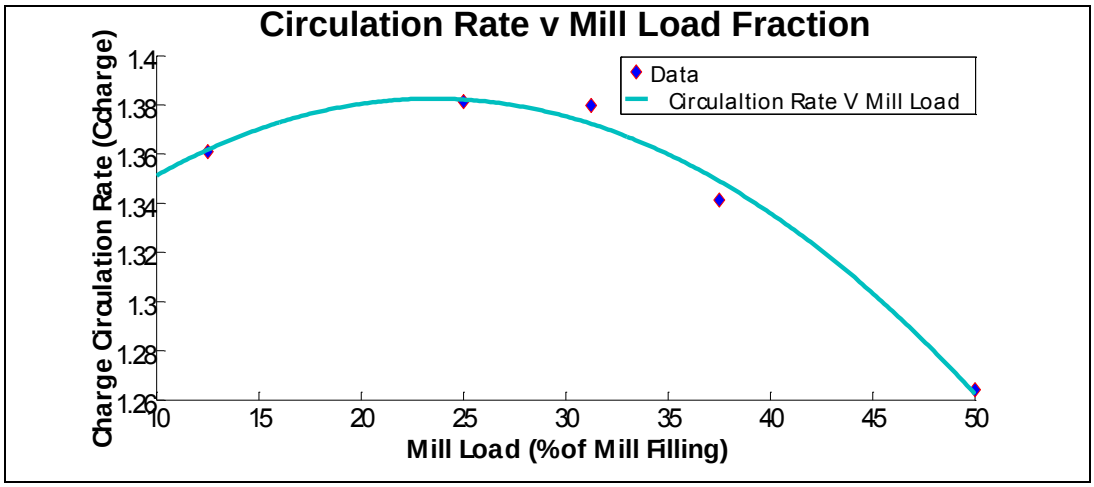

Fig 27: Variation of circulation rate with mill load fraction (volumetric filling).

B. Method 2: Fourier Analysis of PEPT Data

Fourier methods are a powerful and fascinating branch of mathematics. In the analysis of complex functions one may sometimes need to make an educated guess about the identity of a function or the meaning of a result [116]. Until recently this branch of mathematics had very little practical application. With the continued application of computers to mathematics Fourier methods have emerged as central to many parts of science and technology. These methods have found applications in areas such as predicting ocean tides, analysis of noisy signals and mostly in the analysis of periodic data. This ability to analyze periodic data is important in the discussion of circulation rate of data obtained from PEPT. The method was therefore applied to our experimental data with reasonable degree of success. But before we explore the application of this method to PEPT let us first discuss the basic concept of the Fourier methods.

The basic concept of Fourier methods is that a periodic function in its time-domain (the form in which most data are obtained, including PEPT data) can be transformed to its frequency-domain resulting in compressed data that lend themselves to easier analysis. What is most interesting about the method is that these two domains are quite interchangeable. Performing Fourier transform on

spatial data (real space) results in its frequency component called the Fourier space description of the spatial data. The frequency component (Fourier space description) can be turned back to its spatial data (real space) through inverse transformation.

If the raw positional data derived from PEPT is considered a function of time, that is $f(t)$, then the Fourier transform of this function is given by equation (27).

$$F(\omega) = \int_{-\infty}^{\infty} f(t) e^{-i\omega t} dt \tag{27}$$

The resulting function $f(\omega)$ has complex values with frequency magnitudes and phase relationships. Equation (27) shows how the spectral energy of the function $f(t)$ is continuously distributed in the frequency domain [117]. Hence $f(t)$ can be regenerated from the frequency domain function $f(\omega)$ to obtain the time-domain function as shown in equation (28).

$$f(t) = \frac{1}{2\pi} \int_{-\infty}^{\infty} F(\omega) e^{i\omega t} d\omega \tag{28}$$

However, in the analysis of tumbling mill data sampling is necessary, meaning that a discrete formulation of the /Fourier transform has to be employed. That is, we need a transformation process which takes regularly sampled data and returns the values of the Fourier transform for a set of values in the frequency space, provided they are equally spaced or discrete. The equivalent transformation is obtained by replacing the integral by a summation to give the Discrete Fourier Transform (DFT). For N discrete intervals (ie, k = 0, 1, …N - 1), the DFT of a function $f_k = f(t_k)$ is given in equation (29).

$$F(\omega_n) = \sum_{k=0}^{N-1} f_k e^{-ik\omega_n}; \qquad 0 \le n \le N-1 \tag{29}$$

Where

$$\omega_n = n\frac{2\pi}{N} \tag{30}$$

From equation (29) the inverse DFT can readily be obtained as in equation (31).

$$f_k = \frac{1}{N}\sum_{k=0}^{N-1} F(\omega_n) e^{ik\omega_n} \tag{31}$$

In order to obtain reasonable results from this transformation procedure will ideally require (N^2) multiplications and this invariably renders the procedure slow. The DFT can be done in a more efficient manner by the use of the Fast Fourier Transform (FFT) algorithm which often only require (N log N) operations [116, 117]. Currently most DFT are actually performed as FFT were incremental data are used because the results are much faster to obtain. Some properties of Fourier transform are similarity, shift, differentiability and convolution, discussions of which are beyond the scope of this thesis.

Since the discrete time-domain function (such as equation 31) puts a set of values consecutively in time, in order to apply the Fourier methods to obtain circulation

rate values from PEPT experiments we produced the power spectrum, see figure (28). Power spectrum, for the case of the discrete Fourier transform, is a plot of a given signal's power (energy per unit time) that falls within given frequency bins. It is an auto-correlation function that represents the long and short-term correlation within the signal. This allows one to obtain information about the behaviour of the signal (in our case the circulation rate of the charge) and to predict future behaviour (extrapolate). The power spectrum for the discrete case is given in equation (32).

$$P(\omega_n) = \frac{1}{N} F(\omega_n) F*(\omega_n) \tag{32}$$

In equation (32) $F^*(\omega_n)$ is the complex conjugate of $F(\omega_n)$. An interpolation was done on the PEPT data in order to fix the time interval at (Δt) since the data obtained from PEPT experiments are sampled at irregular time intervals. For the tumbling mill scenario the trajectory data in Cartesian coordinate is given as:

$$\mathrm{x}(t_k) = (x(t_k), y(t_k), z(t_k)) \tag{33}$$

Hence the radial position of the particle at time (t_i) can be obtained from equation (34).

$$r_k = \left|\mathrm{x}'(t_k)\right| = \sqrt{x^2(t_k) + y^2(t_k)} \tag{34}$$

(a) Circulation rate at 20% mill speed and 40% mill load

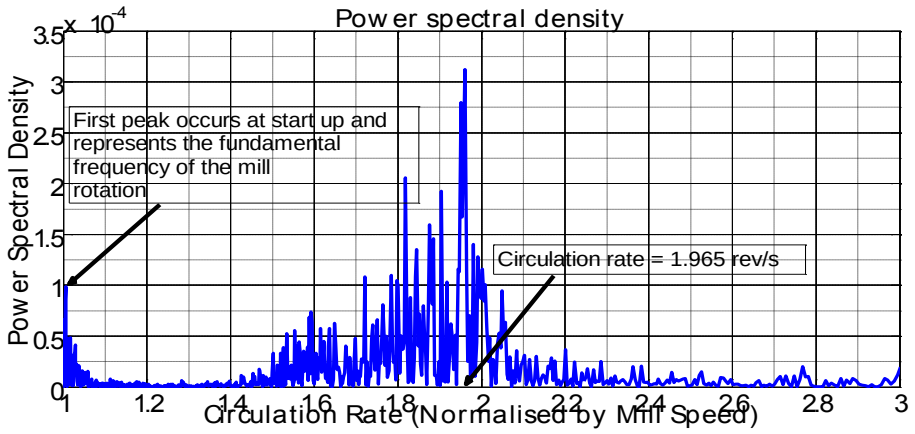

(b) Circulation rate at 35% mill speed and 40% mill load

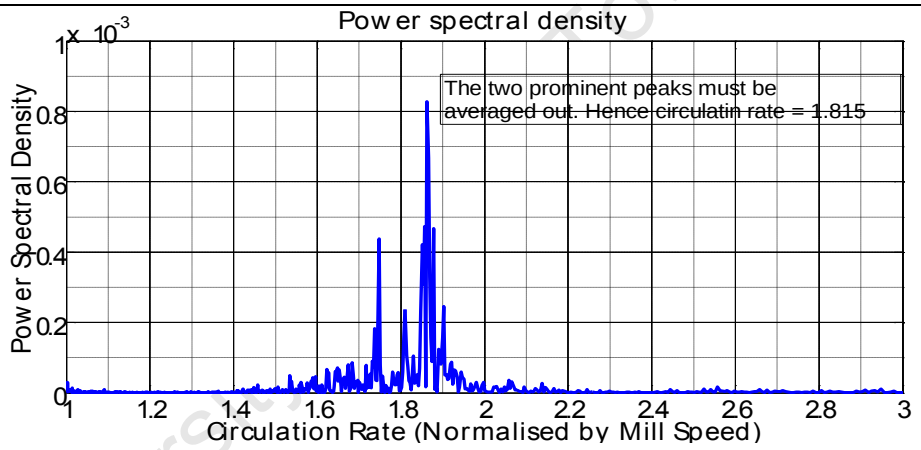

(c) Circulation rate at 50% mill speed and 40% mill load

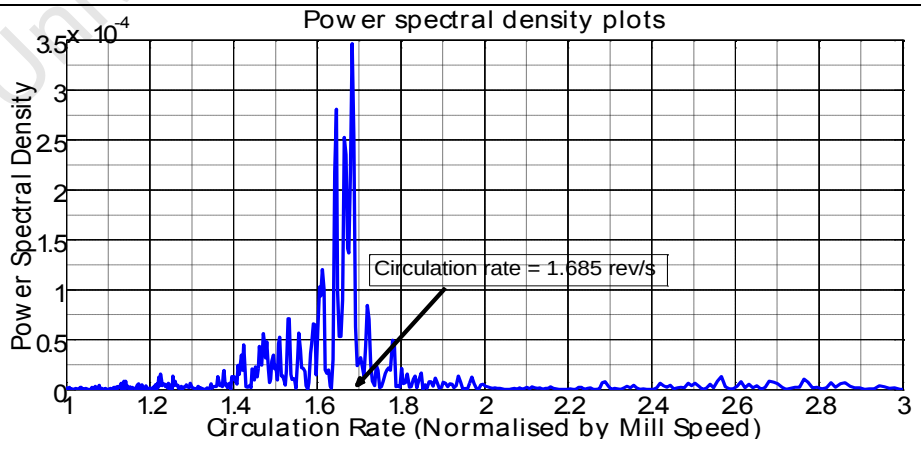

Fig 28: Power spectral plots showing circulation rates obtained from the first peak or an average of closer peaks.

(a) Circulation rate at 65% mill speed and 40% mill load

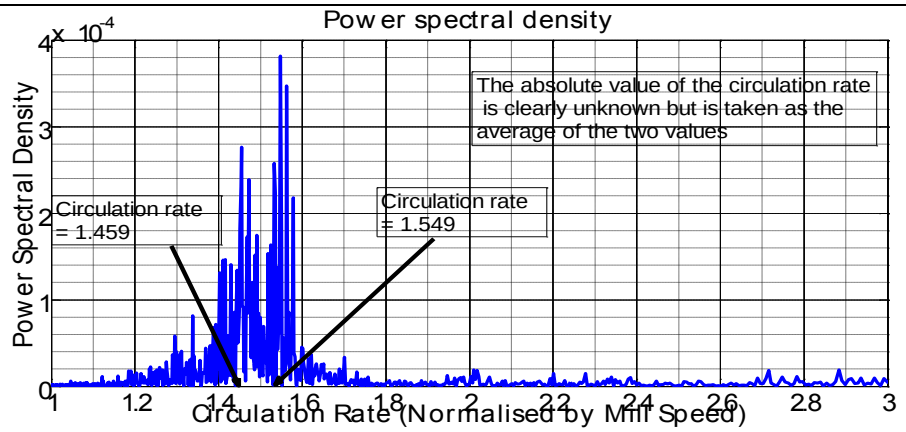

(b) Circulation rate at 75% mill speed and 40% mill load

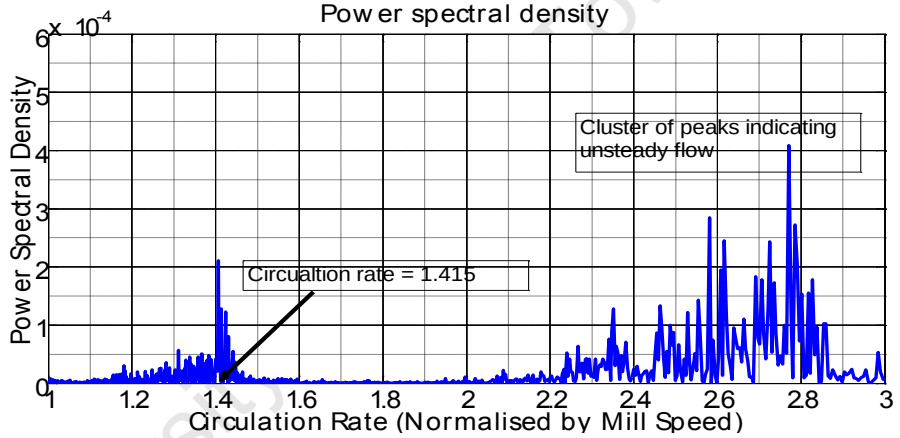

(c) Circulation rate at 90% mill speed and 40% mill load

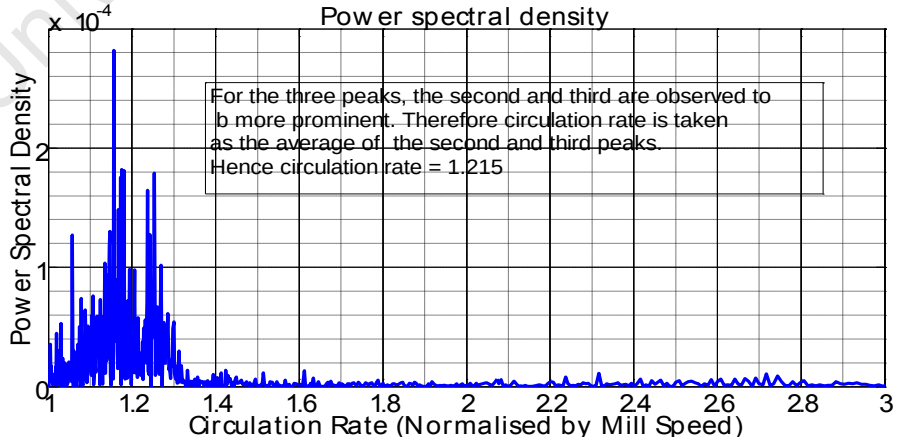

Fig 29: Power spectral plots showing circulation rates obtained from the first peak or an average of closer peaks.

Using the MATLAB FFT function, the DFT of the radial positions $R(\omega_n)$ could be found. The power spectrum at various mill speeds is obtained from equation (32) and plotted in figures (28) and (29). Some important inferences that can be made from these plots are:

- In figure (28a) which shows the mill running at 20% of the mill critical speed (the lowest speed used in the experiments) an initial peak appears at start up. Since the plots are normalized by mill speed this peak represents the fundamental frequency of the mill. The charge and mill are seen to move at the same velocity indicating that this fundamental frequency must be equal to unity ($\omega_0 = 1.0$).

- Once the charge starts to circulate a peak or cluster of peaks appear to the right of this fundamental frequency. This peak is the fundamental harmonic from which the circulation rate of that experimental run can be read.

- There is a gradual shift in the location of the peaks (or cluster of peaks) towards this fundamental frequency as mill speed is increased. This can be explained by the fact that the trajectory path travelled by a particle in one circulation is considerably shorter than the mill circumference at lower speeds but this ratio reduces at higher speeds. Hence at lower speeds the circulation rate of the charge in a tumbling mill is high. At higher speeds, when the charge trajectories are longer, the circulation rate approaches the fundamental frequency of ($\omega_0 = 1.0$).

- These harmonics (circulation rates) are plotted as a function of mill speed in figure (30). An empirical line is fitted to the data with a high coefficient of determination ($R^2 = 0.98326$). From this plot a linear relationship between the fundamental harmonic (circulation rate) and mill speed is

observed where the former decreases near linearly with increasing the later. Figure (30) has a similar trend to figure (26) showing that there is a near linear relationship between circulation rate and mill speed.

- In figure (29b) it can be observed that higher order harmonics may sometimes occur in the spectral plots. These may represent higher order charge circulation rates in the mill and could be as a result of unsteady flows nearer to the end of the experimental run. However there may better more physical interpretations of this occurrence and its consequence for mill performance needs to be further investigated. This however is out of scope of this research.

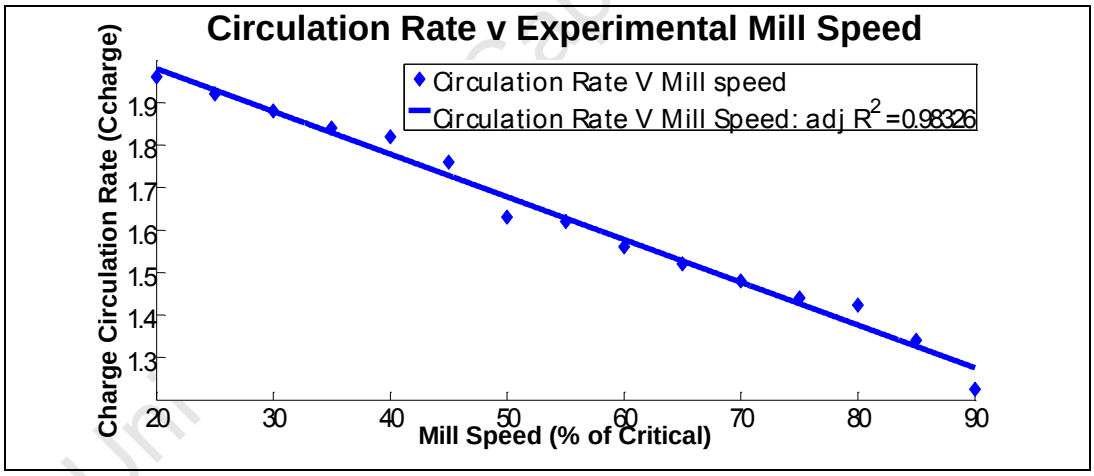

Fig 30: Plot of power spectral peaks (harmonics or circulation rates) as a function of mill speed.

5.1.4 The Equilibrium Surface and the Centre of Circulation (CoC)

The charge in a tumbling mill can be delineated into an ascending and a descending zone [115]. There is, therefore, a frictional surface separating these zones often referred to as the equilibrium surface. According to Barth [105] this "equilibrium surface" is a plane that splits the charge into two distinct regions: an

inner static region that does not appear to move relative to the shell and a shear region where balls either flow down the free surface of the charge (cascading) or follow parabolic paths as they are projected into free-flight (cataracting). Although not entirely true, the observations of Barth denote one of the seminal efforts in delineating the charge body into measurable constituents.

Powell and McBride [56] used the concept of conservation of flow across three control surfaces to identify the CoC and the equilibrium surface. This approach has been employed in the present research and a detailed program was developed for carrying out our calculations, see Appendix C.

The circulation plane of the mill can be divided into families of horizontal, vertical and radial control surfaces. In this way a cumulative count can be obtained of particles passing through any point along a given control surface. This allows for the identification of a point along that control surface at which the flow of particles is deemed to be maximum, termed the "flow equilibrium point." According to Powell and McBride [56] this "flow equilibrium point" identification is similar to the phenomenon of destructive interference in that particles whose motions are regarded as been positive according to some criteria are in equilibrium with those whose motions are regarded as negative with respect to the same condition. Obtaining the flow equilibrium surface in any family of control surfaces is achieved by joining the points corresponding to successive flow equilibrium points within that family. This gives rise to three flow equilibrium surfaces corresponding to the orientation of the families of flow control surfaces in the vertical, horizontal and radial directions. The vertical flow equilibrium surface formed from the vertical control surfaces separates the ascending and descending *en-masse* charge. The horizontal flow equilibrium surface formed from the horizontal control surfaces separates the *en-masse* charge moving in a positive sense in a horizontal direction from that moving in a negative sense.

Powell and McBride [56] observed that the flow along any control surface passing through the Centre of Circulation (CoC) will be a local maximum and independent of the control surface orientation. Hence we identified three distinct Centres of circulation (labelled as CoC1, CoC2 and CoC3 – see appendix C) corresponding to the points of maximum flow cumulative counts along each flow equilibrium surface. The combined (CoC) is the average of the three centres of circulation.

The coding was implemented successfully but with a little limitation. Observations shows that at some speed the charge may form a hollow space between the ascending *en-masse* and descending cascading charge. In such situations the (CoC) location can best be *eye-balled* by the use of the (ginput) function of matlab. This second approach proved more successful but is user-dependent.

5.1.5 Centre of Mass (CoM)

The centre of mass (CoM) of a system has been said to obey the equations of motion and as such can be used as a reference point for other calculations [119]. According to Symon [120], for any system of particles, a fundamental law of mechanics states that the Centre of Mass (CoM) moves like a single particle, who's mass is the total mass of the system, acted on by a force equal to the total external force acting on the system. For a system at rest the centre of mass corresponds with the centroid of the particles [15, 23]. The (CoM) of a distributed system (such as the charge in tumbling mills) is a point that acts as if the entire mass of the system were concentrated there. Using this law as a basis, Powell and Nurick [79] suggested that the (CoM) of the charge in a rotating mill can be defined as that point where, if the entire mass of the charge were to be condensed, would exert the same torque about the centre of the mill. For a distribution of particles the (CoM) can be regarded as a function of the position and masses of

the individual particles and its location can be found by statistical methods as the weighted average. In statistical context the centre of mass of a system of particles would be defined as the average of their positions weighted by their masses [120]. This position was found by using the definition of Powell and Nurick [79] given in equation (27) below.

For a series of particle positions of the tracked ball with mass *m*, the (CoM) is given by [79]:

$$X_{CoM} = \frac{\sum_{j=1}^{q}\sum_{i=1}^{N_j} x_{ij}}{\sum_{j=1}^{q} N_j}, \qquad Y_{CoM} = \frac{\sum_{j=1}^{q}\sum_{i=1}^{N_j} y_{ij}}{\sum_{j=1}^{q} N_j}, \qquad Z_{CoM} = \frac{\sum_{j=1}^{q}\sum_{i=1}^{N_j} z_{ij}}{\sum_{j=1}^{q} N_j} \tag{27}$$

Where N_j is the number of images of the tracked particle in the j^{th} circulation and q is the number of complete circulations made by the tracked particle. In the Euclidean space the more closer the point obtained from equation (27) is to the true centre of mass the more likely it is to belong to our data set. The coordinates (X_{CoM}, Y_{CoM}, Z_{CoM}), therefore, represent the time-averaged centre of mass of the tracer particle distribution.

5.1.6 Angle of Repose (AoR)

The angle of repose of a pile of material is normally evaluated at its critical value. The angle of natural repose is widely used in agricultural processing, where it is commonly determined as the angle between the sides of a cone and its base formed by a pile of granular materials [121]. Such a pile remains stable if the internal friction angle is greater than the natural repose angle [122]. This will

indicate that a point of static equilibrium can be achieved when the coefficient of static friction equals the tangent of the repose angle [23]. This value varies widely between materials - while crushed asphalt has as high an angle of repose of 45^o, wet excavated clay has as low a value as 15^o [123]. The value also varies between conditions – dry sand has an angle of repose of 34^o while the value for wet sand is 45^o [123].

In comminution the angle of repose is commonly employed in describing the torque exerted by the charge, and consequently the power drawn. The concept may have evolved because of the difficulty associated with measuring or calculating the angular position of the centre of gravity of the charge. In the literature Powell and McBride [56] have presented the most user-independent definition for the repose angle by noting that the path of the balls in the *en-masse* region form concentric rings of decreasing radii that converge on the (CoC). Hence they concluded that "the tangent to the equilibrium surface at the (CoC) is perpendicular to the radial line passing through the (CoC). This condition is uniquely defined because the equilibrium surface has a different curvature to the mill shell, so only one point on the surface can have a tangent perpendicular to a radial line."

According to Govender [23] closer inspection of the geometric implications of the Powell and McBride definition [56] reveals that the angle of repose is simply the angular position of the (CoC), see figure (31a).

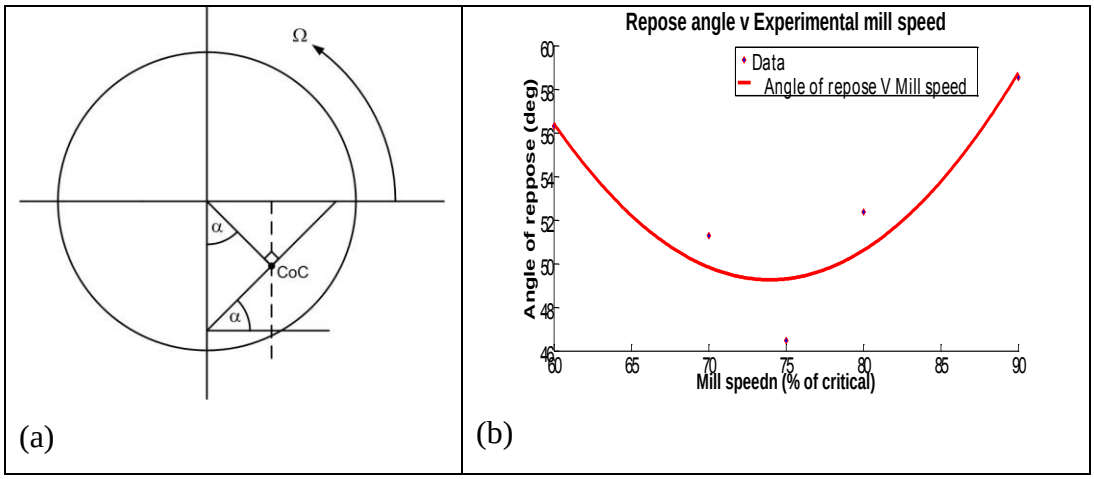

Fig 31: (a) Angular location of the CoC, Govender [23], (b) relationship between mill speed and the repose angle.

This definition has been used in this research and the repose angle was obtained from the coordinates of the combined (CoC) location as shown in table (6). The plot in figure (31b) illustrates the relationship between the angle of repose of the charge (angular location of the charge centre of circulation) and the mill operating speed.

Table 6: The CoC, CoM and the repose angle values for all particle sizes

Mill speed	**Centre of Mass (m)**		**Centre of Circulation (m)**		**Repose angle**
(%) of critical	**x**	**y**	**x**	**y**	**degrees**
90	0.063935	-0.019030	0.081316	-0.050530	58.53324
80	0.068095	-0.030040	0.078409	-0.060720	52.36307
75	0.067579	-0.032030	0.074821	-0.071050	46.47562
70	0.069638	-0.037250	0.073170	-0.058610	51.27762
60	0.086156	0.050950	0.073585	-0.050170	56.31217

5.1.7 Toe and Shoulder (TaS)

The importance of the toe and shoulder in comminution research can hardly be overstated. Some researchers have used their definitions to provide a description of the angle of repose of granular particles in mills as the line joining the toe and shoulder of the charge [66, 67, 124, 125]. Recent work by Powell and McBride [56] has revealed the inherent shortcomings of these eye-balled definitions since they cannot hold true at speeds greater than 80% of the critical. Powell and McBride [56], therefore, proposed the concept of a departure and head shoulder in describing a shoulder region and an impact and bulk toe in describing a toe region, see figure (32).

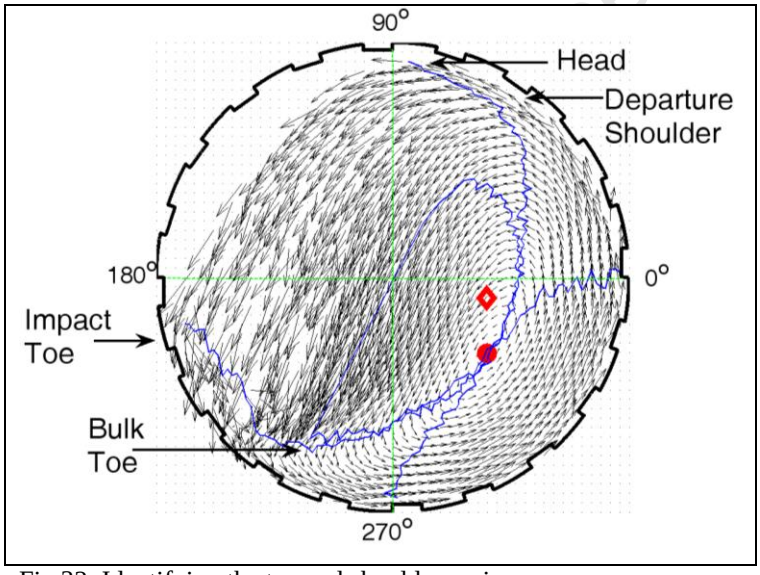

Fig 32: Identifying the toe and shoulder regions.

According to these authors [56], the departure shoulder (DS) is defined as the uppermost point at which the charge departs from the shell of the mill. The charge may still travel along the surface of a lifter bar, and may still be travelling in an upwards direction, prior to entering cascading motion or free flight. The head shoulder (HS) is defined as the apex position reached by the charge, so it is the

highest vertical position that the charge attains. The bulk toe (BT) is located by the point where the horizontal extension of the horizontal equilibrium surface from the inflection point (defined as the point at which the horizontal equilibrium surface moves in an upwards direction towards the impact toe) intersects the shell. The impact toe (IT) is where the cataracting charge impacts the shell in the toe region when the mill speed is sufficiently high. This is given by the point where the horizontal equilibrium surface intersects the shell of the mill in the toe region.

Table 7: The circulation rate, mill speed and the departure shoulder angle.

Mill speed	**Circulation rate**	**Departure shoulder angle**
(%) of critical	**(s^{-1})**	**degrees**
90	1.227383	37.25399
80	1.284023	33.40157
75	1.343833	31,02789
70	1.422219	29.20086
60	1.514961	22.62064

We have implemented these definitions here to manually obtain the coordinates for these four points by using the (ginput) function of matlab. The manual estimates of the departure and head shoulder as well as the impact toe are readily obtained from the picture of the particle trajectory as illustrated in figure (32). However, the bulk toe location is not easily implemented in a numerical sense due to the noisy path followed by the horizontal equilibrium surface. In table (7) we give some values from the estimates of the departure shoulder using the above mentioned method. An empirical line is fitted to the data with a high coefficient of determination (R^2 = 0.96373). Figure (33) shows the relationship between the departure shoulder of the charge and the mill speed at all mill loads.

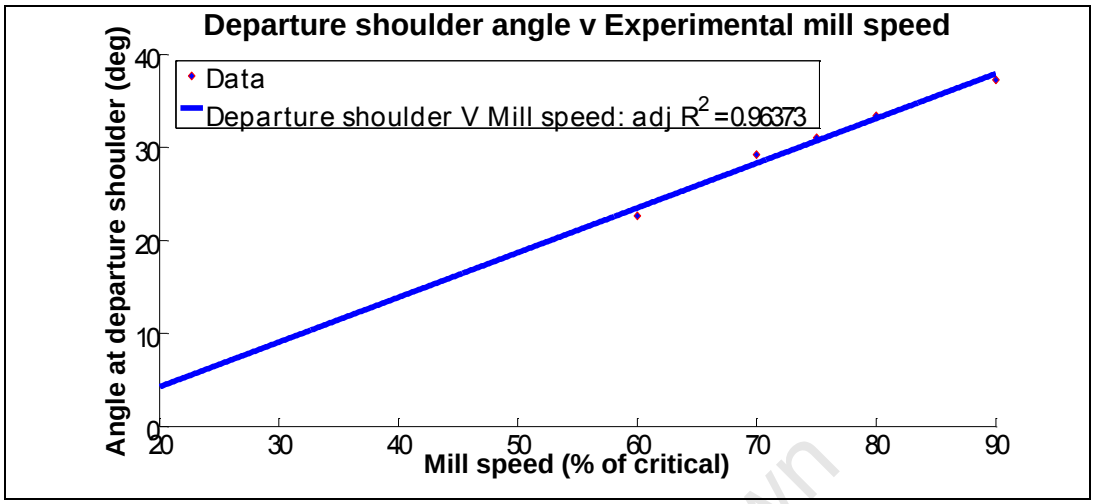

Fig 33: Variation of departure shoulder with mill speed at all mill loads.

With angles measured anti-clockwise from the zero degrees line (positive x-direction) it is easy to see that the departure shoulder angle increases with increasing mill speed. This trend is reversed for the relationship between circulation rates and departure shoulder as indicated in table (7). The graph, figure (33) indicates that provided the mill filling is appropriate, the apex of the charge (defined as the uppermost point reached by charge) may still be in the first quadrant in a geometric sense even for low mill speeds. Hence by way of their connecting relationships with mill operating parameters such as mill speed and mill fractional filling, geometric parameters such as angle of repose, toe and shoulder angles can be shown to vary with the circulation rates of the tumbling charge. In chapter (7) we show that circulation rate of tumbling mill charge can be written as a function of mill operating physical and geometric parameters, as shown in equation (35).

$$C_{charge} \rightarrow C_{charge}\,[N,\ \mu_k,\ \theta_{mean},\ \theta_c,\ \zeta,\ \alpha\ ] \qquad (35)$$

5,2 Conclusion

In this chapter we have established that the rate of circulation of the charge in a tumbling mill can be expressed as a function of measureable mill parameters such as mill rotational speed, load fraction, charge angle of repose, departure shoulder angle and coefficient of friction, depicting near linear trends. While the rate of circulation of the charge was found to decrease with increasing mill speed and departure shoulder angle it showed a non-linear relationship with mill load fraction, indicating the effect of circulation rate on mill liner designs. There is no perfectly keyed-in motion, even for the outermost layer of the charge and all layers of the charge, irrespective of the speed and lifter configurations, were found to slip relative to the mill. Experimental results showed clear cascading motion at moderate speeds (40 - 60%), cataracting at (70 - 75%) and partial centrifuging at higher speeds such as (85 - 90%) of the critical speed. The circulation rate of the charge was found to be a maximum when the (CoC) was correctly located, but there was no observable trend between circulation rate and the (CoM). Accurate determination of the charge geometric location is dependent on the angular location of the CoC – angle of repose - and the charge repose – the line joining the impact toe and departure shoulder. Experimental results show these features can have a linear relationship with the mill operational speed and through that to the tumbling charge circulation rate.

Chapter six: Tumbling Charge Motion

6.0 Introduction

Until the work of Mishra and Rajamani [110] and later Morrell [54], very little was known of the kinematics of industrial tumbling mill charge motion. Morrell [54] noted that many of the previous descriptions make simplifying assumptions about the charge in order to allow for fairly simple mathematical treatments. Hence optimization and modelling through simulation has been preferred to characterization as this allows the investigator to assume a prior knowledge of charge motion characteristics. However, the complex phenomena encountered in mill modelling would require well developed descriptions of charge motion achievable only through a thorough characterization process. Optimization through simulation could then lead to more accurate predictions of charge motion dynamics.

In this chapter we present a review of current understandings of the kinematics of charge motion using PEPT data and focusing our discussion in the 2D plane represented by the charge circulation. The analysis of the PEPT data in chapter five makes it possible to assess circulation rate trends useful in comminution practices. The internal friction between charge and the mill shell was shown to

follow a linear pattern, decreasing with mill speed, giving a corresponding decrease of slip between charge layers.

6.1 Charge Motion in the 2D Plane

The 2D motion of the charge in rotary mills has been reported to range from that of a slipping bed which appears to be stationary [126], to that of a bed that sticks to the shell and rotates with the mill [18]. Between these two extreme states charge rotational motion is categorized into three main forms and seven subtypes as shown in table (8) below. There are transition conditions from one form of motion to the other as well as between subtypes which have all been shown to mostly depend on mill internal friction and mill speed [15].

Table 8: Motion forms and their subdivisions.

Circular charge motion							
Forms	**Slipping**		**Cascading**			**Cataracting**	
Characteristics	Low friction & mill speeds		Sufficient friction & moderate speeds			Sufficiently high friction and very rigorous speeds	
Types	Sliding	Surging	Slumping	Rolling	Cascading	Cataracting	Centrifuging

6.1.1 Slipping Motion

Slipping motion is characterized by low friction and in the absence of lifters the charge will continually slip back to the base of the mill like a rigid body sliding down a smooth inclined plane. Within this range of motion is the case where the charge appears to have a flat stationary bed known as *sliding motion* or a stationary bed under a slight deflection known as *surging motion*. In reality the

charge is lifted for some part along the mill shell before it slips back to the base of the mill in an oscillating motion with very small amplitude [15, 110]. To date there has been no mathematical model to describe this motion form because it does not have any practical industrial significance. However, Rutgers [126] suggested this form of motion can be observed in some production processes even at higher speeds and filling degrees and can only be eliminated through good lifter designs.

6.1.2 Cascading Motion

Cascading motion is described by some form of rotational motion arising from an increased friction. The transition from slipping to cascading has been presented by Mellmann [15]. He suggested the transition criterion is influenced by friction at the mill wall which he showed to be a function of the filling degree, see section (7.1.1). Cascading motion is widely preferred in industrial operations because of improved particle interactions and hence breakage through abrasion and attrition. Three motion types have been identified within this range - slumping, rolling and cascading motions. The transition between these is affected mostly by mill speed [15].

At mill start up, if mill wall friction is correctly set (by the use of lifter bars) a critical point can be reached where the rising charge (in the *en-masse* region) is levelled out by successive avalanches at the surface. This process is known as slumping of the charge surface and gives rise to the motion type known as *slumping motion*. The slumped layers are replaced by more charge and the cycle continues giving rise to particle mixing. This process is important in the understanding of abrasion-attrition breakage and hence in the classification of grinding efficiency of some mills [127]. An assessment of the slumping frequency can lead one to determine the time of charge lift to its maximum position and the slumping time [15]. Mellmann [15] showed that the transition from slumping

motion to rolling motion occurs when the time of lift is less than the slumping time, as illustrated by equations (36) to (38), which are derived using parameters in figure (34).

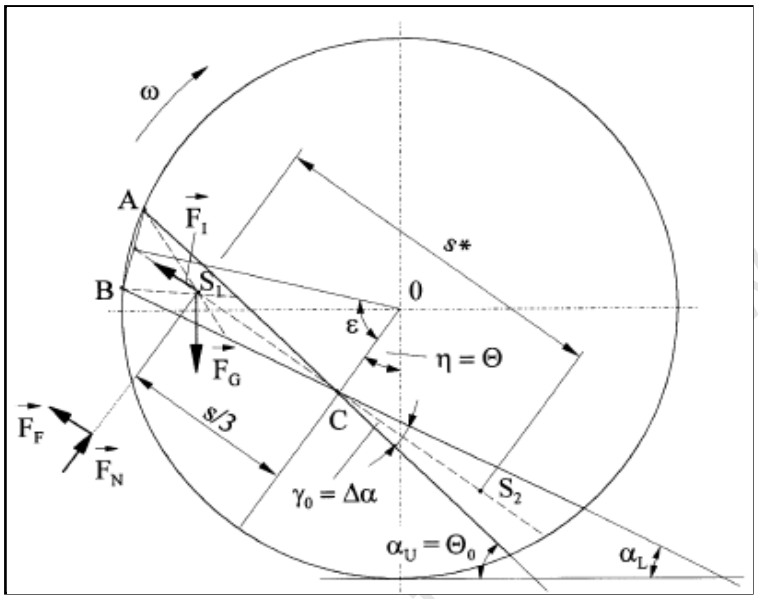

Fig 34: The upper, mean and lower angles of repose during charge slumping - drawn after Mellmann [15].

Time of lift:

$$t_1 = \frac{\pi\gamma_0}{180\omega} \tag{36}$$

Slump time:

$$t_2 = \sqrt{\frac{2s}{g\ \sin\eta - \mu\cos\eta}} \tag{37}$$

Transition criteria given by $t_1 < t_2$

Giving:

$$Fr_c = \frac{3}{2}\left(\frac{\pi(\theta_0 - \theta)}{180}\right)^2 \frac{\sin\theta - \tan(2\theta - \theta_0)\cos\theta}{\sin\varepsilon} \tag{38}$$

Equation (38) gives the critical Froude number which determines the transition from slumping to rolling [15]. This derivation is, however, based on the assumption that the potential energy is converted solely to kinetic energy lowered by energy losses due to friction at the slip plane, see [63].

The significance of Mellmann's findings are that the transition condition outlined in equation (38) is affected by the mill speed and at this stage layers of particles begin to roll down the charge surface. When the first layer of particles rolls down the near flat charge surface the centre of circulation (CoC) assumes its initial location (in a geometric sense) and the charge is essentially circulating [16]. Therefore this transition of the charge motion from slumping to rolling (as illustrated by equation 38) can be regarded as the un-set of charge circulation – that is, it gives the Froude number at which the charge begins to circulate. However, this description remains geometric and how this transition can be determined in a practical sense is still open to debate. From our experiments it was observed that even at 20% mill speed the charge was already rolling, indicating that this transition occurs at speeds lower than 20% of the critical. This

conclusion is supported by the values of Froude numbers in table (9). Mellmann [15], suggested charge slumping appears within the range of Froude number ($10^{-5} < Fr < 10^{-3}$) and from table (9) this will indicate below (10%) of the critical mill speed. Due to the design of the motor used in all PEPT experiments the speed could not be reduced to below 20% critical.

As could be expected *rolling motion* begins at the stage where the first layer of balls roll down the surface of the charge which acts as an inclined plane. Provided mill wall friction is sufficient, as mill speed is increased gradually more and more particle layers continue to roll until the bed begins to form into a kidney shape. The transition to cascading is experimentally difficult to determine and subject to manipulation by the investigator. Henein et al [128], suggested cascading appears when the filling angle exceeds a critical value given by equation (39), see figure (34).

$$\varepsilon = 90° - \theta \tag{39}$$

Mellmann [15], noted that the condition in equation (39) is only possible if the apex of the bed (highest point attained by charge) is in the upper part of the mill (first or second quadrants). However investigations have shown that cascading can also occur at low filling degrees [15, 16, 19]. Mellmann [15] proposed the transition criterion is given by equation (40):

$$Fr\left(\frac{D}{d}\right) \cong 2 \tag{40}$$

Where the mill diameter is represented by (D), (Fr) is the Froude number and (d) is the particle size or median particle size. However, Mellmann [15] revealed the relationship in equation (40) has not been experimentally validated. In particular, the model does not hold if the ratio (D/d) is significantly large. For instance in our experiments at the iThemba labs, the particle size is (d = 0.005m) while the mill diameter is (D = 0.3m) giving a ratio of (D/d = 30). From equation (40), this would give a Froude number of (Fr = 0.03333) and it would appear that cascading sets in at a mill speed of around (18.3%) of the critical. This is clearly against experimental observation, as the charge was observed to be rolling even at (20%) critical mill speed. One reason for this lack of validity is the difficulty in determining the Froude number for the entire charge to a reasonable degree of certainty. With a slurry and particle size distribution, the dimension of the problem becomes manifold. In table (9) below we give the Froude numbers for different mill speeds. Mellmann [15], suggests that cascading appears within the range of Froude number of ($10^{-3} < Fr < 10^{-1}$) while rolling ends at ($Fr < 10^{-2}$). Hence from table (9) the transition from rolling to cascading will occur within the range of mill speed of (30% to 35%) of the critical mill rotational speed.

Table 9: List of Froude numbers at different mill speeds.

Mill speed (% cri)	**Froude number**	**Mill speed (% cri)**	**Froude number**
5	2.500×10^{-3}	55	3.025×10^{-1}
10	1.000×10^{-2}	60	3.600×10^{-1}
15	2.250×10^{-2}	65	4.225×10^{-1}
20	4.000×10^{-2}	70	4.900×10^{-1}
25	6.250×10^{-2}	75	5.625×10^{-1}
30	9.000×10^{-2}	80	6.400×10^{-1}
35	1.225×10^{-1}	85	7.225×10^{-1}
40	1.600×10^{-1}	90	8.100×10^{-1}
45	2.025×10^{-1}	95	9.025×10^{-1}
50	2.500×10^{-1}	100	1.000

Important in the discussion of circulation rates of the charge in a tumbling mill is the behaviour of the centre of circulation (CoC) within the range of cascading motion. According to Powell and Nurick [16], the (CoC) only comes into existence at the un-set of rolling motion giving the (CoC) its initial radial and angular positions. As more layers roll the original charge surface moves outwards and hence the (CoC) will be seen to migrate towards the mill shell. According to these authors [16], the (CoC) will have its maximum radial position at the point where rolling ends and cascading begins. This point is determined by the dimensions of the mill and the particles [15, 128]. At this point then, the (CoC) appears to momentarily stop before returning inwards. In figure (35) plotted for the case of (40%) filling, this turning point was experimental determined to be (35%) of the critical mill speed. This further validates our theoretical conclusion that the transition to cascading occurs close to (35%) mill speed.

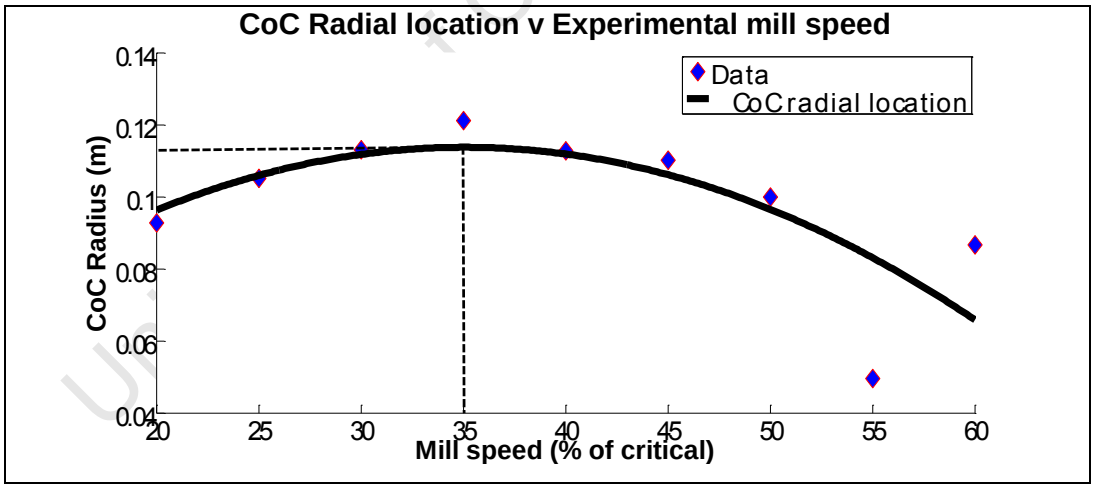

Fig 35: Radial location of the (CoC) at low mill speeds.

Increasing the mill rotational speed from this point (35% critical), as the charge circulates it forms into a kidney shape sometimes called the S-shape. This motion is illustrated as shown by the occupancy plots, figure (37), plotted for the case of (40%) filling,. This stage is known as *cascading motion.* The best description thus far for the occurrence of the S-shape in granular material has been provided by

Taberlet el al [19]. They developed a law linking the inclination of the charge surface (φ) with flow thickness (h) and channel width (L) and showed that the most important factor giving rise to the S-shape observed in cascading is the effect of friction at the end-plates as shown in equation (42).

$$Tan(\varphi) = \mu_i + \mu_\omega \times \frac{h}{L} \tag{42}$$

Where (μ_i) is the coefficient of internal friction (that is friction between charge layers) and (μ_w) is the wall friction coefficient. Deriving an expression for (h), the maximum height attained by the bean-shaped charge, as a function of (x), Taberlet et al [19], showed that the S-shape can be described by equation (43). Where (x) and (y) are Cartesian coordinates.

$$\frac{\partial y_{surf}}{\partial x} = \mu_\iota + \mu_\omega \times \left(\frac{d\omega^2}{g} \right)^{1/4} \frac{1}{L} \sqrt{R^2 - x^2 - y_{surf}^2} \tag{43}$$

From figure (36) it is easily seen that when ($\mu_w = 0$) the charge will have a flat surface as indicated by the black line in the figure. This is a rolling stage of tumbling charge motion. As the influence of the wall friction increases (that is, $\mu_w > 0$) a curvature appears and the charge assumes an S-shape. Qualitatively this scheme could be used to reproduce their experimental and numerical observations.

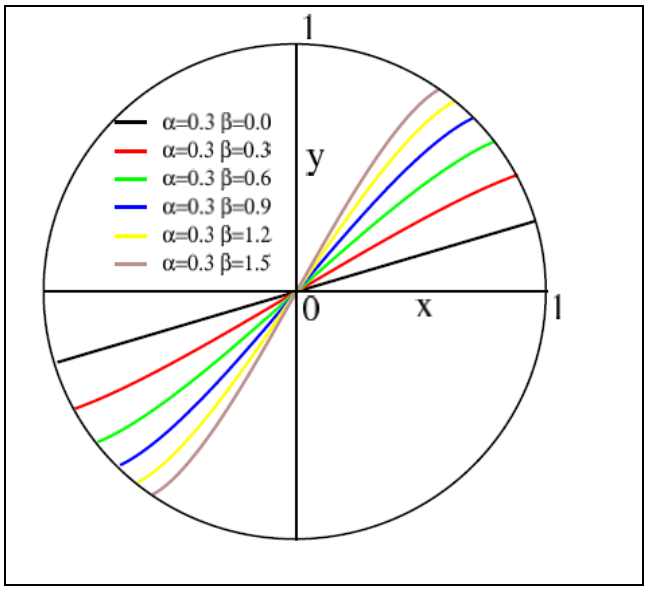

Fig 36: Occurrence of the S-shape in rotary mills, Tabelet et al [19].

The authors noted, however, that equation (43) may not be valid for flows in rotating drums as it was derived for uniform flows. Moreover, when the grains acquire high velocities during the flow they are seen to form upward tails at the end of the slope. Since the inertia of the grains was ignored in the derivations, the model (in equation 43) cannot reproduce this upward flow. Finally from figure (36) it would seem the model is valid only for half drum filling. This leaves more to be done on the S-shape observed during cascading. This was considered out of scope of this research.

It is important to note, however, that according to their range of Froude numbers [15], it would appear that some form of cascading remains prevalent till near the point of centrifuging. That is, when cataracting sets in there would be a combination of cascading and *cataracting motions*.

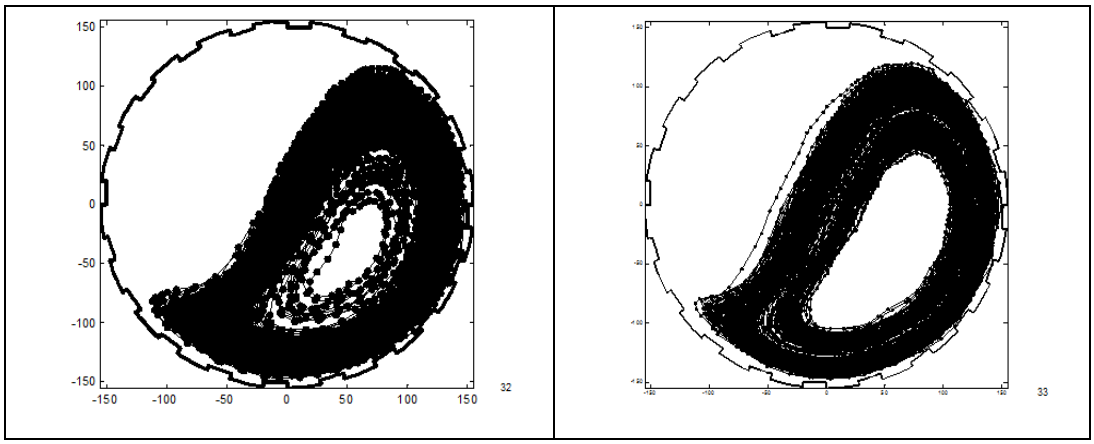

Fig 37: A hollow space forms in the charge while the charge cascades within speed range 40% to 65%.

6.1.3 Cataracting Motion

In this motion range the charge in a tumbling mill are lifted along the mill shell and at some stage they deviate from the mill profile, enter free-flight until they strike the impact point. This motion is illustrated in the occupancy plots, figures (38) and (39), plotted for the case of (40%) filling,. This motion range is characterized by useful impact breakage of larger rocks and compression grinding of finer particles. In section (7.1.2) we have provided a detailed description of the transition from cascading to *cataracting motion*. Motion types in this range are *cataracting* (figure 38) and *centrifuging motions* (figure 39).

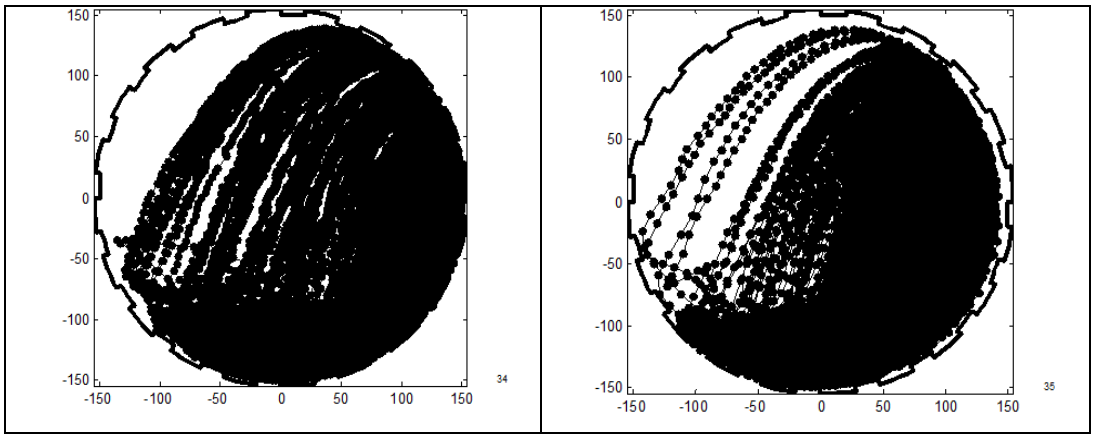

Fig 38: Cataracting motion occurred between speed range 70% to 85%.

Centrifuging occurs when the outermost layer of the charge becomes concentric with the mill shell in rotation. In reality this is only partial centrifuging and complete centrifuging only occurs at extremely high speeds, where the entire charge is seen to form layers that are concentric with the mill shell and rotate together with the shell. The characteristic criterion for transition from cataracting to centrifuging is (F_r = 1). However this is only possible for a single particle moving along the periphery of the mill shell as was originally suggested by White [61]. In practice the charge centrifuges when (F_r > 1) [15, 18]. Figure (39) shows the partially centrifuged charge at (90%) critical mill rotational speed.

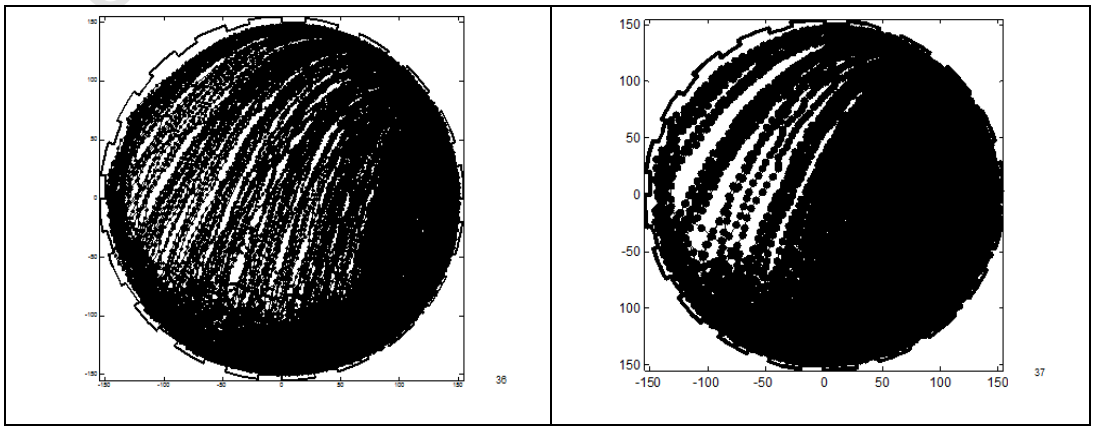

Fig 39: Partial centrifuging seen occurring at around 90% mill speed.

6.2 Summary of Tumbling Charge Motion

In 1984 Mishra and Rajamani [110] adapted the numerical schemes of Cundall and Strack [111] to fit the geometric configuration of a tumbling mill and developed a numerical model using the DEM. This 2D model provided some insight into general charge motion but was still far too simplified to predict the complex movements and forces within industrial mills. Even with the extension to super-quadrics particles by Cleary [55] using a particle size distribution, the 2D models were fundamentally different with regards to particle packing, percolation of smaller particles through the charge and energy distribution when compared to expected results from real mills. Much remains unknown about the particle dynamics deep within the grinding environment of industrial tumbling mill.

The descriptions of particle behaviour provided by many mill models assume the circulation rate of the charge to be unity, implying that the frequency of energy transferred to the charge for potential breakage is once per revolution of the mill. Govender [23] has shown why this needs not be the case. According to him at a speed conducive to cataracting – 75% critical as in figure (38) - particles will be projected into free-fall, following parabolic paths before impacting the mill shell at the toe region. For all experimental speeds used in this thesis this path is observed to be clearly shorter than the path along the shell – inner mill circumference. In addition the tangential speed of the shell is lower than that of the free-falling particles. These differences culminate in the particle circulating faster than the mill and consequently the circulation rate of the charge is greater than unity. Circulation rates of unity can only be achieved when the particles are completely centrifuging. As noted earlier this is an extreme case of charge motion that is not industrially desirable. Therefore, for the range of mill speeds commonly encountered in industrial tumbling mill operations, the circulation rate of the charge is indeed higher than unity.

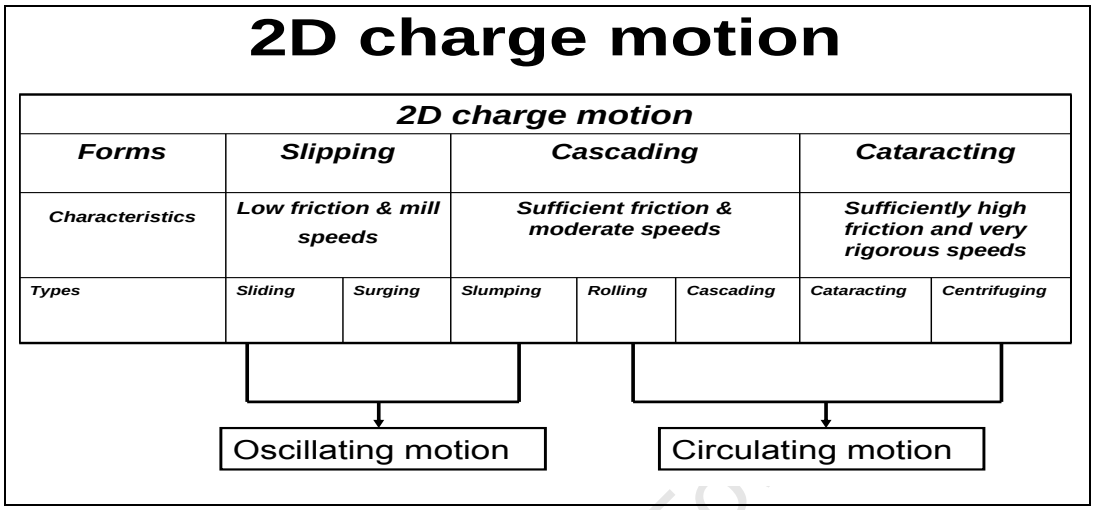

Fig 40: Delineating tumbling charge motion

The common motion ranges can further be delineated into two distinct mechanical motion forms: an *oscillating motion and a circulating motion*. The oscillating motion range is characterized by the charge swinging about a mean deflection taken from the downward vertical. No charge circulation occurs in this motion range and as such the (CoC) is not present. Motion types that fall in this range are sliding, surging and slumping and for its acronym form we have named this range of motion (O-S^3). The circulating motion range is characterized by charge circulating about its own distinct centre (CoC) which has a different location from the mill centre and also migrates depending on the mill speed. The motion types are rolling, cascading, cataracting and centrifuging and we have termed this motion range (C-RC^3).

Chapter seven: Modelling the Circulation Rate of Tumbling Mill Charge

7.0 Introduction

The circulation rate of the charge in a tumbling mill can be regarded as the speed of circulation of the charge about the centre of circulation (CoC). It is the number of complete revolutions made by the charge about the CoC per unit of time. Previous authors have noted that the circulation rate of tumbling mill charge depends on two important factors; mill speed and the mill internal friction (both at the mill wall and slip within the charge) [15 – 19, 23, 24, 128 - 131]. A gradual increase in the wall friction coefficient is known to cause charge motion to change from slipping to cascading [15] and at extremely high speeds, motion eventually changes to cataracting [15, 18, 126, 129]. These two physical parameters of tumbling mill operation, it may be argued, are fundamental to charge circulating motion and any work on modelling the circulation rate of the charge in a tumbling mill must provide mathematical descriptions of the effect of these two parameters. However, in order to fully understand their influence on charge behaviour one needs to examine the boundaries conditions that enable a change between the known common ranges: slipping, cascading and cataracting.

7.1 Transition Zones Revisited

In the previous chapter we described tumbling charge motion and the transitions within the known ranges of slipping, cascading, and cataracting. Mellmann [15], derived the transition conditions not only within these main forms but also between the ranges of motion. In this chapter we revisit these derivations and formulate new descriptions. We have been able to develop these new descriptions by approaching the problem from an *in-situ* perspective using the PEPT technique.

Generally slipping motion (sliding and surging) can occur at both low and high speeds if friction at the mill wall is low (no lifters). Increasing mill friction coefficient such that the charge can move at the speed of the mill, motion changes to cascading (or tumbling) and the range of slumping, rolling and cascading motion occurs. With sufficient friction and at relatively high speeds cataracting motion sets in. Centrifuging is an extreme case of cataracting when the outermost balls of the charge form a concentric ring with the mill shell [15, 18, 126, 129].

7.1.1 Slipping to Cascading Transition

Studies on charge motion date back to the work of White [61] and cover a wide variety of topics. However, only a few authors [15, 18 and 129], among others, have attempted any investigation of the transition criteria for motion changing between these forms and within the range of each form of motion. In 2000, Mellmann [15], published a detailed investigation of charge motion transition behaviour from slipping to cascading and showed that this depends on the mill critical wall friction coefficient as illustrated by equation (44).

$$\mu_w > \frac{2\sin^3 \varepsilon \sin \delta}{3\ 1+F_r \quad \varepsilon - \sin \varepsilon \cos \varepsilon} \tag{44}$$

Where (δ) is the angle of repose of bed surface, (F_r) is the Froude number, (ε) is the filling angle, (μ_w = tan φ_w) characterizes the effective frictional coefficient of the bed material to wall over the entire solid covered wall. These parameters are shown in figure (41) below.

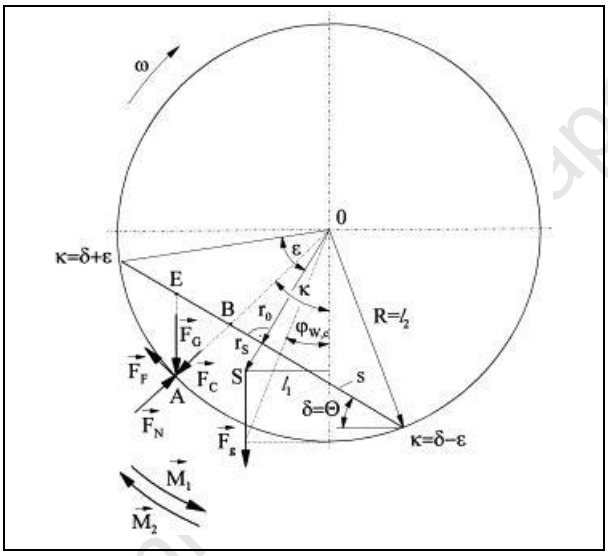

Fig 41. Illustration of the mill geometry at low speeds by Mellmann [15]

Hence from slipping to cascading the transition behaviour is determined by the wall friction coefficient (μ_w), filling angle (ε) and the Froude number (F_r). With the onset of cascading motion a dynamic angle of repose (θ) which determines the new position of the centre of gravity of the charge is brought into play giving a critical wall friction coefficient shown in equation (45), where (f) is the filing degree.

$$\mu_{w_c} = \frac{2\sin^3 \varepsilon \sin\theta}{3\pi f \ \ 1+F_r} \tag{45}$$

Suffice it to say here that equations (44) and (45) as derived by Mellmann are based on an over simplified charge shape and a uniform packing of the particles such that the centre of mass of the assembly coincides with the centre of gravity of the system. However, Symon [120] showed that the centre of mass of a system of particles cannot always be the same as the centre of gravity. Thus equations (44) and (45) are only valid for low speeds. For a mill with a size distribution of particles moving at higher speeds we present a new derivation here. Our derivation, which follows closely that of Mellmann's, shows that the centre of mass need not be the same as the centre of gravity of the system under study.

For moment balance around the axis of rotation, let (M_1) be the moment due to the gravitational pull (F_g) on the charge acting through the centre of mass (CoM) and (M_2) the moment due to the frictional forces acting at the mill wall.

Then from figure (41), for (M_1)

- determine the centre of mass from equation (27),
- calculate (F_g),
- multiply (F_g) by (l_1): the perpendicular length from mill centre (O) expressed in terms of (r_i) and (θ_i) the polar coordinates of the centre of mass (CoM).

That is,

$$l_1 = r_i \sin\theta_i \tag{46}$$

Thus

$$M_1 = mgr_i \sin\theta_i \tag{47}$$

Similarly for moment caused by the inner wall friction (M_2), let (κ_m) be the mean charge deflection, ($l_2 = R$), ($F_G = mg$), ($F_c = m\omega^2 R$) and (v) is the mill tangential velocity. Then again from figure (41):

- determine the mean charge deflection (κ_m) of the charge from its original resting position which coincides with the 270^o line pointing south,
- calculate (F_F) the mean frictional force acting through the point of mean deflection (κ_m) of the charge along the mill wall,
- multiply (F_F) by (l_2) the perpendicular length from mill centre (O), which is equal to the radius of the mill in this case.

Then normal force at mill wall:

$$F_N = F_G \cos\kappa_m + F_c \tag{48}$$

Becomes;

$$F_N = mg\cos k_m + m\omega^2 R \tag{49}$$

Equation (49) gives the normal reaction for a particle at a mean deflection of (κ_m). We approach the derivation using two conditions, each of which approach gives a characteristic criterion for motion transition from slipping to cascading. In the first case we consider the total force of the charge to be concentrated at its mean charge deflection (κ_m). This approach gives the average friction model. In the second case we find the friction over the entire particle covered surface to obtain the total friction model.

A. Average Friction Model

Let the normal reaction (F_N) act through the point of mean charge deflection (κ_m). Then from the diagram in figure (41) we see that:

$$F_F = \mu_w F_N \tag{50}$$

From which we can obtain:

$$F_F = \mu_w (mg\cos k_m + m\omega^2 R) \tag{51}$$

The moment at the mill wall is then given by equation (52).

$$M_2 = \mu_w m(Rg\cos k_m + v^2) \tag{52}$$

The transition to cascading occurs when the moment at the mill wall caused by friction exceeds the moment due to gravity [15].

$$M_2 > M_1 \tag{53}$$

This leads to a limiting average coefficient of friction as in condition (54).

$$\mu_w > \frac{gr_i \sin\theta_i}{(Rg\cos\kappa_m + v^2)} \tag{54}$$

The limiting average friction model in condition (54) determines the transition from slipping motion to cascading and depends on the polar coordinates of the centre of mass, the mean charge deflection from its original resting position and the tangential velocity of the mill. Equation (54) is the required coefficient of friction for the transition from slipping to cascading. These parameters are easily determined from PEPT experiments, making it possible to validate the model. Equation (54) shows that the transition to cascading can be independent of the mass of the assembly and the ranges of Froude number, and hence independent of bed material used. The relationship between wall friction coefficient and mill speed is shown in figure (42).

This validation graph shows the rapidly declining effect of friction on the circulating particles as mill speed is increased gradually from rest, becoming zero at approximately 101% of the critical mill rotational speed. It is suggested

here that beyond this point the charge is centrifuged entirely under the effect of centrifugal forces.

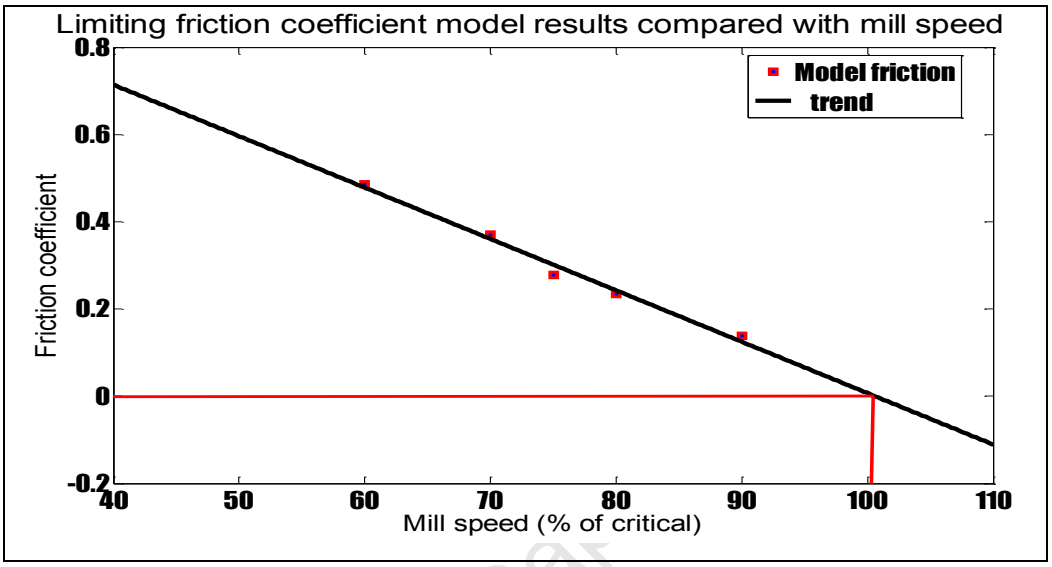

Fig 42: Relationship of wall friction coefficient with experimental mill speed

Let us examine boundary conditions for this model (equation 54). The mean charge deflection angle (κ_m) is determined as half the charge repose - where the charge repose is the angle formed, at the mill centre, by the line joining the departure shoulder and the impact toe. Applying trigonometric conventions the angle (κ_m) coincides with the 270^o line at only two instances of charge motion: once at mill start up and again when the entire charge centrifuges. In such a case ($cos\ \kappa_m = 0$). Furthermore assuming a uniform distribution of particles at start up, the angular location of the centre of mass (CoM) will also coincide with the line 270^o giving (sin θ_i = -1). Hence, we propose here that the maximum attainable friction occurs at start up and is given by equation (55).

$$\mu_{w(\max)} = \frac{-gr_{CoM(i)}}{v^2} = -\frac{g}{a_{CoM(i)}} \qquad (55)$$

The initial tangential acceleration of the centre of mass ($a_{com(i)}$) would be the same as the mill acceleration for the charge and mill, at start up, to move together as one rigid body – important to industrial applications. The negative sign in equation (55) is well supported by the graph in figure (42).

B. Total Friction Model

From figure (41) consider the friction at the deflection (κ) from the vertical. By definition this friction is given as:

$$f_F = \mu_w F_N \ , \quad f_F = \frac{F_F}{A} \tag{56}$$

And from equation (49) we can write:

$$f_F = \mu_w \ mg\cos\kappa + m\omega^2 R \tag{57}$$

The friction along the particle covered surface is then obtained as in equations (58) and (59).

$$dF_F = f_F A = f_F R d\kappa \tag{58}$$

$$dF_F = m\mu_w \left[Rg\cos\kappa + v^2 \right] d\kappa \tag{59}$$

Equation (59) can be integrated between the toe angle (T = δ - ε) and shoulder angle (S = δ + ε), see figure (41).

$$dF_F = m\mu_w \int_T^S (Rg\cos\kappa + v^2) d\kappa \tag{60}$$

$$F_F = \left[m\mu_w \left[Rg\sin\kappa + \kappa v^2 \right] \right]_T^S \tag{61}$$

$$F_F = m\mu_w \left[Rg \left[\sin S - \sin T \right] + v^2 \left[S - T \right] \right] \tag{62}$$

The result of integration, equation (62), is a frictional force model that is a function of the mill tangential velocity, the angle at the departure shoulder and the angle at the impact toe region. When this force is multiplied by the mill radius one obtains the moment caused by friction through the mill axis of rotation.

$$M_2 = F_F \times R \tag{63}$$

$$M_2 = mR^2\mu_w \left[g \left[\sin S - \sin T \right] + a \left[S - T \right] \right] \tag{64}$$

One interesting outcome of this model is that it can also be written in inertial terms as in equation (65).

$$M_2 = I\mu_w\left[\, g\ \sin S - \sin T\ + a\ \ S - T\ \right] \tag{65}$$

Equation (65) indicates that the charge in the *plug-flow* region (rising *en-masse*) is in fact an inertial-dominated driven flow. Recalling the condition: $M_2 > M_1$, where (M_1) is given in equation (47) yields the total friction model in equation (66).

$$\mu_{w_{Total}} > \frac{g r_i \sin\theta_i}{R^2\left[\, g\ \sin S - \sin T\ + a\ \ S - T\ \right]} \tag{66}$$

Equation (66) shows that the total friction over the particle covered mill surface can be written as a function of the mill tangential acceleration (a), the angle at the departure shoulder (S) and the angle at the impact toe region (T). This model is similar to the average friction model in equation (54), the main difference being the replacement of the mean charge deflection by the shoulder and toe angles. The total friction model shows that the charge is accelerated between the toe and shoulder thereby limiting the occurrence of slip between the charge and the mill wall. Both models provide the limiting coefficient of static friction along the particle covered mill wall and are the required friction coefficient for motion transition from slipping to cascading.

7.1.2 Cascading to Cataracting Transition

Cataracting motion which is prominently encountered in industrial tumbling mill operations is characterized by particle throw-off at the departure shoulder and the particle trajectories follow parabolic paths that end at the toe region. The classic theory of throw off states that for the charge to arrive at the upper part of the mill will require the vertical component of the mill acceleration to offset the effect of gravity acting on the particles [15]. Employing this theory Mellmann [15], derived an expression for the transition from cascading to cataracting motion in terms of the Froude number which he found to be a function of the angle at the departure shoulder, equation (67).

$$F_r = \frac{\omega^2 r}{g} > \sin\zeta \tag{67}$$

Where (ω) is the angular velocity, (g) the acceleration due to gravity, (r) is the orbital radius and (ζ) is the departure shoulder angle. These parameters are illustrated in figure (43).

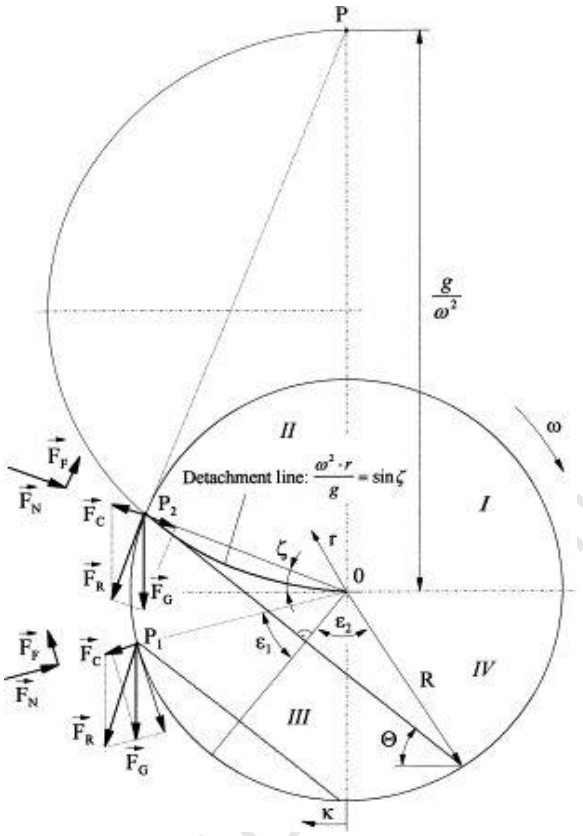

Fig 43: Illustration of the mill geometry at high speeds showing the Davis circle - Mellmann [15].

Equation (67) yields a logarithmic line (OP_2) which is part of a circle of radius ($g/2\omega^2$). This circle is known as the Davis circle [62], shown super-imposed on the mill centre, see figure (43). The circle meets the mill profile at point (P_2) which marks the point of projection of particles into cataracting. Mellmann [15], showed that this point subtends an angle (ζ) at the mill centre and thus developed the transition criteria to cataracting as in equation (67). This criteria remains to be validated as no convincing scheme has yet been developed to determine the departure shoulder angle with reasonable degree of certainty. The departure shoulder estimates remains at best subject to the manipulation by different authors. Moreover, Mellmann [15], suggests pronounced cascading motion may arise from increasing the mill speed which can

eventually cause particles to be projected into free-flight. However, he failed to provide a transition criterion based on the mill speed at the point of departure. Furthermore, based on equation (67) one may obtain two solutions within the range of zero and two pi (2π). Finally, equation (67) requires the mill to be moving upwards such that angle (ζ) is positive. These observations necessitated a new approach.

Let us consider the mill critical rotation speed model proposed by Watanabe [18], see equation (68). The significance of this model is in its inclusion of the charge load fraction (α) and the critical angle of repose (θ_c), making it a clear improvement on the ideas of Rose and Sullivan [17].

$$N_c = \frac{1}{2\pi}\sqrt{\frac{g}{R\sin\theta_c\sqrt{1-\alpha}}} \tag{68}$$

The left hand side of equation (67) is the Froude number (F_r), which is a scaling that delineates the charge into distinct flow regimes. This scaling can also be written as a ratio of the mill rotational speed (N_m) to that of the critical rotational speed (N_c), [15].

$$F_r = \left(\frac{N_m}{N_c}\right)^2 \tag{69}$$

Since the line of detachment in figure (43) is given by Mellmann's model in equation (67), it is easily seen that a combination of equations (67), (68) and (69) would yield a mill speed which is a function of the angle at the departure

shoulder, equation (70). This model determines the characteristic criterion for transition from the range of cascading motion to that of cataracting motion.

$$N_m = \frac{1}{2\pi}\sqrt{\frac{g\sin\zeta}{R\sin\theta_c\sqrt{1-\alpha}}} \tag{70}$$

It must be mentioned here that equation (70) would appear invalid in the lower portion of a typical tumbling mill (third and fourth quadrants) when the angle at the departure shoulder is negative. However, following from the classic throw-off theory Mellmann [15], noted that although at low filling degree and high speeds cataracting can also be observed in the lower portion of the mill, in practice particles can only be projected into free-flight in the upper portion of the mill (first and second quadrants). The model (equation 70), therefore, illustrates the importance of fixing the charge filling degree such that particle throw-off can be achieved. The characteristic criterion for charge motion transition from the range of cascading to that of cataracting can be deduced from equation (70) as in condition (71).

$$N_m > \frac{1}{2\pi}\sqrt{\frac{g\sin\zeta}{R\sin\theta_c\sqrt{1-\alpha}}} \tag{71}$$

The graph in figure (44), plotted from equation (70), shows a close comparison between PEPT experimental speeds and the model mill speed as evaluated from equation (70).

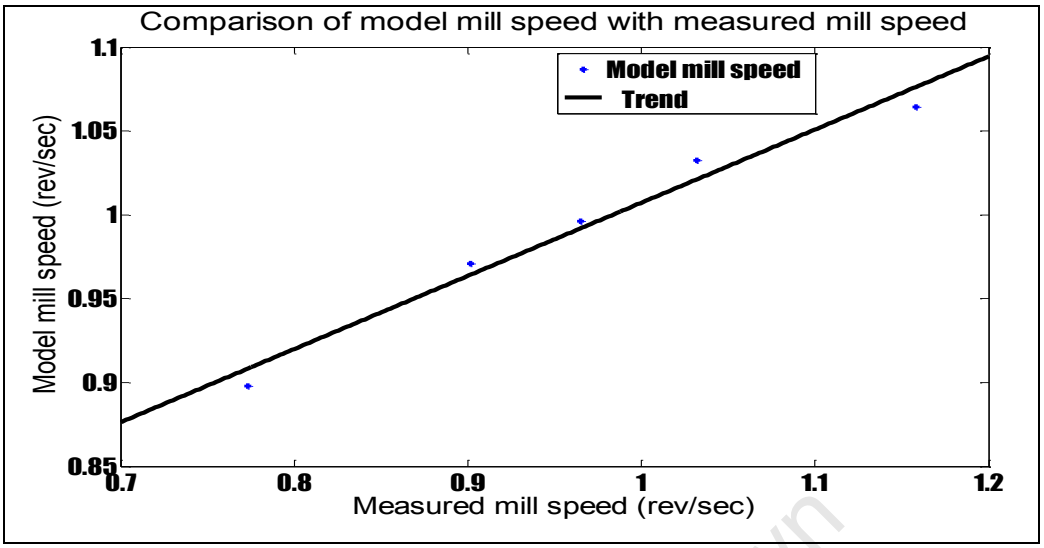

Fig 44: Comparing model and PEPT experimental mill speeds

According to Powell and Nurick [16], the critical angle of repose for mills occurs at the point of total centrifuging and must, therefore, be equal to (90^o). The (CoC) coincides with the mill centre at this stage. The numerator under the root sign in equation (70) corresponds to the mill centripetal acceleration acting along the line of detachment, see figure (43). Hence **(***gsin* $\zeta = g$) at only one point along the mill profile: when ($\zeta = 90^o$). As a point of comparison, equation (68) as derived by Watanabe [18], for mill critical rotation speed is a special case occurring only at the point of total centrifuging, while the new model in equation (70), as derived in this thesis is a more generally case of the mill speed for a mill running below critical speed. Industrial tumbling mills are mostly operated at sub-critical speeds. Equation (70) also relates the Froude number to the shape of the charge (critical repose angle and departure shoulder angle) in the aggressive environment of industrial tumbling mills, Hence the transition to cataracting can now be mapped to more physical geometric interpretation.

7.2 Two-Cycle Description of Tumbling Charge Motion

According to Taberlet et al [19], two distinct regimes can occur in granular flows in rotating drums and both depend on the angular velocities in the grinding region. At low rotational speeds the free charge surface is flat and inclined at a small angle of deflection. A significant curvature appears at higher rotational speeds forming tails that have a major significance for inertial driven flows. We propose that these two distinct flow regimes can be described by two cycles: an oscillating cycle ($O - S^3$) and a circulating cycle ($C - RC^3$) as described in section (6.2).

7.2.1 The Oscillating Cycle ($O - S^3$)

The oscillating cycle is characterized by swinging of the charge about a mean deflection. No charge circulation occurs at this stage as the (CoC) is non-existent. Common motion ranges are sliding, surging and slumping. The predominant modelling parameter of the $O\text{-}S^3$ cycle is the friction at the mill wall. This friction has been shown to alternate between static or kinetic [23]. Another important parameter is the angle of repose of the charge which has been shown to fluctuate between an upper and a lower value [15, 23]. These conditions are shown in figure (45). Interestingly, approaching the work from two different points of view both Mellmann [15] and Govender [23] derived the same model that describes the downward acceleration when the charge slumps from the upper to the lower angle of repose, see equation (72).

$$a(t) = \frac{d^2x}{dt^2} = g \ \sin \ \theta(t) \ - \mu_k \cos \ \theta(t) \tag{72}$$

Here the downward charge acceleration (a) is a function of the angle of repose (θ) and the coefficient of kinetic friction (μ_k). Govender [23] further suggested this acceleration goes through its zero point at the mean angle of repose (θ_{mean}) which he related to the coefficient of kinetic friction, equation (73).

$$\mu_\kappa = \tan\Theta_{mean} \tag{73}$$

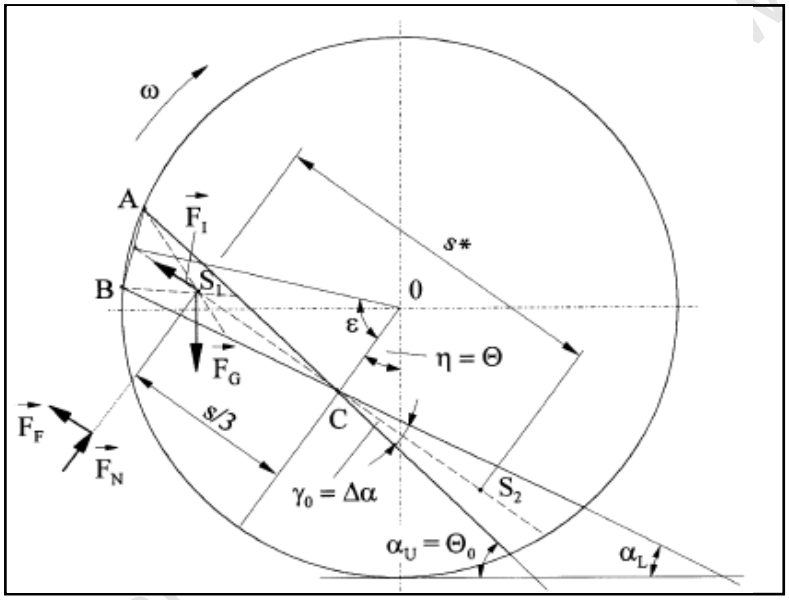

Fig 45: The upper, mean and lower angles of repose during charge slumping by Mellmann [15]

Provided the mean angle of repose is known equation (73) establishes the limiting coefficient of kinetic friction of the charge. It is important to note that there exist a direct relationship between equations (54), (66) and (73). Since the former two describe the limiting coefficient of static friction within the same range of charge motion (that is, O – S^3), then they must be equal in magnitude to the later, [23]. The three friction models also play a major role in

limiting slippage within the charge that is sometimes observable within this range of motion. The basic idea of charge slipping is that the angular velocity of a rigid body must remain constant at all radial positions with deviations from this phenomenon indicating slip within the charge [54, 106]. By studying the circulation rate of particles with their radial positions Morrell [54], established this degree of slip as a function of radial position. Using an experimental procedure Govender [23] obtained a plot of the variation of the degree of slip with mill speed (*N*) shown in figure (46).

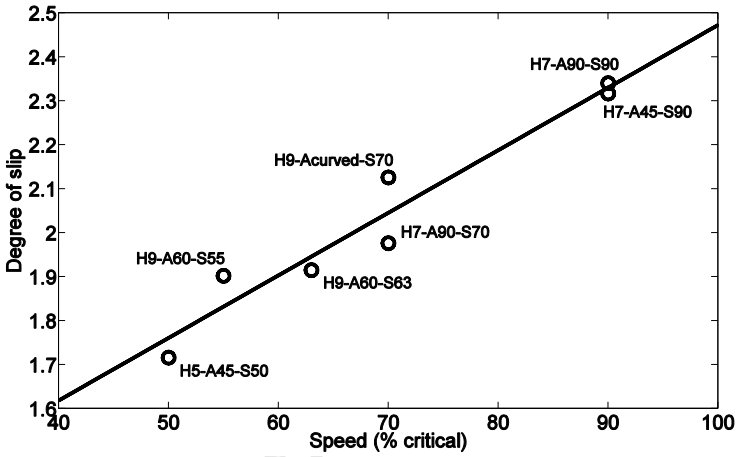

Fig 46. Variation of angular velocity gradient across charge layers with mill speed by Govender [23]

This plot shows a distinctly linear relationship between degree of slip (*D*) and mill speed (*N*) with their connecting relationship shown in equation (74).

$$D = 0..14N + 1 \tag{74}$$

Due to the lack of further verification of this model the relationship between the degree of slip and mill speed is still unclear. However, Vermeulen and

Howat [65], showed that the angular velocity of the concentric layers of the tumbling charge decreases as the (CoC) is approached, becoming zero at the (CoC) itself. In the oscillating cycle, since the (CoC) does not exist, this would mean the point along the charge surface where a radial line bisects the chord formed by this surface. From figure (45) it can be observed that this is at (C) where the charge surface appears to be in a state of resting position as compared to the surrounding oscillating charge. For all other points slip will occur between particle layers unless the degree of slip along the chosen surface (between two particle layers) is equal and opposite to the coefficient of kinetic friction. Hence for such a mill the relationship in equation (75) holds true. Again the negative sign in the model is well supported by the graph in figure (42).

$$\mu_{\kappa} = -\tan\theta_{mean} \tag{75}$$

Equation (75) gives a complete picture of (O – S^3) range of tumbling charge motion.

7.2.2 The Circulating Cycle (C – RC^3)

The circulating cycle is a motion range that is characterized by particles circulating about the (CoC). Common ranges include rolling, cascading, cataracting and centrifuging motions. Any discussion of circulating motion in rotary mills must necessarily begin with an understanding of two important grinding regions; that of the toe and shoulder. The definitions of these regions vary from researcher to researcher and until recently were qualitatively employed to define the angle of repose – as the line joining the toe and shoulder of the charge. Powell and McBride [24], noted these definitions

become meaningless if the speed is increased beyond (80 %) of the critical, indicating that such definitions hold only at low mill speeds. In practice the line joining the toe and shoulder can better be referred to as the *charge repose*. The *mean charge deflection* (κ_m) is half the charge repose.

Using DEM to numerically validate empirical models, Cleary et al [55] and more recently Powell and McBride [24], provided improved definitions of the toe and shoulder regions of the mill. These definitions, which use trajectory data from an experimental run depicting clear cascading and cataracting, are illustrated in figure (47).

Powell & Nurick [16], suggested that although the toe and shoulder concepts are useful in characterizing the charge in the mill, poor definitions prevent an objective charge description. Accordingly Powell and McBride [24], proposed that the shoulder region can be defined using the concepts of a head and a departure shoulder of the charge, figure (47). The toe region on the other hand can be described using the bulk and impact toe. When the charge circulates its trajectory follows two paths, one in ascending and the other in descending with the start and end points of both paths at the toe and shoulder regions respectively. The trajectory of a circulating particle can only be calculated if three parameters are known: the locations of the centre of circulation (CoC), departure shoulder and impact toe. These parameters have been shown to vary with the operating mill speed. Hence the (C – RC^3) motion range is well described by the mill speed model reproduced below, see equation (76)

$$N_m = \frac{1}{2\pi}\sqrt{\frac{g\sin\zeta}{R\sin\theta_c\sqrt{1-\alpha}}} \tag{76}$$

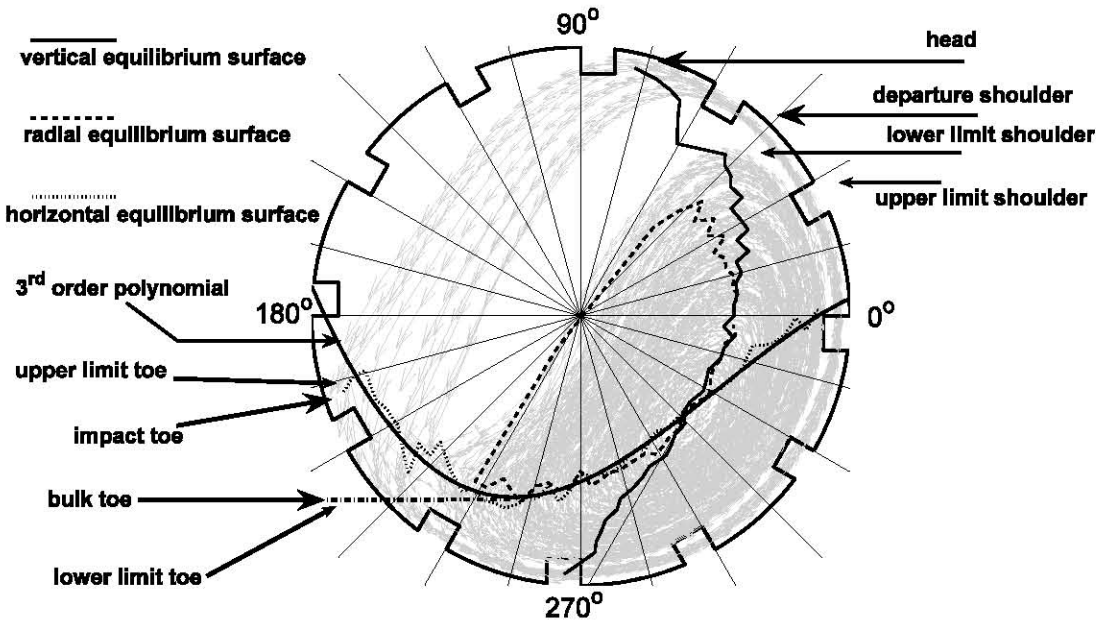

Fig 47. Shoulder and toe estimates according to Powell & McBride [24] and Cleary et al [113] for the H7-W9-A90-S70 (lifter) configuration. Small arrows: Cleary et al; Large arrows: Powell & McBride

7.3 A Circulation Rate Model

A great deal of effort has been directed to studies on breakage probability applied to tumbling mills. Austin and Cho [132] developed an algorithm for computing a size-based mass energy balance arising from impact breakage of particles at various specific strain energies. Many more, such as Schonert [28], have detailed the development of models that attempt an explanation of the complex phenomenon of particle breakage. Most of these models are based on simplifying assumptions made about the rate of energy transfer to the charge body. On the premise that the critical Froude number, occurring at the point of centrifuging, is unity, it is commonly assumed that the rate of energy transfer to the grinding environment is equal to unity irrespective of the speed at which the mill is run. Mellmann [15], argues that such assumptions inevitably lead to overlooking the effect of tangential equilibrium arising from

friction at the mill wall. In chapters four and five we have shown that the charge circulation rate is not constant with respect to mill operating variables such as mill speed and volume containing fraction. This is well supported by the findings of Govender and Powell [6].

Recent X-ray particle tracking experiments conducted by Govender and Powell [6] within a simplified laboratory tumbling mill showed that the circulation rate of the charge can have a near linear relationship with speeds typical of tumbling mill operations. In current literature the circulation rate of a particle is defined as the average number of circulations per revolution of the mill. A plot obtained by Govender and Powell [6] on this definition, see figure (48a), showed a near linear trend with a circulation rate of approximately 1.7 at (50%) of the critical mill speed.

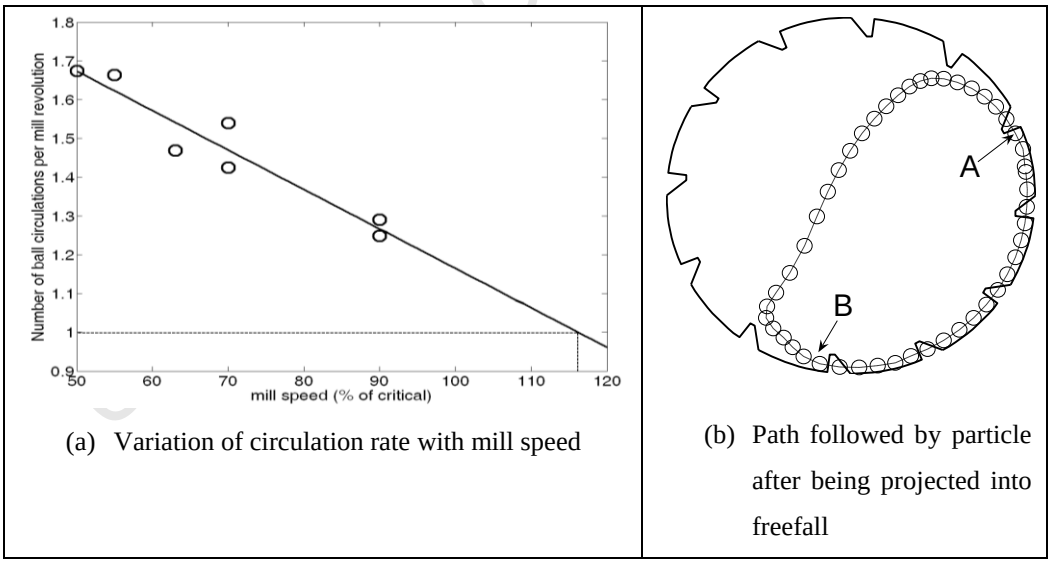

(a) Variation of circulation rate with mill speed

(b) Path followed by particle after being projected into freefall

Fig 48: Circulation rate of tumbling mill charge from X-ray particle tracking experiment by Govender and Powell [6]

The circulation rate dropped near linearly from this initial value to a value of 1.0 at an extrapolated speed of (114%) of the critical. The authors obtained a

straight line fit from the experimental data, figure (48a), with a trend line, equation (77), where (C) is the circulation rate and (N) the mill speed as a percentage of critical.

$$C = -0.01N + 2.2 \tag{77}$$

Employing the work of Ristow, who derived an expression for the critical speed as a function of the load fraction, Govender and Powell [6] attempted to model the circulation rate, based on equation (77). Their model would include mill operating variables such as mill speed and volume filling fraction (α). They derived an expression for the circulation rate given in equation (78).

$$C = -0.01N + \left[\frac{1}{\sqrt{1-\alpha}} + 1\right] \tag{78}$$

The validity of this expression was borne out by the fact that at a load fraction of (α = 40%) they obtained a predicted critical speed that was statistical equivalent to the experimentally derived value of (114%). The authors observed, however, that the linearity suggested by both experimental data and numerical derivation was clearly limited to certain practical speeds of (50 – 90%) and filling degrees of (15 – 50%). Similarly when (N = 0) it would appear that equation (78) would give a value of two rather than zero. Finally, since practical values of circulation rate cannot be less than one, equation (78) would have to be truncated at the point where all the charge centrifuges and cannot be valid for a fractional filling of (α = 1). These limitations make it necessary to present a more robust formulation.

In section (7.2) we presented a two cycle description of tumbling charge motion which is well supported by a cross-section of previous investigations [15, 18, 19, 23, 24, 54, 55, 65], to name but a few. Assuming uniform packing, the charge surface for a mill at rest will be nearly horizontal. The tangent to the horizontal charge surfaces (along particle layers) will be zero. There will be no mill rotation or charge circulation and hence equation (75) which describes the oscillating cycle holds true. The initial acceleration of the charge centre of mass indicates the amount of energy required to overcome the inertia of the system, as illustrated by equation (55). At low mill speeds, circulation of the charge is only possible if the conditions in (54) and/or (66) are met. Prior to this stage, if the wall friction is sufficient and as slumping begins the continued rise and slump of the charge surface leads to an alternate kinetic and potential energies associated with two fixed positions; the upper and lower angles of repose [15, 23, 24]. Hence in the ($O - S^3$) the total energy acquired by the charge due to friction at the mill wall and slip within the charge, are described by equations (54), (66) and (75). The motion of the charge in the ($O - S^3$) range is, therefore, described by the tangent of the mean angle of repose, equation (79), where (C_{charge}) is the circulation rate of the charge.

$$C_{charge} = \tan\theta_{mean} \tag{79}$$

On increasing the mill speed the charge acquires higher order energies and at some point particles deviate from the mill shell and roll down the near flat surface. The angle at which particles deviate from the mill profile is (ζ) known as the departure shoulder angle. The equilibrium condition at this point denotes the on-set of gravity-driven flows and is fully described by condition (71). The mill speed at which this condition is achieved is shown in equation (76), indicating that particles deviate at a speed equal to that in equation (76). The original charge surface moves inwards by one layer and the (CoC) assume

its initial radial and angular location. The total energy of the charge is now described by equations (76) and (79). However, the effect of the energy transfer to the charge described by equation (79) declines gradually as mill speed is increased as indicated by the graph in figure (42). Hence at higher speeds the model in equation (76) dominates. This conclusion is well supported by the fact that when the angle at the departure shoulder arrives at the upper dead end of the mill ($\zeta = 90^o$) the charge speed will be the same as the mill critical rotation speed proposed by Watanabe [18], in equation (68). Therefore, the circulation rate of the charge in a tumbling mill is described by equation (80).

$$C_{charge} = \tan\theta_{mean} + \frac{1}{2\pi}\sqrt{\frac{g\sin\zeta}{R\sin\theta_c\sqrt{1-\alpha}}} \tag{80}$$

A close examination of equation (80) reveals that the circulation rate of the charge in tumbling mills (C_{charge}) is a combination of the oscillating cycle (O – S^3) and the circulating cycle (C – RC^3). Hence the model in equation (80) accounts for all tumbling charge motion types in the plane of interest to this research. The model shows that the total energy of the charge comes partly from external forces (the effect of the mill rotation) which causes impact work and partly from internal agitation (assisted by the mill internal design vis-à-vis, lifters) which gives rise to abrasion and attrition work.

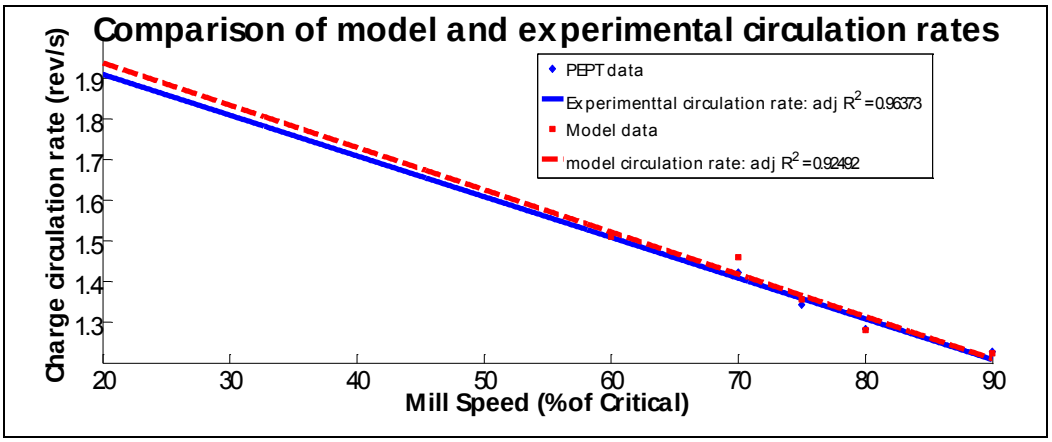

Fig 49: Validating the circulation rate model in equation (80).

The graph in figure (49) is a comparison of circulation rates obtained from PEPT experiments and the model circulation rate values obtained from equation (80). The plot, fitted with empirical lines, shows a close statistical correlation between experiment and theory thereby validating the circulation rate model.

7.4 Conclusion

From the foregoing discussion one can conclude that the circulation rate of the charge in a tumbling mill varies directly with mill speed and coefficient of kinetic friction (mill internal wall lining design) and indirectly with a number of charge features such as mean and critical angles of repose, the departure shoulder angle and the load fraction. Hence the model in equation (80) can be rewritten as in equation (81).

$$C_{ratio} = \frac{C_{charge}}{N_m} = \frac{\mu_\kappa}{N_m} + 1 \qquad (81)$$

From the plot in figure (42) and the model in equation (81) it is easy to see that the circulation of the charge starts at a higher value than the mill rotational speed but declines towards unity as the charge approaches centrifuging. A circulation rate of unity is only possible when the entire charge is centrifuging.

Chapter eight: Energy Distribution in the Grinding Environment of Tumbling Mills from a Continuum Approach

8.0 Introduction

Tumbling mills have found wide use in the fine grinding of mineral ores [1]. Grinding is a size reduction process that creates large surface areas of materials and hence enabling the liberation of valuable minerals from their matrices. In the beneficiation of mineral ores the efficiency of this process remains relatively low while its energy requirement is increasing [133]. The concomitant increase in the beneficiation cost is felt by the minerals industry. Consequently the need to improve energy utilization in these mills can hardly be overstated.

To improve the grinding efficiency of tumbling mills requires an understanding of not only the effect of the external environment on the charge but also the internal dynamics of the grinding environment. The effect of the external environment is material transport to the grinding regions that allow the application of stressing for potential breakage. The probability of particle breakage is directly related to the frequency of stressing [134 - 137]. It is, therefore, no surprise that the bulk of the efforts towards the modelling of

these devices have been directed towards understanding the frequency of energy transferred to the grinding environment (power draw). El-Shall et at [138], emphasized that material transport in these mills depends primarily on the pulp fluidity which in turn is influenced, among other things, by the nature of particle-particle interactions and particle-mill wall interactions, A notable authority on comminution modelling, King [139], postulated that "until at such a time when the patterns of energy distribution and stress application are known, breakage in complex system cannot be synthesized from the universal single-particle breakage functions." Consequently the influence of circulation rate of the tumbling charge on the power draft of the mill cannot be ignored.

The most common approach to quantifying power drawn by the charge in most tumbling mills is to compute the power from a torque arm approach. The values so obtained are compared with the motor or mill shell power as recorded by the distributed controls systems readings. However, the disparity between experiment and theory remains large particularly at low mill speeds [140]. In chapter seven we reported the development of a number of grinding media mill models using positron-emission-particle-tracking (PEPT) data. The experimental approach is highly suited to allow us to effectively examine the assumption that the charge in these mills circulate at a constant rate of unity. A notable outcome has been the development of a model linking the circulation rate of charge particles with physical mill parameters (load fraction, shoulder angle and friction). This model allows for characterization of the shape of the charge body into distinct flow regimes and hence the transitions between these regimes can now be mapped to more physical geometric interpretations. The model also allows the distributions of energy in the grinding environment to be analysed, from approaches such as continuum mechanics among others, which may lead to the development of newer power models.

8.1 Review of Power Draw Models

8.1.1 The Morrell Power Draw Model

In his PhD thesis Morrell [54], studied the grinding regions of the charge in tumbling mills, in particular, the toe and shoulder angles and their influence on charge behaviour. His models for evaluating the angles subtended by these two grinding regions at the mill centre are at best geometric. One notable outcome of his work was in the assessment of slip planes in the *en-masse* region of the charge. He developed a normalized model for the change in tangential velocity across particle layers. His findings that "considerable variations in tangential velocities occur along slip planes" are seminal and lead calls for continued analysis of steady state conditions in these mills. In the bulk of this work he attempted to relate power draw to the motion and shape of the charge in tumbling mills. In this regard he proposed three approaches to calculating the power drawn during milling: the torque approach, frictional force approach and the energy balance approach. These approaches are briefly described below.

A. *Torque approach*

Here the equilibrium of forces acting through the mill axis of rotation is examined. In the approach the author [54], assumed that the torque exerted by the charge is equal and opposite to that exerted on the charge by the mill, taken about the mill rotational axis. This is used to formulate the power exerted by an elemental mass with the total power drawn by the entire charge obtained by integration, see figure (50).

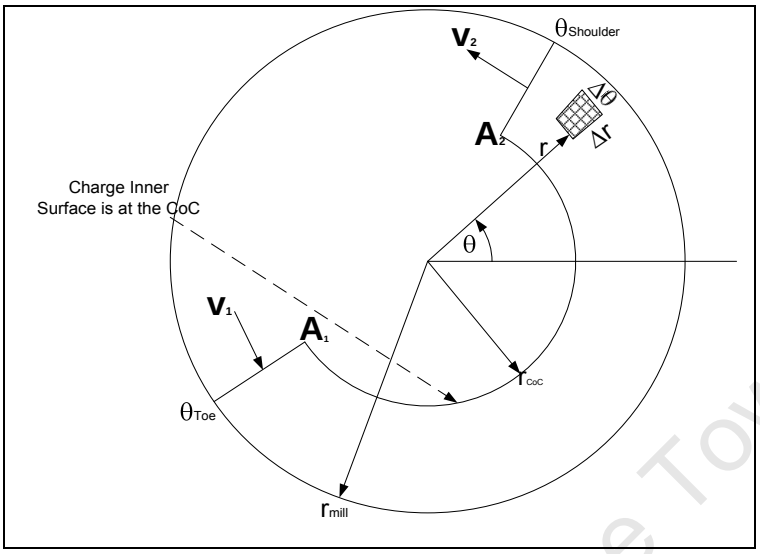

Fig 50: Charge geometry showing the shoulder and toe angles. Redrawn after Morrell [54].

$$Power = \tau \times 2\pi N \tag{82}$$

Where (τ) is the torque exerted by an elemental area and (N) is the mill rotational speed. Hence by integration:

$$P_{net} = 2\pi g L \rho_c \int_{r_i}^{r_m} \int_{\theta_T}^{\theta_S} N_r r^2 \cos\theta d\theta dr \tag{83}$$

In equation (83), (L) is the effective mill internal length, (ρ_c) is the charge density, (r_i) radius of the charge inner surface, (r_m) the mill radius, (θ_S) the departure shoulder angle and (θ_T) the impact toe angle. By considering the geometry of the charge in figure (50), he obtained the net power as shown in equation (84).

$$P_{net} = \frac{\pi g L \rho_c N_m r_m}{3(r_m - z r_i)} \left[2r_m^3 - 3z r_m^2 r_i + r_i^3 (3z - 2) \right] \left[\sin\theta_S - \sin\theta_T \right] \quad (84)$$

Model excludes power required to provide kinetic energy to the charge from the rotating mill.

B. *Friction force approach*

In this approach the mill is said to transfer energy to the charge through friction at the mill wall and friction between particle layers. Morrell [54], derived an equation for this frictional force at a radius (r), which is half way between the inner surface (r_i) and the mill shell (r_m). Thus the charge in the mill can only be moved by the transfer of energy from the rotating shell given by equation (85).

$$Power = F_{F_r} \times V_r = V_r L \rho_c r \cos\theta d\theta dr \quad (85)$$

Where (F_{Fr}) is the frictional force and (V_r) is the tangential velocity along the particle layer at a radius of (r). Hence the net power can be evaluated from equations (86) and (87).

$$P_{net} = \int_{r_i}^{r_n} \int_{\theta_T}^{\theta_S} F_{F_r} \times V_r \quad (86)$$

$$P_{net} = gL\rho_c \int_{r_i}^{r_m} \int_{\theta_T}^{\theta_S} V_r \cos\theta d\theta dr = 2\pi gL\rho_c \int_{r_i}^{r_m} \int_{\theta_T}^{\theta_S} N_r r^2 \cos\theta d\theta dr \quad (87)$$

This is the same results as obtained from the torque arm approach in section (A) above.

C. *Energy balance approach*

In this approach, Morrell [54], attempts to include the kinetic energy transferred to the charge by the effect of the mill rotation. He investigated the net rate of potential and kinetic energy generation within the charge. For a given element, see figure (54), the volumetric flowrate is given as:

$$V_{flowrate} = \text{Area} \times \text{tangential velocity} \quad (88)$$

And the mass flowrate as:

$$M = V_{flowrate} \times \rho_c \quad (89)$$

Hence the potential energy transferred to the charge is calculated from equation (90).

$$P.E. = Mgh = V_r \rho_c Lghdr \quad (90)$$

Where the height of the elemental volume is at (h) and is given by equation (91).

$$h = r(\sin\theta_S - \sin\theta_T) \tag{91}$$

He determined the kinetic energy transferred to the charge as in equation (92).

$$K.E. = \frac{1}{2} M V_{flowrate}^2 = \frac{V_r^3 \rho_c L}{2} dr \tag{92}$$

The power is the sum of the potential and kinetic energies transferred to the charge by the mill rotation, shown in equations (93) to (95).

$$P_{net} = \int_{r_i}^{r_m} potential + kinetic \; dr \tag{93}$$

$$P_{net} = \int_{r_i}^{r_m} \left[V_r \rho_c L g h + \frac{V_r^3 \rho_c L}{2} \right] dr \tag{94}$$

$$P_{net} = \frac{\pi g L \rho_c N_m r_m}{3(r_m - z r_i)} \left[2r_m^3 - 3z r_m^2 r_i + r_i^3 (3z - 2) \right] \left[\sin\theta_S - \sin\theta_T \right] + L\rho_c \left\{ \frac{N_m r_m \pi}{r_m - z r_i} \right\}^3 \left[(r_m - z r_i)^4 - r_i^4 (z-1)^4 \right] \quad (95)$$

8.1.2 The Heuristic Power Draw Model

Assuming the bulk of the charge is found in the region lying below the charge repose, then its centre of gravity must be in this region. This charge repose was, however, mistakenly taken to be the angle of repose of the charge by some researchers [142, 143], as shown in figure (51). According to Hogg and Feurstenau [142] and later Haris et al [143], this centre of gravity will exert a torque at the mill centre given by equations (96).

$$T = MgR_{CoM} \sin(\alpha) \quad (96)$$

$$P = 2\pi T \Phi = 2\pi MgR_{CoM} \sin(\alpha)\Phi \quad (97)$$

Where (Φ) is the mill rotational frequency measured in revolutions per second (rps). Here (T) is the torque exerted by the charge of mass (M), (g) is the acceleration due to gravity, (R_{CoM}) the radial distance of the centre of mass of the charge (CoM), and (α) the angle of repose. The power can thus be calculated from equation (97).

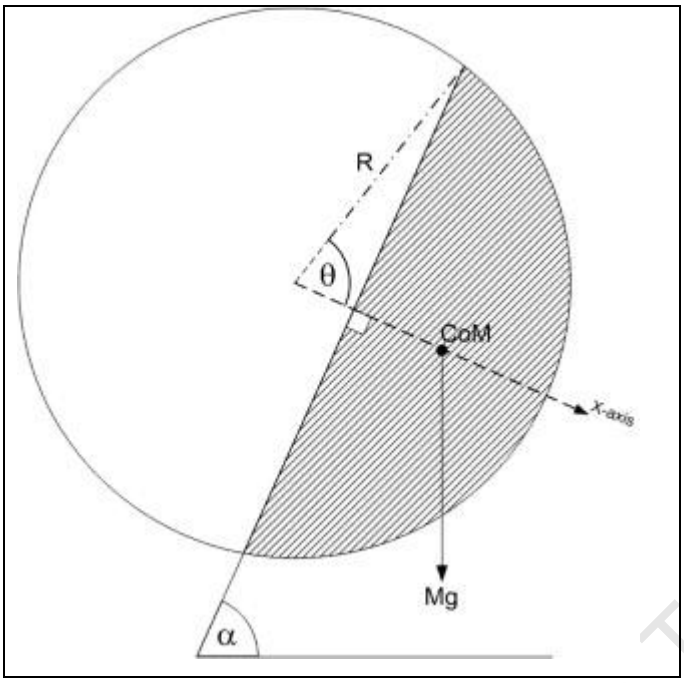

Fig 51. Basic geometry of charge used in the torque-arm implementation of power draw [144]

A recent improvement on this model was reported by Govender and Powell [144], who eliminated the angle of repose of the charge and replaced it by the angular orientation of the centre of mass (statistical centre of mass as obtained from equation 27, see chapter five). Their model is therefore based on the polar coordinates of the centre of mass and is given in equation (98).

$$P = MgR_{CoM}\cos(\theta_{CoM})\Omega \tag{98}$$

Where (Ω) is the angular frequency of the mill measured in (rad s^{-1}). Other methods that have been reported for determining the power draw in tumbling mills include the bin algorithm [140]. In this method the cross-section of the mill is discretized into a number of bins and the power exerted by each discrete bin is calculated. Bbosa et al [140], reports this method reduced the

absolute difference between experiment observations and theoretical results as compared to the torque-arm approach.

8.2 The CoC and the Quasi-plug Flow Region

The centre of circulation (CoC) of the charge is a geometric location about which the entire charge appears to circulate often referred to as the "eye of the charge." A scheme for the determination of this location has been suggested, [24], through the use of three control surfaces. The significance of the location is underscored by the fact that its correct location was experimentally observed to yield the maximum circulation rate value for the charge at all mill speeds [142]. Between the (CoC) and the mill shell is a quasi-plug flow region whose motion is influenced mainly by the effect of the mill rotation. This region begins at the impacting point (impact toe) and ends at the point of departure (departure shoulder) where the charge particles deviate from the mill profile. It is therefore the region where the charge remains in contact with the mill shell. The angle formed by the segment containing this region is termed the "charge repose" and is a measure of the spread of the charge (shape of charge).

During milling the effect of the mill rotation is to impose a gradient on the system and at a constant speed the system may evolve to a time invariant state often known as steady state – forced flows. The time invariant state of such a driven system is not an equilibrium state in that the system may or may not be uniform as is prominently observed in the quasi-plug flow region. The length of the quasi-plug flow region can become pronounced at high speeds as the charge repose approaches the characteristic (360^{o}). The trajectory followed by this flow system has been the subject of numerous investigations [6, 15, 16, 17, 18, 54, 58, 63 – 69, 79 – 81, 109 – 113, 118, 124, 125, 135, 142 - 144]. While these reports detail the formulation of robust models, none has attempted to integrate the tumbling charge circulation rate into a model for the

power draw. The circulation rate model reported in chapter seven is used here to develop a mechanical energy model that compares well with the equations of change derived from non-Newtonian fluid dynamics.

8.3 The Mechanical Energy Model

Grinding mill performances are affected by many variables such as production capacity, total energy consumed during milling as well as liner design and life. Several investigations have focused on developing newer methodologies for improving these performances.

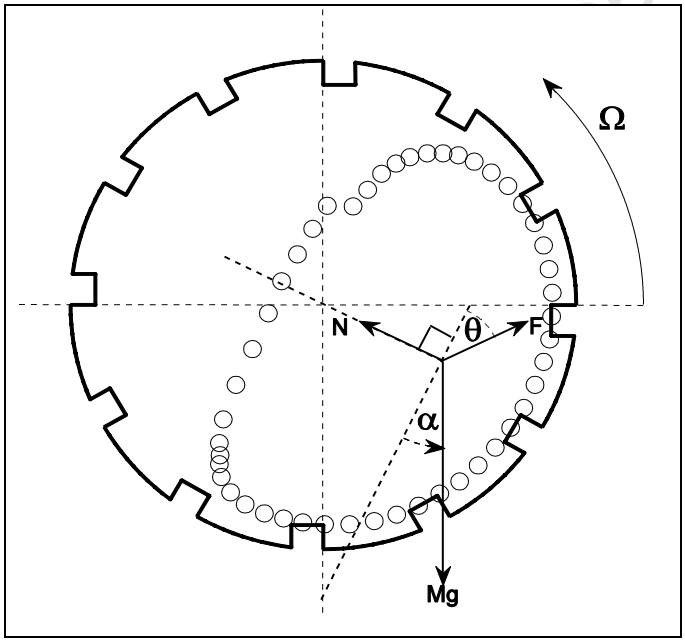

Fig 52: The torque-arm approach [23].

To date the most important method of modelling power drawn by the charge is to compute the power from a torque-arm approach. This method is often called the "*Traditional power approach*" where the torque-arm is taken from the centre of mass (CoM) and about the mill centre, figure 52. The model is also

based on the mill rotational frequency, equation (99). The limitation of this approach has been well documented by Bbosa et al [140], who concluded that the underlying assumption of a circulation rate of unity may be affecting the model calculations. A more robust approach then is to take the torque-arm about the charge centre of circulation (CoC) and to use the charge rotational frequency (C_{charge}), equation (100). In this equation the moment of the charge centre of mass (CoM) is taken about the charge centre of circulation (CoC) rather than the mill centre as in previous models. This approach could give a measure of the mechanical energy acquired by the charge during milling, see figure 53.

$$P_{CoM} = [Mg\cos(\theta_i)]R\Omega \tag{99}$$

$$P_{mech} = MgC_{charge}[x_{CoM} - x_{CoC}] \tag{100}$$

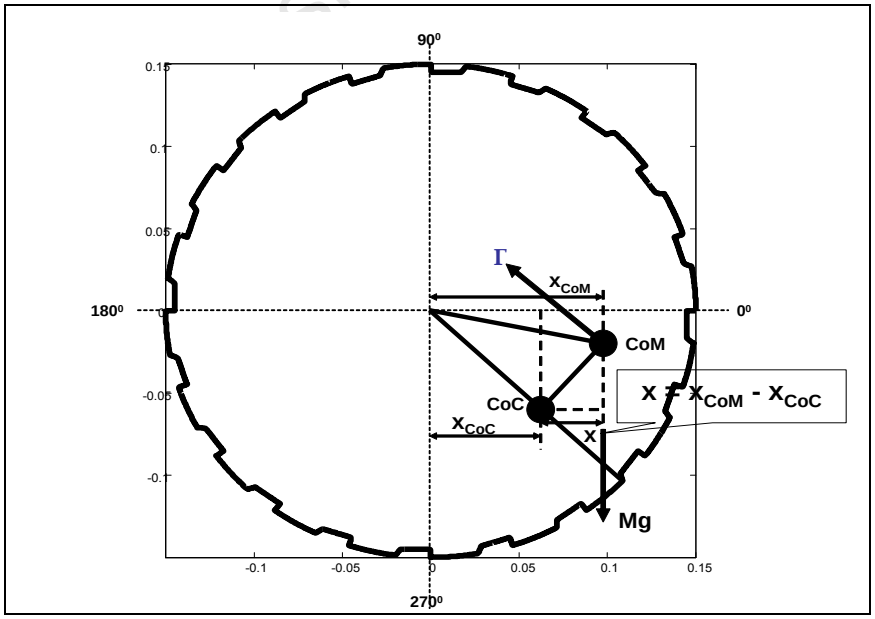

Fig 53: The torque-arm approach applied about the charge center of circulation.

The charge in a rotating mill does not dictate its own direction of flow. The direction of flow is imparted to it by the effect of the mill rotation and the shape of the free (cascading) surface. Within a given reference force frame and at steady state the total energy of the system, to include *kinetic, potential, heat, etc*, must remain conserved over time regardless of the choice of reference force frame. Therefore one can conclude that the net-energy transferred to the grinding environment is equal to the difference between the power readings (at the distributed control systems) for the mill running at a certain speed firstly with charge and then with no charge.

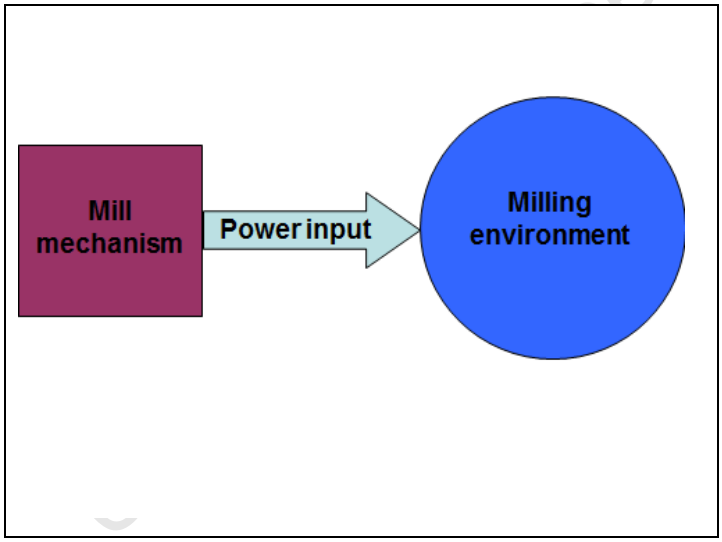

Fig 54: Energy transfer to milling environment.

In table (10) power readings recorded using Lab-view signal express are shown for the case of no lifters. For the set of experiments conducted at the iThemba LABS we obtained power readings for no load runs and for runs with (40%) load. The difference in the power readings is termed here as charge power (P_{charge}) see column four of table (10).

This difference is obtained as the area between the two curves in the graph in figure (55). In the plot the red line represent power drawn by the mill with (40%) load while the blue line represent power drawn by the mill with no load. We postulate that the total energy transferred to the circulating charge (as represented by the area ABCD in figure 55) goes partly as mechanical energy acquired by the charge (P_{mech}) and partly as energy losses during grinding (P_{loss}), equation (101).

$$P_{charge} = P_{mech} + P_{loss} \tag{101}$$

Table 10: Power draw for (0mm) lifters.

Mill Speed	**Power (j/s = W)**			
% critical	**No load**	**40% load**	**Charge power**	**Mech power (P_{mech})**
	(1)	**(2)**	**P_{charge} = (2) – (1)**	**Equation (100)**
20	0.663163	1.092192	0.429028	0.194468
25	0.780192	1.313760	0.533568	0.380996
30	0.943545	1.640516	0.696572	0.503632
35	1.102021	1.922225	0.820204	0.511173
40	1.255622	2.240219	0.984598	0.668136
45	1.401908	2.607696	1.205689	0.873121
50	1.572575	2.941161	1.368587	1.212944
55	1.731073	3.382632	1.651581	1.076916
60	1.877337	3.631135	1.753798	1.460990
65	2.035814	3.966417	1.930604	1.628768
70	2.199166	4.488876	2.289704	1.762118
75	2.345452	4.623228	2.277776	2.085077
80	2.503929	5.016053	2.512124	2.397343
84	2.674593	5.362553	2.687957	2.512804
90	2.820882	5.728504	2.907622	2.759014

Since the system is isolated, and running at steady state a constant force is required to maintain motion (hence $\Delta F = 0$). Equation (101) then gives the distribution of the energy into the grinding environment and the essential difference between equations (100) and (101) is the energy losses term (P_{loss}).

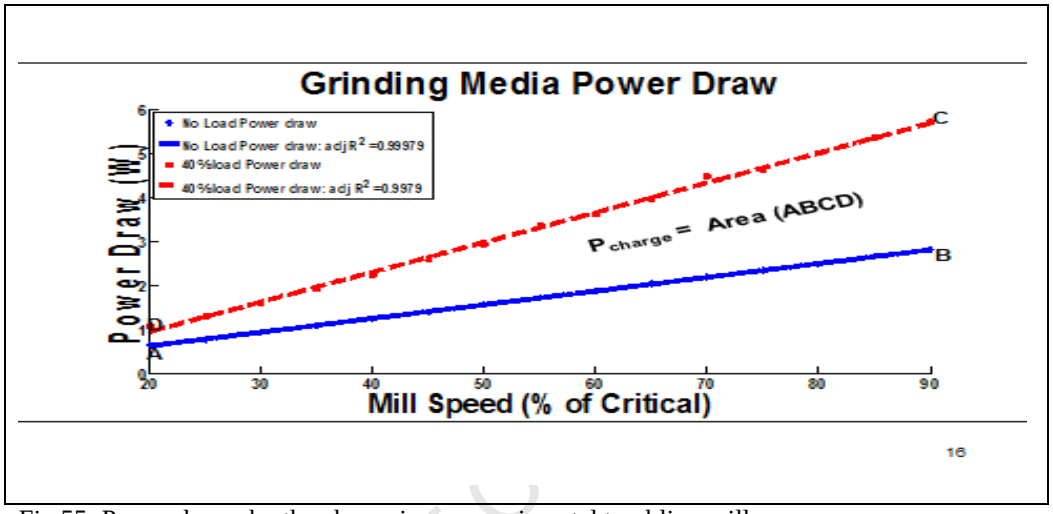

Fig 55: Power drawn by the charge in an experimental tumbling mill.

Experimentally, if the two equations are plotted the area between their graphs would represent this energy losses term, as shown in figure (56). In this figure the black line represents the charge power (P_{charge}), shown in equation (101) and table (10) and determined as area ABCD in figure (55). The green line represents the mechanical power determined from equation (100). The difference between these two trends is a measure of the power lost in grinding.

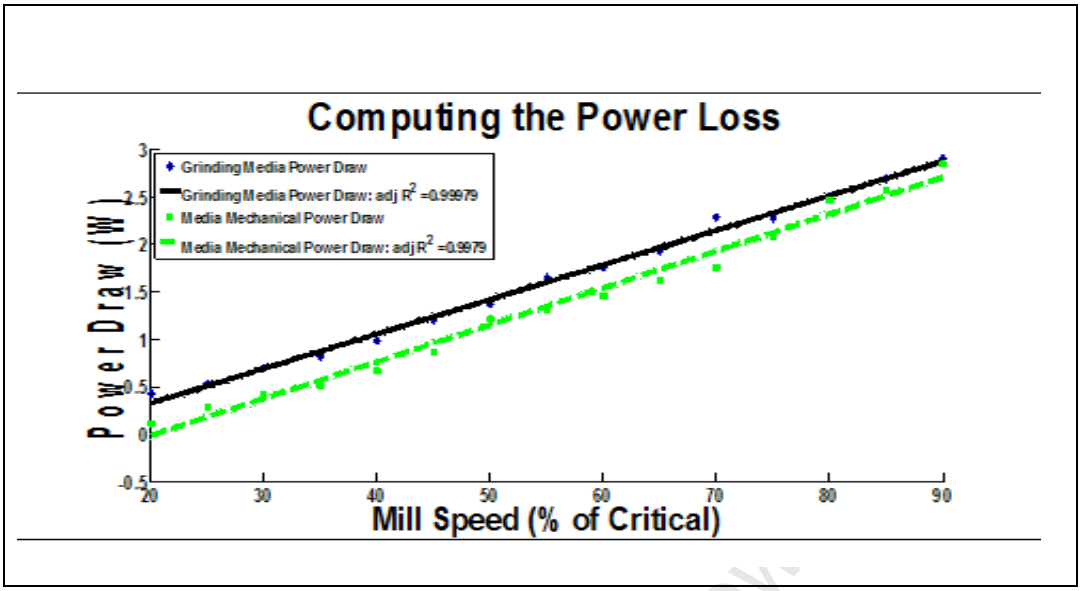

Fig 56: Experimental power measurements using lab-view signal express.

8.4 A continuum Based Energy Model of Tumbling Mills

For most non-Newtonian fluids rheological properties of many different flow conditions are best studied from the constitutive equations of change developed from continuum mechanics. Here the precise dynamics of the complex flow system is used to formulate partial differential equations that approximate to the highly desired Newtonian behaviour. The approach is to study the mass, energy, momentum and angular momentum transport in the system at the three levels of macroscopic, microscopic and molecular [13]. For instance in the literature we find the reported energy losses at the macroscopic and microscopic levels occur through particle-particle interactions, particle-mill wall interaction, conversion of energy into kinetic energy of the products, sound, heat as well as deformation and wear of the grinding media. At the molecular level energy is utilized on elastic and plastic deformations, rearrangement of lattices, energy required for creating new surfaces and mechano-chemical reactions [138].

Mechanical motion in grinding mills resulting from drive shafts, push rods, or similar devices are known as driven flows. These driven flows combined with friction or drag may lead to velocity gradients and hence viscous shear stresses may build up within the charge. Noether's theorem [148], states that there exist a one-on-one correspondence between the conservation laws and differentiable symmetries of physical systems. Hence conservation laws based on balances of mass, energy, momentum and angular momentum can be employed to help elucidate the complex phenomenon of the distribution of energy in the grinding environment of industrial tumbling mills. For complex flow systems, the assumption of a time-invariant steady state allows one to apply the theory of relativity in assessing the mass-energy equivalence of the system. We found that conversion of *rest mass* to kinetic energy (mobile mass) and the conversion of kinetic energy to internal energy (reversible and irreversible), heat or light could be used to assess energy losses within the grinding environment, particularly arising from viscous shear stresses.

In applying these laws to the tumbling mill scenario we approached the problem from the microscopic level deriving the partial differential equations relevant to our analysis, see figure (57). Because the velocity of the tracer particle is dependent on its position with time, its flow can be described by partial differential equations. These equations of change are then scaled up through integration to the macroscopic level. Our coordinates are in the (r – radial) and (θ – angular) directions for the circular face of the mill and (z) is in the axial direction. We choose values of (r), (θ) and (z) such that the elemental volume can hold only one particle at a time. That is, the volume is like a small fluid element (one tracer particle location) moving with the fluid. Between the toe and shoulder the fluid element moves through a cylindrical space with unit vectors (i), (j) and (k) in the (r), (θ) and (z) directions respectively, see figure (58). The tangential velocity field in this coordinate system will be given as:

$$\mathrm{V} = u\mathrm{i} + v\mathrm{j} + w\mathrm{k} \tag{102}$$

On this basis the following definitions hold. Velocity components:

$$u = u(r, \theta, z, t) \tag{103}$$

$$v = v(r, \theta, z, t) \tag{104}$$

$$w = w(r, \theta, z, t) \tag{105}$$

And the bulk density:

$$\rho = \rho(r, \theta, z, t) \tag{106}$$

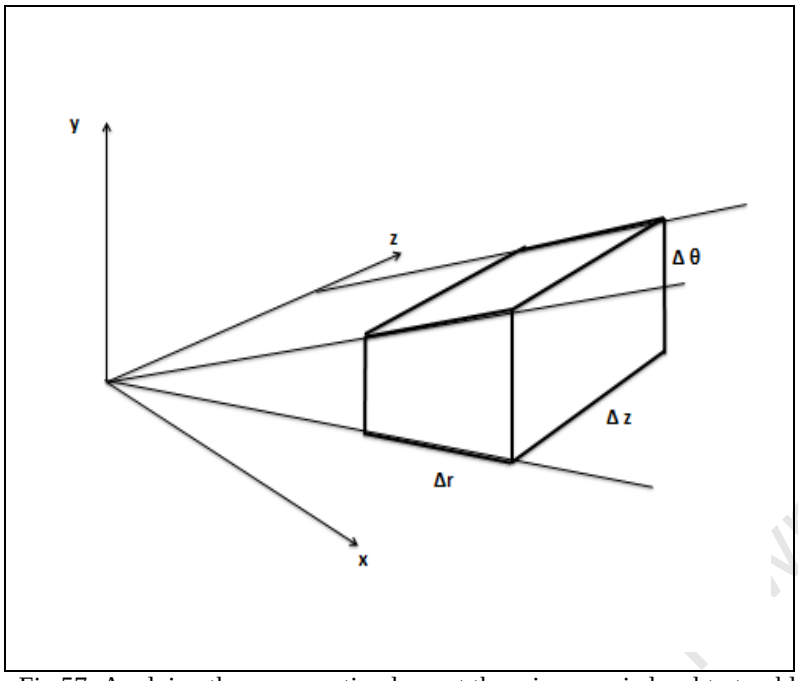

Fig 57: Applying the conservation laws at the microscopic level to tumbling mills.

In figure (58), particles enter the quasi-plug flow region at the bulk toe and leave at the departure shoulder. If we consider the (bead) particles to be uniformly packed the cross-sectional area at the bulk toe (A_1) will be the same as that at the departure shoulder (A_2), hence ($A_1 = A_2 = A$). Assuming that the time-smoothed velocity is uniform across these cross-sections and that the bulk density of the particles entering these cross-sections are uniform for this system (use of beads of the same diameter), we can integrate the microscopic equations of change, obtained using our coordinate system, to yield the time-dependent macroscopic equations. These derivations follow a similar procedure to Bird et al, [14] and the integrations yield the same components indicating that these equations of change may be independent of the choice of coordinates systems employed.

8.4.1 The Continuity Equation

The continuity equation at the microscopic level, equation (107), is obtained from mass balances in the elemental volume defined by $\Delta\theta\Delta r\Delta z$, figure (57).

$$\Delta r\Delta\theta\Delta z\frac{\partial\rho}{\partial t} = \Delta\theta\Delta z\left[\ \rho v_{r\ r} - \rho v_{r\ r+\Delta r}\right] + \Delta r\Delta z\left[\ \rho v_{\theta\ \theta} - \rho v_{\theta\ \theta+\Delta\theta}\right] + \Delta r\Delta\theta\left[\ \rho v_{z\ z} - \rho v_{z\ z+\Delta z}\right] \tag{107}$$

In the limit as Δr, $\Delta\theta$, $\Delta z \rightarrow 0$:

$$\frac{\partial\rho}{\partial t} = -\left(\frac{\partial}{\partial r}\rho v_r + \frac{\partial}{\partial\theta}\rho v_\theta + \frac{\partial}{\partial z}\rho v_z\right) \tag{108}$$

Or in tensor notation:

$$\frac{\partial\rho}{\partial t} = -\nabla.\rho v \tag{109}$$

Equation (109) shows that the rate of mass increase within the elemental volume is equal to the net rate of mass addition per unit volume by convective processes. In other words, it is the net rate at which the tracer particle occupies the elemental volume. The equation indicates that the derivation of the continuity equation is independent of the choice of coordinate system employed. For velocities at the bulk toe and departure shoulder of (v_T) and (v_S) respectively and for the same bulk density, integration of equation (109)

between the toe and shoulder angles yields the macroscopic mass balance, shown in equation (110).

$$\frac{d}{dt} m_{tot} = -\rho A \langle v_T - v_S \rangle \tag{110}$$

Equation (110) is an illustration of the particle build-up within the quasi-plug region and for slippage of the charge to be prevented or minimized the bulk velocity must be seen to be greater than the velocity at the point of departure. From this equation it can be seen that mass is conserved in the system of interest, see figure (58). A special state (steady state) macroscopic mass balance is achieved if the rate of tracer particle flow in the elemental volume Is constant. For such a condition then the tracer particle moves with equal velocities between the bulk toe and the departure shoulder (equation 111). Hence forced flows can approximate the unidirectional character of equilibrium systems only if the flow is laminar (uniform).

$$0 = -\rho A \langle v_T - v_S \rangle : \qquad v_T = v_S = v_m \tag{111}$$

In equation (111), (v_m) is the tangential velocity of the mill.

8.4.2 The Momentum Equation

Newton's second law is employed to derive a motion equation from momentum balances within the elemental volume ($\Delta r \Delta\theta \Delta z$). The net rate of momentum change in the elemental volume occurs both by convective and

molecular transport. The momentum is derived in each coordinate direction. The net rate of momentum addition in the θ-direction is given as:

$$\Delta r\Delta\theta\Delta z\frac{\partial}{\partial t}\rho v_\theta = \Delta r\Delta z\left[\ \Phi_{\theta\theta}\ _\theta - \ \Phi_{\theta\theta}\ _{\theta+\Delta\theta}\right] + \Delta\theta\Delta z\left[\ \Phi_{r\theta}\ _r - \ \Phi_{r\theta}\ _{r+\Delta r}\right] + \Delta\theta\Delta r\left[\ \Phi_{z\theta}\ _z - \ \Phi_{z\theta}\ _{z+\Delta z}\right] + \Delta r\Delta\theta\Delta z\rho g_\theta \quad (112)$$

In the limit as Δr, $\Delta\theta$, $\Delta z \rightarrow 0$:

$$\frac{\partial}{\partial t}\rho v_\theta = -\left(\frac{\partial}{\partial\theta}\Phi_{\theta\theta} + \frac{\partial}{\partial r}\Phi_{r\theta} + \frac{\partial}{\partial z}\Phi_{z\theta}\right) + \rho g_\theta \quad (113)$$

This is the partial derivative in θ-direction. In a similar way we can obtain the partial derivatives in (r) and (z) as:

$$\frac{\partial}{\partial t}\rho v_r = -\left(\frac{\partial}{\partial r}\Phi_{rr} + \frac{\partial}{\partial\theta}\Phi_{\theta r} + \frac{\partial}{\partial z}\Phi_{zr}\right) + \rho g_r \quad (114)$$

$$\frac{\partial}{\partial t}\rho v_z = -\left(\frac{\partial}{\partial z}\Phi_{zz} + \frac{\partial}{\partial\theta}\Phi_{\theta z} + \frac{\partial}{\partial r}\Phi_{rz}\right) + \rho g_z \quad (115)$$

Equations (113) – (115) can be combined to give the motion equation in (116).

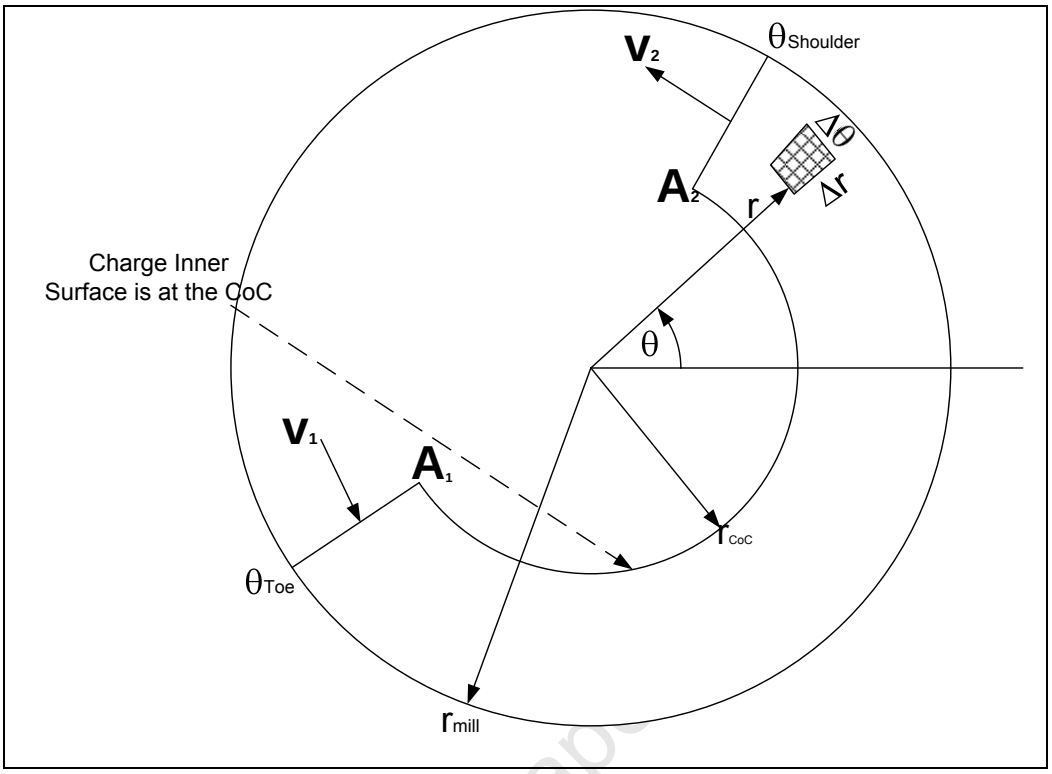

Fig 58: Applying the conservation laws at the macroscopic level to tumbling mills, redrawn after Morrell [54].

$$\frac{\partial \rho}{\partial t} = -\ \nabla.\rho \mathrm{vv}\ - \nabla p - [\nabla.\tau] + \rho g \tag{116}$$

By vector-tensor notation equation (116) can be rewritten as in equation (117).

$$\frac{\partial}{\partial t}\rho v_i = -\ \nabla.\Phi_{\ i} + \rho g_i \quad \text{for } i = r, \theta, \text{z} \tag{117}$$

Where $\Phi = \rho \mathrm{vv} + p\delta + \tau$ (118)

Here (Φ) is the combined momentum flux tensor, (ρ**vv**) is the convective flux tensor, ($p\delta$) the pressure term and (τ) is the shear stress term. Equation (117) reads; the mass times acceleration of fluid is equal to the pressure force, viscous force and the external forces. That is, it is the same as newton's second law of motion with the fluid element moving at a velocity (v). If the condition in equation (111) is applied to equation (116) one obtains the Stokes flow equation as:

$$\nabla.\rho \mathbf{vv} = -\nabla p - [\nabla.\tau] + \rho g \tag{119}$$

Again this condition approximates steady state in the flow stream. Since pressure in a fluid is constant and the density is assumed to be uniform, equation (119) shows that energy losses in the grinding environment may occur due to shearing effect between particle layers.

8.4.3 The Energy Model

The total energy of a system can be changed by mechanical processes involving motion and is defined by the amount of work done on the system. On this basis we seek to derive an energy model that sufficiently illustrates the decomposition of this driven flow energy into components of mechanical work, heat, pressure work and energy dissipated due to viscous shear stresses within the charge. In an infinitesimal time interval the work done on a particle is given by the dot product of the force acting on it and the resulting displacement. In other words, it is the dot product of its velocity and momentum. At the microscopic level the mechanical energy is derived by taking the vector dot product of the momentum equation (116), with the velocity vector.

$$\frac{\partial}{\partial t}\left(\frac{1}{2}\rho v^2+\rho\Phi\right)=-\left(\nabla.\left(\frac{1}{2}\rho v^2+\rho\Phi\right)\mathrm{v}\right)-p\ -\nabla.\mathrm{v}\ -\ -\tau:\nabla\mathrm{v}\ -\ \nabla.p\mathrm{v}\ -\ \nabla.[\tau.\mathrm{v}] \tag{120}$$

This equation simply reads: the rate of addition of kinetic and potential energies in the elemental volume is equal to the rate of increase of kinetic and potential energies in the volume less the rate of conversion of kinetic energy into reversible and irreversible internal energies, less the effect of pressure work, less the effect of viscous dissipation due to shear gradients. Equation (120) indicates that no matter what form energy takes it always exhibits relativistic mass and hence the conservation laws are held true for these derivations. By integration of equation (120) between the bulk toe and departure shoulder, using our coordinate system, yields the macroscopic model shown in equation (121). Again we find the equation has mechanical components of kinetic and potential energy build-up in the quasi-plug flow region together with the pressure work done. The terms are seen to vary from the toe to the shoulder and exert a torque on the charge about a point of circulation (the CoC).

$$\frac{d}{dt}\ K+\Phi\ =\rho\mathrm{A}\left(\left(\frac{1}{2}\left\langle v_T^3-v_S^3\right\rangle\right)+\ \Phi_T\left\langle v_T\right\rangle-\Phi_S\left\langle v_S\right\rangle\ \right)+A\ \ p_T\left\langle v_T\right\rangle-p_S\left\langle v_S\right\rangle$$
$$+W_w+\int_{V\,t}p\ \ \nabla.\mathrm{v}\ \ dV+\int_{V\,t}\ \tau:\nabla\mathrm{v}\ \ dV \tag{121}$$

The remaining terms represent energy that may be lost during grinding by various means. Theoretically, this accounts for the power losses illustrated in equation (101).

$$E_{loss} = W_w + \int_{V\ t} p\ \nabla.\mathrm{v}\ dV + \int_{V\ t} \tau : \nabla \mathrm{v}\ dV \tag{122}$$

The friction model in equation (123) illustrates the amount of energy required to prevent slippage of the charge down the mill wall and hence (W_w) (in equation (122) is the work done by the mill wall on the charge. This work we project as a function of the mill internal design and the mill rotational speed, equation (124). The last two terms in equation (122) will see mechanical energy increase or decrease depending on expansion/compression work as well as viscous dissipation due to shear stresses. Again the system mass and energy remain conserved throughout this process. Equation (121) then gives the complete distribution of energy in the grinding environment during milling.

$$\mu_w > \frac{g r_i \sin\theta_i}{R^2 \left[g\ \sin S - \sin T\ + a\ (S - T) \right]} \tag{123}$$

$$W_w = W_w(\mu_W, \Omega) \tag{124}$$

On the basis of equation (121) we can identify two further case scenarios or boundary conditions for the case of the tumbling mills.

A. Case Scenario One: Flow is Incompressible

In the first scenario we examine the situation where the flow system is incompressible and hence eliminating the compression/expansion term to obtain equation (125).

$$\frac{d}{dt}\ K+\Phi\ =\rho A\left(\left(\frac{1}{2}\left\langle v_T^3-v_S^3\right\rangle\right)+\ \Phi_T\left\langle v_T\right\rangle-\Phi_S\left\langle v_S\right\rangle\ \right)+A\ \ p_T\left\langle v_T\right\rangle-p_S\left\langle v_S\right\rangle\ +W_w \\ +\int_{V\ t}\ \tau:\nabla \mathrm{v}\ \ dV \tag{125}$$

From equation (125) it can be seen that energy losses occur from work done at the mill wall and shear dissipation due to viscosity. This energy loss is given by equation (126) whose first term (W_w) is obtained from equation (124).

$$E_{loss}=W_w+\int_{V\ t}\ \tau:\nabla \mathrm{v}\ \ dV \tag{126}$$

For non-Newtonian couette flows, the (n = 2) power law gives a linear distribution of solids velocity [13, 14]. This velocity distribution is given in equation (127) on the basis of which the shear stress distribution in the quasi-plug flow region is obtained, equation (128).

$$V_\theta=R_m\Omega\left(\frac{r-R_e}{R_m-R_e}\right) \tag{127}$$

$$\tau_{r\theta} = \frac{k}{r^2}\left(\frac{R_e R_m \Omega}{R_m - R_e}\right)^2 \tag{128}$$

Equations (127) and (128) are taken directly from Bird [13] and Bird eta l [14].

B. Case Scenario Two: Wet Runs

In the second scenario we examine the case of wet runs. With good lifter designs, such that much of the charge is cascading and cataracting, energy losses from friction at the mill wall as well as through shear stresses can be eliminated giving rise to a reduced model as in equation (129).

$$\begin{aligned}\frac{d}{dt}\ K+\Phi\ &= \rho A\left(\left(\frac{1}{2}\left\langle v_1^3 - v_2^3\right\rangle\right) +\ \Phi_1\left\langle v_1\right\rangle - \Phi_2\left\langle v_2\right\rangle\ \right)\\ &\quad + A\ \ p_1\left\langle v_1\right\rangle - p_2\left\langle v_2\right\rangle\end{aligned} \tag{129}$$

Equation (129) is a mechanical energy model that gives the time rate of kinetic and potential energy build-up in the quasi-plug flow region and the pressure work. The model compares well with the model in equation (100). They both indicate rotational motion about a given point (CoC). Both equations (100) and (129) illustrate the amount of energy captured by the charge during milling and will have a significant impact on several simplifying breakage rate assumptions. However, according to Bird et al [14], "when we derive a flow field from the equations of change it is not necessarily the only physically admissible solution. Therefore emphasis must be placed on experiments in fluid dynamics." As a consequence these equations must be subject to rigorous

experimental validation as suggested in the recommendations, see chapter nine.

Chapter nine: Conclusions and Recommendations

9.0 Introduction

The objective of this study was to analyse the motion of tumbling mill charge so as to provide a fundamental understanding of the circulation rates of the charge in these mills. It is a well-known fact that a large number of both defined and undefined variables encountered in modelling and optimization of tumbling mills have an influence on achieving steady state conditions in these mills. At such a state the circulation rate of the charge can be measured using the schemes developed in this thesis and hence allowing the energy distribution in the grinding environment to be analysed. The effect of charge mixing, friction and/or drag at the mill wall and between particle layers, the existence of viscous shear stresses due to velocity gradients are all known to be describable by physical laws as applied to these mills. Experimentally, the build-up of critical mass at the toe region can be examined and its influence on limiting the effect of friction and/or drag within the charge analysed. Theoretically, the changes in energy, momentum and angular momentum in the ascending *en-masse* region can be analysed and modelled. This chapter details the recommendations for future work on tumbling charge motion.

9.1 Recommendations

Due to scope and time constraints a number of possible objectives were not investigated in this research. Results showed that the circulation rates of the charge in these mills are not constant at different operating conditions. Indeed the circulation rate varied with measurable parameters typically encountered in industrial operations. However, much remains to be done, specifically on further developing the Fourier method, accurate determination of the departure shoulder angle and (CoC) location and the examination of the influence of circulation rates on current power draw descriptions.

9.1.1 Fourier Methods

Section (5.1.3B) details the Fourier method used to extract circulation rates data from the PEPT trajectory field of the tracer particle. Spatial plots were obtained that show harmonics occurring at some point away from the fundamental harmonic and the position of these represented the circulation rates for the given mill speed. However, it was observed that higher order harmonics may sometimes occur in the spectral plots. These may represent higher order charge circulations in the mill and could be as a result of unsteady flows nearer to the end of the experimental run. However there may be better physical interpretations of this occurrence and its consequence for mill performance needs to be further investigated.

9.1.2 The Centre of Circulation (CoC) Location

In this thesis two methods were used to determine the (CoC) location. The first method utilizes the ideas of Powell and McBride [24] and in the second we used manual identification from trajectory fields plotted in matlab. However,

for both methods the (CoC) location remains highly unstable and is at best rough estimates. Because the charge circulates about the (CoC) the circulation rate was found to be higher nearer to the correct (CoC) location. This dependency means developing a better scheme to accurately determine the (CoC) location will yield more accurate values of the charge circulation rates and enhance the modelling of power quantification and breakage rates.

9.1.3 The Departure Shoulder Angle

From Mellmann's work [15], applying tangential equilibrium of forces at the mill wall at the point of departure would yield:

$$Fr = \frac{\sin\ \kappa - \varphi_{\omega}}{\sin\ \varphi_{\omega}} \tag{130}$$

Using this model the particle deflection from the base of the mill up to the departure shoulder is given as:

$$\kappa = \varphi_{\omega} + \sin^{-1}\left[\sin\varphi_{\omega}\left(\frac{N}{N_c}\right)^2\right] \tag{132}$$

Where:

$$\varphi_{\omega} = \tan^{-1}\ \mu_w \tag{133}$$

This model yields a direct relationship between the operating mill speed and the total deflection of the charge from its original resting position to the departure shoulder. It is proposed that the model be further developed and tested against mill speeds used in PEPT experiments. Friction values can be read from the graph (such as figure 42) since it was plotted using the friction model, see equations (54) and (55). The total deflection (κ) would then give a good estimate of the expected departure point and hence the angular orientation of the mill tangential velocity at that point can be found. The departure velocity would be useful in the determination of particle kinetic energy at departure and hence the particle trajectory can be calculated.

9.1.4 Power Draw

In the previous chapter we outline the different approaches that have been proposed to quantify the power draft in industrial tumbling mills. Using the PEPT system it is possible to obtain charge trajectories in an appropriate coordinate system. These charge profiles are generally found to have longer paths when cataracting motion sets in. As mentioned in chapter eight, measured shaft power increased with speed. However, the continuum-based models outlined in the previous need experimental validation and possible further development.

9.2 Conclusion

Tumbling mills are utilised in almost all mineral processes where they are used in many different applications such as standard ball mills, autogeneous, semi-autogeneous grinding mills, and run-of-mine ball mills. These installations are

continuously required to process higher tonnages at higher efficiencies, which highlight the importance of optimal mill operation. Although the tumbling mill has been in use for many years, a fundamental and generic description of its operation is still lacking. This is largely due the difficulty of obtaining *in-situ* measurements from within the harsh mechanical environment inside an operating tumbling mill. Consequently most models are formulated from feed and discharge measurements and complimented with descriptions derived from environments dissimilar to that of the tumbling mill. Still, such empirical models can be tweaked to provide highly robust descriptions within the specific window of operation. However, they generally do not allow extrapolation beyond the modes of operation for which they were developed.

Researchers have long attempted to gain better understanding of tumbling mill operations and modelling by applying a range of techniques. These vary from industrial techniques (e.g. sampling campaigns of feed and discharge streams, crash stops and internal measurements, residence time studies, microphones, etc.), laboratory techniques (e.g. transparent mill charge motion, breakage studies), to computational simulations (e.g. single particle trajectory prediction, discrete element modelling (DEM)). However, none of these techniques can truly 'see' inside a realistic tumbling mill environment.

Fortunately, in recent years novel techniques like PEPT and X-ray imaging have allowed researchers an *in-situ* perspective of particle dynamics deep within the charge body. Both systems are specialised to provide 3D time-dependent trajectory fields, however, unlike the X-ray imaging system PEPT allows the use of real charge within a scaled industrial mill. It is thus the only tool capable of providing detailed kinematics histories of real rock and slurry.

Through the use of PEPT, detailed studies of charge motion and transport are now possible under a full range of conditions using rock or artificial charge within realistically scaled laboratory mills. The work described in this thesis is

focussed on the experimental program conducted at the PEPT unit at the University of Birmingham and at the iThemba LABS in Cape Town. The data derived from the particle tracking system spans a wide range of dry and wet milling configurations. The preliminary results are derived from the particle tracking of dry glass bead charge with sizes ranging from 2mm to 8mm within a 300mm x 270mm (D x L) mill.

The following conclusions are drawn from the research.

1. In chapters six and seven details of the transverse charge motion in tumbling mills are given. The chapters also provide theoretical understandings of the transition behaviour from one form of motion to the other. These descriptions, which consolidate the work of earlier researchers, fulfil the first objective (section 1.4.1) and present a number of new models.

2. The rate of circulation of the charge in a tumbling mill can be expressed as a function of mill operating parameters such as mill rotational speed, load fraction, charge angle of repose, departure shoulder angle and coefficient of friction, depicting near linear trends in most cases. This finding answers the first question in the key questions (section1.2.1)

3. While the rate of circulation of the charge was found to decrease with increasing mill speed and departure shoulder angle, it increased with increasing coefficient of friction indicating the effect of liner designs on circulation rates. This observation validates the first hypothesis (section 1.3.1) that discusses the relationship between circulation rates and mill speed as a percentage of critical.

4. Circulation rate of the charge in the experimental tumbling mill showed a non-linear trend with mill fraction of volume filling. This observation validates the second hypothesis (section 1.3.2) that discusses the relationship between circulation rates and mill load as a percentage of volume filling.

5. There is no perfectly keyed-in motion, even for the outermost layer of the charge and all layers of the charge, irrespective of the speed and lifter configuration, were found to slip relative to the mill.

6. Experimental results showed clear cascading motion at 60%, cataracting at 75% and partial centrifuging at 90% critical speed.

7. The circulation rate of the charge was found to be a maximum at the CoC but there was no observable trend between circulation rate and the CoM. Accurate determination of the charge geometric location is dependent on the angular location of the CoC – angle of repose - and the charge repose – the line joining the impact toe and departure shoulder. Experimental results show these features can have a linear relationship with the mill operational speed and thus these features have an indirect relationship with circulation rates of the charge.

8. In chapter seven (section) a model of circulation rate was presented and validated (see figure). This completes the third objective (section1.4.3) and serves as the main outcome of this thesis.

9. Mechanical motion resulting from drive shafts, push rods, or similar devices are known as driven flows.

10. These driven flows combined with friction or drag may lead to velocity gradients and hence viscous shear stress develop within the charge.

Thus the energy transferred to the grinding environment is distributed into mechanical energy gained by the circulating charge and energy losses in grinding. This finding answers the question in the key questions (section 1.2.2). It also validates the third hypothesis (section 1.3.3) and fulfills the fourth objective (section 1.4.4).

11. Hence conservation laws based on balances of mass, energy, momentum and angular momentum must be applied to better understand the nature of the distribution of energy in the grinding environment.

References

1. T. J. Napier-Mann, S. Morrel, R. D. Morrison and T. Kojovic. Mineral Comminution Circuits Their Operations and Optimization. *JKMRC monograph series in mining and mineral processing*. No 2 662.7 , 1996, pp160.

2. L. M. Tavares, and R. P. King. Single particle fracture under loading. *International Journal of Minerals. Processing*.54,. (1998), 1 – 28.

3. J. L. Salazar, L. Magne, G. Acuna, F. Cubillos. Dynamic modelling and simulation of semi-autogenous mills. *Minerals engineering*. 22 (2009) 70 – 77.

4. R.D. Morrison, P.W. Cleary. Towards a virtual comminution machine. *Minerals Engineering* 21, 11, (2008), 770-781.

5. H. Cho and L. G. Austin. An equation for breakage of particles under impact. *Powder Technology*. 132. (2003), 161-166.

6. I. Govender and M.S. Powell. Investigating SAG model assumptions using laboratory 3D trajectory data. SAG'06, Sep. 27 – Sep. 30, 2006, Vancouver, Canada. Ed. Barratt et al, Published.

7. U. Bock, K. Schonert. Charge motion model for vibrating mills with high excitation. *Powder technology*. 105 (1999) 311 – 320.

8. M. A. Van Nierop, N. H. Moys,. Axial mixing of slurry in an autogenous grinding mill. *International journal of mineral processing*. 56 (2002) 151 – 164.

9. Y. C. Zhou, A. B. Yu, R. L. Stewart, J. Bridgwater. Microdynamic analysis of the particle flow in a cylindrical bladed mixer. *Chemical engineering science* 59 (2004) 1343 – 1364.

10. J. Ling, P. V. Skudarnov, C, X. Lin, M. A. Ebadian. Numerical investigation of liquid-solid slurry flow in a fully

developed turbulent flow region. *International journal of heat and fluid flow - Elsevier*. 24 (2003) 389 – 398.

11. N. Khumalo, D. Glasser, D. Hildebrandt, B, Hausberger, S. Kauchali. The application of the attainable region analysis in comminution. *Chemical engineering science* 61 (2006) 5969 – 5980.

12. M. S. Powell and A. T. Mcbride. What is required from DEM simulations to model breakage in mills. *Minerals Engineering19 (2006) 1013 – 1021I.*

13. R. Byron Bird. 1957. The Equations of change and the macroscopic mass, momentum and energy balances. *Chemical Engineering Science.* Vol 6, Issue 3. Pp 123 – 131.

14. R. B. Bird, W. E. Stewart and E. N. Lightfoot. 1960. Transport Phenomena. New York: John Willey and Sons.

15. J. Mellmann. The transverse motion of solids in rotating cylinders – forms of motion and transition behavior. Powder technology 118 (2001) pp 251 – 270.

16. M. S. Powell, G. N. Nurick. A study of charge motion in rotary mills part I – extension of the theory. *Minerals engineering.* (1996), 9, 2, 259 – 268.

17. H. E. Rose and R. M. E. Sullivan, A treatise on the internal mechanics of ball, tube and rod mills, *Constable and Company*, London, pp. 35-69, 1958.

18. H. Watanabe. Critical rotation speed for ball-milling. *Powder technology.* Vol 104, (1999), 95 – 99 (5).

19. N. Taberlet, P. Richard and E. J. Hinch. The S-shape of a granular pile in a rotating drum. *Physical review*. Edition 73 (2006), pp. R050301-1 - 050301-4.

20. H. E. Cohen. Energy usage in mineral processing. *Transactions of the institution of mining and metallurgy*. Section C. Vol 92, pp. 160 – 163 (Sept 1983).

21. H. Y. Liu, S. Q. Kou, P. K. Lindqvist. Numerical studies on the inter-particle breakage of a confined particle assembly in rock crushing. *Mechanics of materials* 37 (2005) 935 – 954.

22. M. Yekeler, A. Ozkan, I. G. Austin. Kinetics of fine wet grinding in a laboratory ball mill. *Powder technology*. 114 (2001) 224 – 228.

23. I. Govender. X-ray motion analysis of charge particles in a laboratory mill. PhD thesis, Dept. of Mechanical Engineering, University of Cape Town, August 2005.

24. M. S. Powell and A. T. Mcbride. A three-dimensional analysis of media motion and grinding regions in mills. Minerals Engineering 17 (2004) pp 1099 – 1109.

25. P. R. Rittinger. Lehrbuch der aufbereitungskunde. Berlin (1867)

26. F. Kick. Das gasetz der proportionlen wilderstande und seine anwendung Felix-Verlag, Leipzig (1885).

27. F. C. Bond. The third theory of comminution. *Mining engineering 4, 484 – 494*.

28. K. Schonert. Fundamentals of particle breakage. *Course notes. Section F6. Division of continueing engineering education.* University of the Witwatersrand. Johanesburg. (1988).

29. E. T. Stamboliadis. The energy distribution theory of comminution specific surface energy, mill efficiency and distribution mode. *Mineral engineering*. Vol 20 (2007) 140 – 145.

30. B. Bohloli and E. Hoven. A laboratory and full scale study on the fragmentation of rocks. *Engineerng Geology*. Vol 89 (2007), pp. 1 – 8.

31. B. A. Wills. *Minerals processing technology* 5th edition. Pergamon press. Oxford (1992) pp. 855.

32. O. Tsoungui, D. Vallet, J-C. Charmet. Numerical model of crushing of grains inside two-dimensional granular materials. *Powder technology*. *Vol* 105, pp. 190 – 198.

33. R. A. Bearman, R. W. Barley, A. Hitchcock. Prediction of power consumption and product size in cone crushing. *Minerals engineering.* 4, No. 12, pp. 1243 – 1256 (1991).

34. C. Tangsathikulchai, L. G. Austin. The Effect of slurry density on breakage parameters on quartz, coal and copper ore in a laboratory ball mill. *Powder technology.* Vol 42 (1985) pp. 287 – 296.

35. R. M. Braun, J. Kolacz, D. I. Hoyer. Fine dry comminution of calcium carbonate in a Hicom mill with an improsys air classifier. *Minerals engineering.* Vol 15 (2002), pp.123 – 129.

36. L. G. Austin, K. Julianelli, A. S. De Souza, C. L. Schneider. Simulation of wet ball milling of iron ore at Carajas, Brazil. *International journal of mineral processing.* Vol 84, (2007), pp. 157 – 171.

37. N. L. Zhou. Experimental research on optimum operation of middle store parameter manufacturing system of the 300 MW unit. J. Shangai University Electrical Power. Vol 22, issue 3, 2006, pp. 217 – 220.

38. D. Y. Wu, H. Z. Sheng, X. L. Wei, L. X. Yu, H. C. Zhang. Optimized experiments on milling system for coal-fired boiler. *Proceedings of the CSME*. Vol 24, issue 12, 2004, pp. 218 – 221.

39. X. M. Zhang, X. H. Zhang. Determination of the load of all mill based on frequency spectrum analysis. Meas control Technology. Vol 19, issue 4, 2000, pp. 47 – 38.

40. H. Wang, M. Jia, P. Hon, Z. Chen. A study on a new algorithm to optimize ball mill system based on modeling and GA. Energy Conversion and Management. Vol 51, issue 4, April 2010, pp. 846 – 850.

41. A. R. Laplante, U. Prasad, R. E. Mclvor, J. A. Finch. Error analysis for bond work index determination part 2: a phenomenological basis for the analysis of systematic errors for the rod mill test. *Minerals Engineering.* Vol 6 issue 5 May 1996, pp. 509 – 521.

42. C. Hosten, c. Ozbay. A comparison of particle bed breakage and rod mill grinding with regard to mineral liberation and particle shape effects. *Minerals Engiineering.* Vol 11, issue 9, 1998, pp 871 – 874.

43. S. Morrell, G. Johnson, T. Revy. A comparison through observation and simulation of the power utilization performance of two dissimilar comminution plants. *Proceedings of Mill Operators Conference.* Burnie (AusIMM).

44. F. Concha, L. Magne, L. G. Austin. Optimization of the make-up ball charge in a grinding mill. *International journal of mineral processing* 34 (3), 231 – 241.

45. W. Valery Jr., S. Morell. The development of a dynamic model for autogenous and semi-atutogenous grinding. *Minerals engineering.* 8 (11) 1285 – 1297.

46. W. J. Whiten. A matrix theory for comminution machines. *Chemical engineering science.* 29 (1974) 585 – 599.

47. T. A. Apelt, S. P. Asprey, N. F. Thornhill. Inferenctial measurement of SAG mill parameters. *Minerals engineering.* 14 (6), 575 – 591.

48. T. A. Apelt, S. P. Asprey, N. F. Thornhill. Inferenctial measurement of SAG mill parameters II: state simulation. *Minerals engineering.* 15 (2002), 1043 – 1053.

49. T. A. Apelt, S. P. Asprey, N. F. Thornhill. Inferenctial measurement of SAG mill parameters III: Inferential models *Minerals engineering.* 15, (2002) 1055 – 1071.

50. O. Galan, G. Barton, J. Romagnoli. Robust control of SAG mills. *Powder technology.* 124, (2002) 264 – 271.

51. K. Leung. An energy based ore specific model for autogenous and semi-autogenous grinding mills. *Ph.D. Thesis*. The University of Queensland, Australia (1987)

52. J. L. Salazar, L. Magne, G. Titichoca, F. Cubillos, G. Acuna.XXXI ENEMP. Congreso Brasilelro de Sistemas Particulados, *Uberlandia*. Brazil. 24/27.

53. L. G. Austin. A mill power equation for SAG mills. *Minerals and metallurgical processing.*Vol 288 (1991) *57 – 62*.

54. S. Morrell. The prediction of power draw in wet tumbling mills. *Ph.D. Thesis*. The University of Queensland, Australia (1993).

55. P. W. Cleary, Predicting charge motion, power draw, segregation and wear in ball mills using discrete element methods, *Minerals Engineering*, vol. 11, no. 11, (1988) pp. 1061-1080.

56. M. S. Powell and A. T. Mcbride. A three-dimensional analysis of media motion and grinding regions in mills. Minerals Engineering 17 (2004) pp 1099 – 1109.

57. D. J. Parker, M. R. Hawkesworth, C. J. Broadbent, P. Fowles, T. D. Fryer, P. A. McNeil. Industrial positron-based imaging principles and applications. *Nuclear instruments and methods in physics research. . A* 348 (1994) 583 592.

58. I. Govender, R. Chandramohan, D. J. Parker, X. Fan, A. Ingram and M.S. Powell. Positron Emission Particle Tracking of charge particles in a scaled industrial tumbling mill.

59. R. J. Charles. Energy-size reduction relationship in comminution. Trans. AIME. Min. Eng. 208. (1957), 80 – 88.

60. O. R. Walton and R. L. Braun. Simulation of rotary drums and repose tests for frictional spheres and rigid sphere clusters. Joint DOE/NSF workshop on flow of particulates and fluids. Sept 29 – Oct 1, 1993. Ithaca, NY.

61. H. A. White. The theory of the tube mill. *The journal of chemical, metallurgical and mineral society of South Africa.* (1905) 290 – 305.

62. E. W. Davis. Fine crushing in ball mills. AIME *Transactions of the American Institute of Mining and Metallurgy Engineers.* . 61. (1919), 250 – 296.

63. R. E. Mclvor. Effects of speed and liner configuration on ball mill performance. *Mining engineering.* (1983) 617 – 622.

64. L. A. Vermeulen. The lifting action of lifter bars in in rotary mills. *Journal of South Africa institute of mining and metallurgy*. (1985), 65, 2, 51 – 63.

65. L. A. Vermeulen and D. D. Howat. Effects of lifter bars on the *en-masse* grinding media in milling. *International* j*ournal of mineral processing.*24, (1988), pp. 143 – 159.

66. L. Rolf, T. Vongluekiet. Measurement of energy distribution in ball mills. *Journal of Chemical engineering.*Vol 7, (1984), pp. 287 – 292.

67. S. Yashima, H. Hasimoto, Y. Kanda, S. Sano. Measurement of kinetic energy of grinding media in a tumbling ball mill. *Proceedings from the XVI international minerals processing congress.* Ed, E. Forsberg. Elsevier science publications. Amsterdam. (1988) 299 – 309.

68. Z. Rogovin, J. A. Herbst. Charge motion in a semi – autogenous grinding mill. *Minerals and metallurgical processing.* (1989) 18 – 22.

69. B. K. Mishra, R. K. Rajamani, W. G. Pariseau. Simulation of ball charge motion in ball mills. *Society of mining, metallurgy and exploration, inc.* Prep. (1990) 90 – 137.

70. D. Bachmann. Bewegungsvorgange in schwingmuhlen mit trockner mahlkorperfullung. VDI Beiheft verfahrenstechnik (1940) 2, 43 – 55.

71. J. T .Botz, C. Loudon, J. b. Barger, S. Jeffrey . D. W. Steeples. Effect of shape and particle size on ant locomotion;

implication for choice of substrate by antlions. *Journal of the Kansas Entomological Society.* Vol 6, Issue 3, pp. 426 – 435.

72. X. Zhao, Z. Yang, G. Gai, Y. Yang. Effect of superfine grinding on properties of ginger powder. Journal of Food Engineering. 91, 2, (2009), 217-222.

73. A. Santomaso, P. Lazzaro, P. Canu, Powder flowability and density ratios: the impact of granules packing, *Chemical Engineering Science* **58** (2003), 2857–2874.

74. K. E. Ileleji and B. Zhou, The ‹angle of repose› of bulk corn stover particles, *Powder Technology* (2008), 10, 1016.

75. H. J. Herrmann. Granular matter**.** Statistical Mechanics and its Applications. 313, 1-2, 1 (2002), 188-210.

76. P.G. De Gennes, Compaction of grains: a free volume model, *Physica.* A 244, 56 (1997).

77. Kevles, Bettyann Holtzmann. Naked to the Bone Medical Imaging in the Twentieth Century. *Rutgers University Press, Camden*, NJ. (1996). p19–22.

78. J. a. Bushberg, E. M. Leidholdt Jr, J. M. Boone. The essential physics of medical emaging (2nd edition). Lippincott Williams and Wilkins. 2001. ISBN 978-0-683-301 18-2.

79. M. S. Powell and G. N. Nurick, A Study of Charge Motion in Rotary Mills: Experimental Work, *Minerals Engineering*, vol. 9, no. 3, pp. 343-350, 1996.

80. M. S. Powell and G. N. Nurick, A Study of Charge Motion in Rotary Mills: Analysis of Results, *Minerals Engineering*, vol. 9, no. 4, pp. 399-418, 1996.

81. A. T. McBride, I. Govender, M. S. Powell and T. J. Cloete, Contributions to the experimental validation of the discrete element method applied to tumbling mills, *Engineering Computations*, vol. 21, no. 2/3/4, pp. 119-136, 2004.

82. M. E. Phelps, E.J. Hoffman, N.A. Mullani, M.M. Ter-Pogossian (March 1, 1975). Application of annihilation coincidence detection to transaxial reconstruction tomography. *Journal of Nuclear Medicine.* Vol 16 issoe 3 (1975) pp. 210–224.

83. E. A. van den Bergen and G. Jonkers, K. Strijickmans and P. Goethals. Industrial applications of positron emission computed tomography. *Internations journal of radial application instrumentation.* Vol 3, *sue 4* (1989), pp. 407 – 418.

84. S. Mirzadeh and R. Lambrecht. Radiochemistry of germanium. *Journal of radioanal nuclear chemistry*. 202, 7 (1996) 102.

85. J. Schuhmacher, H. Zhang, J. Doll, H. R. Macke, R. Matys, H. Hauser, et al. GRP receptor-targeted PET of a rat pancreas carcinoma xenograft in nude mice with a 68Ga-labeled bombesin (6-14). *Journal of nuclear medicine*. 46, (2005), 691 – 699.

86. G. T. Herman. Image Reconstruction from projections: The Fundamentals of Computational Tomography. *Medical physics* 9, 3 (1982) 446 – 448.

87. M. R. Hawkesworth, M. A. O'Dwyer, J. Walker, P. Fowles, J. Heritage, P. A. E. Stewart, R. C. Witcomb, J. E. Batemen, J. Connolly and R. Stephenson. Detector for gamma-rays. *Nuclear intruments and methods in Physics research.* A253 (1986) 145.

88. P. A. E. Stewart, J. D. Roges, R. T. Skelton, P. L. Salter, M. J. Allen, R. Parker, P. Davis, P. Fowles, M. R. Hawkesworth, M. A. O'Dwyer, J. Walker and R. Stephenson,. Non-desructive Testing. *Proceedings fo the 4th European Conference.* London, 1987. 4, pp 2718.

89. C. R. Bemrose, P. Fowles, M. R. Hawkesworth and M. A. O'Dwyer. An improved algorithm for tracking multiple, freely moving particles in a positron emission particle tracking system. *Nuclear instruments and methods.* A273 (1988) 874.

90. G. M. Field, J. Bridgewater, T. D eynon and J. S. M. Botterill. *Proceesings of the 2nd London conference on Position-Sensitive Detectors.* London, UK, (1990) p435.

91. T. J. Abott, M. J. Allen, P. Fowles, M. R. Hawkesworth, M. A. O'Dwyer, J. D. Rogers, P. L. Salter, R. T. Skelton, P. A. E. Stewart and J. Walker. Reliability of non-destructive testing. *Proceedings of the 27th Annual British Conference on NTD.* (1988). P 273.

92. M. R. Hawkesworth, C. R. Bemrose, P. Fowles and M. A. O'Dwyer. *Tomography and Scatter Imaging: Appiications in NDT.* IOP. Bristol. (1989) p 67.

93. M. R. Hawkesworth, D. J. Parker, P. Fowles, J. F. Crilly, N. L. Jetheries, G. Jonkers. Non-medical applications of a positron camera. *Nuclear intruments and methods in Physics research.* A310 (1991) 423 – 434.

94. D. J. Parker, C. J. Broadbent, P. Fowles, M. R. Hawkesworth and P. NcNeil. Positron emission particle tracking – a technique for studying flow within engineering equipment. *Nuclear instruments and methods in physics research*. A326 (1993) 592 – 607.

95. C. R. de Oliveira and T. Werlang. Ergodic hypothesis in classical statistical mechanics. Revista Brasileira de Ensino de fisica. 29, 2, (2007) p 189 – 201.

96. G. Bel and E. Barkai. Occupation times and ergodicity breaking in biased continuous time random walks. *Journal of physics: condensed matter.* 17 (2005) S42287 – S4304.

97. R. L. Jones. Ergodic theory and connections with analysis and probability. *New York journal of mathematics.* 3A (1997)31 – 67.

98. Dter Haar. Elements of statistical mechanics – third edition. *Butterworth-Heinemann, Oxford. Chapters 1 to 3*. 1995.

99. H. Dong and M. H. Moys. Assessment of discrete element method for one ball bouncing in a grinding mill. *International journal of mineral processing.* Col 65, issue 3 – 4, 2002, pp 213 – 226.

100. G. Baumann, I. M. Janosi and D. E. Wolf. Particle trajectories and segregation in a two-dimensional rotary kiln. *Europhysics letters.* 27, 3 (1994) 203 – 208.

101. A. Buffler, I. Govender, J. J. Cilliers, D. J. Parker, J. - P. Franzidis, A. Mainza, R. T. Newman, M. Powell, A. Van der Westhuizen, 2010. PEPT Cape Town: a new positron emission particle tracking facility at iThemba LABS. Proceedings of International Topical Meeting on Nuclear Research Applications and Utilization of Accelerators, 4-8 May 2009, Vienna (IAEA, Vienna, 2010). STI/PUB/1433, ISBN 978-92-0-150410-4, ISSN 1991-2374.

102. T. J. Spinks, T. Jones, P. M. Bloomfield, D. L. Bailey, M. Miller, D. Hogg, W. F. Jones, K. Vaigneur, J. Reed, J. Young, D. Newport, C. Moyers, M. E. Casey, R. Nutt, 2000. Physical characteristics of the ECAT EXACT3D positron tomography. Phys. Med. Biol. 45, 2601-2618.

103. A. M. Gow, A. B. Campbell and W. H. Coghill, A Laboratory Investigation of Ball Milling, *AIME Trans., Milling methods*, pp. 51-81, 1930.

104. A. W. Fahrenwald and H. E. Lee, Ball Mill Studies, *AIME Tech.* Publ. no. 375, 1931.

105. W. Barth, Power consumption in tube mills, *Forschung in Ingenierwesen*, vol. 1, no. 9, pp. 321-328, 1930.

106. M. S. Powell, *A Study of Charge Motion in Rotary Mills, with Particular Reference to the Grinding Action*. PhD thesis, Dept. of Mechanical Engineering, University of Cape, 1993.

107. M. J. Daniel. HPGR model verification and scale up. *Masters thesis, University of Queensland, Australia*. (2002).

108. M. J. Daniel and S. Morell. HPGR model verification and scale up. *Mierals engineering*. 17 (2004) 1149 – 1161.

109. B. K. Mishra and R. K. Rajamani, Simulation of Charge Motion in Ball Mills. Part 1: Experimental Verification, *International Journal of Mineral Processing*. vol. 40, pp. 171-197, 1994.

110. B. K. Mishra and R. K. Rajamani, Simulation of Charge Motion in Ball Mills. Part 2: Numerical Simulations, *International Journal of Mineral Processing*. vol. 40 (1984) pp. 171-197.

111. P. A. Cundall and O. D. L. Strack, A discrete numerical model for granular assemblies, *Geotechnique*, vol. 29, no. 1, pp. 47-65, 1979.

112. P. W. Cleary, Charge behavior and power consumption in ball mills: sensitivity to mill operating conditions, liner geometry and charge composition, *International Journal of Mineral Processing*, vol. 63, (2001) pp. 79-114.

113. P. W. Cleary, M. Sinnott and R. Morrison, Prediction of slurry transport in SAG mills using SPH fluid flow in a dynamic DEM based porous media, *Minerals Engineering*, vol. 19, Issue 15, (2006) pp. 1517-1527.

114. A. Acharya, *A discrete element approach to ball mill mechanics*, MSc thesis, University of Utah, 1991.

115. K. Sichalwe, I. Govender, A. N. Mainza. Characterizing porosity of multi-component mixtures in rotary mills. *Minerals Engineering*. 24, 2011, 276 – 281..

116. M. W. Frazier. *An introduction to wavelets through linear algebra*. Springer-Verlag, 1999..

117. E. M. Stein, G. Weiss. *Introduction to Fourier Analysis on Euclidean Spaces*. Princeton University Press. 1997. ISBN 0-691-08078-X

118. M. S. Powell. The Unified Comminution Model: A conceptually new model. Proceeding presented at *IMPC 2006 Conference*, Istanbul, Turkey, 3-8 September 2006

119. M. F. Beatty. Mathematical concepts and methods in science and engineering. *Principles of engineering mechnaics volume 2: Dynamics – The analysis of motion.* 33. Springer. ISBN 0-387-237048

120. K. R. Symon. Mechanics, second edition. *Addison-Wesley publications Co. Inc*. London, (1960) p158

121. H. Kutzbach and R. Sherer. Internal friction of cereal grain review. *Landtachnik.* 6 (1977) 213 - 219

122. E. Teunon, J. Vassuer and M. Krawczyk. Measurement and interpretation of bulk solids angle of repose for industrial process design. *Powder handling and processing.* 7, 3 (1995) 219 – 227

123. T. J. Clover. Pocket reference. 1998. *Littleton, Colorado.* Sequoia publishing inc

124. K. S. Liddell and M. H. Moys, -The effects of mill speed and filling on the behaviour of the load in a rotary grinding mill, *J.S.A. Inst. Min. Metall*., vol. 88, pp. 49-57, Feb. 1988

125. D. W. Fuerstenau, P. C. Kapur and B. A. Velamakanni, A multi-torque model for the effects of dispersants and slurry viscosity on ball milling, *International Journal of Mineral Processing*, vol. 28, pp. 81-98, 1990

126. R. Rutgers, Longitudinal mixing of granular material flowing through a rotating cylinder, *Chemical Engineering science*. 20 (1965) 1079 – 1087, 1089 – 1100

127. J. Leven. Indicators of grindability and grinding efficiency. *Journal of Southern African Institute of Minerals and Metallurgy.* Vol 92, issue 10, 1992, pp 283 – 290.

128. H. Henein, J. K. Brimacombe and A. P. Walkinson. Experimental study of transverse bed motion in rotary kilns. Metallurgy trans. B. 14B (1983) 191 – 220

129. M. Cross, The transverse motion of solids moving through rotary kilns, *Powder Technology.* 22 (1979) 187 – 190

130. S. Morrell, Prediction of grinding-mill power, *Trans. Inst. Min. Metall. (Section C: Mineral Process. Extr. Metall.)*, vol. 101, pp. C25-C32, 1992

131. P. W. Cleary and R. Morrison and S. Morrell, Comparison of DEM and experiment for a scale model SAG mill, *International Journal of Mineral Processing*, vol. 68, pp. 129-165, 2003

132. L. G. Austin, H. Cho. An equation for the breakage of particles under impact. Power technology 132 (2003) pp 161 – 166

133. S. S. Narayanan and W.J. Whiten, Determination of comminution characteristic from single particle breakage tests and its application to ball mill scale-up, *Trans. Inst. Min. Metall. (Sect. C)* **97** (1988), pp. C115–C124.

134. R. Kalra. Overview on alternative methods for fine and ultra-fine grinding. In: IIR Conference, Crushing & Grinding '99, Perth, 1999.

135. A. Kwade. Motion and stress intensity of grinding beads in a stirred media mill. Part2: Stress intensity and its effect on comminution. *Powder Technology* **86**, (1995), pp. 69–76.

136. R. Hogg, Breakage Mechanisms and mill performance in ultrafine grinding, *Powder Technology* **105** (1999), pp. 135–140.

137. R. Whyte. Measuring Incremental Damage in Rock Breakage by Impact Honours Thesis University of Queensland, Australia. 2005.

138. H. El-Shall, P. Somasundaran. Physico-Chemical Aspects of Grinding: a Review of Use of Additives. *Powder technology*. 38, 1984, pp 275 – 293.

139. R.P. King, Comminution research—a success story that has not yet ended, *Proceedings XVIII Int Min Proc Congress, Sydney, Publ. AUSIMM* **vol. 1** (1993), pp. 39–45.

140. L. S. Bbosa, I. Govender, A. N. Mainza, M. S. Powell. Power draw estimates in experimental tumbling mills using PEPT. *Minerals engineering.* Vol 24, issue 3 – 4, 2011, pp 319 – 324

141. D. V. V. Kallon, I. Govender, A. N. Mainza. Circulation rate modeling of mill charge using position emission particle tracking. *Minerals engineering.* Vol 24, issue 3-4, 2011.

142. R. Hogg, D. W. Feurstenau. Power relationships for tumbling mills. SME-AIMETrans 252, 1971, pp418 – 423.

143. C. C. HarisE. M. Scnock, N. Arbiter. Grinding mill power consumption. *Minerals processing technology*. Rev. 1. 1985. Pp 297 – 345

144. I. Govender, M. S. Powell. An empirical power model derived from 3D particle tracking experiments. *Minerals Engineering.* Vol 19. 2006. Pp 1005 – 1012

145. J. A. Harbst. A microscale look at tumbling mill scale-up using fidelity simulation. *International journal of minerals processing*. Vol 74, I (2004), pp. 299 – 306.

146. L. Tavares and R. Carvalho. A mechanistic model of batch grinding in ball mills. *Proceedings of the XXV International mineral congress (IMPC).* Brisbane, Queensland, Australia. 6 – 10 September, 2010.

147. E. Noether (1918). Invariante Variationsprobleme. *Nachr. D. König. Gesellsch. D. Wiss. Zu Göttingen, Math-phys. Klasse* **1918**: pp. 235–257.

Appendix A: Glossary

AoR: The angle of repose is simply defined as the maximum angle of a stable slope determined by friction, cohesion and shape of the particles.

Attenuation: Refers to the gradual loss of intensity when the emitted rays pass through material media.

Azimuthal angles of emission: This is the angle representing the orthogonal projection of the lines of response from the reference plane through the origin of coordinates in the PEPT system.

Beneficiation: This involves the various processes by which extracted ore are separated into valuable minerals and gangue.

Compton scattering: This is an inelastic scattering of the gamma ray photons by the annihilating electrons, which leads to loss of energy.

Deconvolution: This is a mathematical process employed to reverse the effect of convolution. Convolution itself is a mathematical operation performed on two separate functions to obtain a third function that may be identical to one of the two original functions. Hence the process that computes the inverse of convolution is generally known as deconvolution.

Diagnostic radiography: This is the use of both ionizing and non-ionizing radiations to create images for medical diagnosis.

Grindability: This is a measure of an ore's resistance to grinding.

Hardness: This is the resistance of ores to indentatino when subjected to external forces.

In-situ: This is the ability to examine phenomena exactly where it happens, that is within the grinding environment of the mill, without the need for invading the grinding environment or removing material for onward testing.

Mineral recovery: This is the process of separating commercially valuable minerals from their ores.

Line of sight: This is a line passing through the approximate tracer location and represents a possible line of propagation of the gamma ray photons emitted from the tracer.

Observation, Dependency and Agency: This is an approach to empirical modelling (EM) that allows the development of EM software. The modelling is based on empirical observations and dependency allows for development of dependency maintenance software tools.

Pelletizing: This is the process of molding materials into pellets, which are mostly small spheres. For instance iron ore pellets are spheres used as raw materials for blast furnaces.

Porosity: This is a measure of the void fraction (empty portion) of materials. It is measured as a percentage of voids over the entire volume.

Residence Time: This is defined simply as the amount of time a particle spends in a given system and is directly proportional to the amount of substance in the system.

Scintillations: The pulse of light produced by the ionizing events that affect transparent media (such as the acrylic used in the construction of the experimental mill).

Sintering: This is a process of creating solid objects using powders. The powders are made to fuse between the particles, at below melting point, forming compact solids.

Slurry: This is the fluid mixture formed by pulverized solids mixing with water and form the mill charge in wet runs.

Spatial resolution: This is a measure of how closely lines can be resolved in the PEPT camera system and is often affected by the system under study.

Toughness: Is defined as the amount of energy that a material can absorb during deformation without rupturing.

Triangulation: With a fixed base line the tracer location is determined by measuring angles to it from either points of this base line.

Appendix B: Nomenclature

Symbol	Comment	Symbol	Comment
$\boldsymbol{A}$	Cross-sectional area	$\boldsymbol{R_m}$	Radius to mill shell
$\boldsymbol{a}$	Charge acceleration	$\boldsymbol{r}$	Radial location
$\boldsymbol{Centx}$	x-cordinte of mill center	$\boldsymbol{r_i}$	Radial location of CoM
$\boldsymbol{Centy}$	y-cordinte of mill center	$\boldsymbol{S}$	Departure shoulder angle
$\boldsymbol{CoC}$	Center of circulation	$\boldsymbol{T}$	Impact toe angle
$\boldsymbol{CoM}$	Center of mass	$\boldsymbol{t}$	Time
$\boldsymbol{C_{charge}}$	Charge circulation rate	$\boldsymbol{V}$	Volume
$\boldsymbol{D}$	mill internal diameter	$\boldsymbol{v}$	Linear velocity
$\boldsymbol{d_m}$	Mean particle diameter	$\boldsymbol{W_w}$	Work done to overcome wall friction
$\boldsymbol{E_{loss}}$	Energy losses	$\boldsymbol{x_{CoC}}$	x-cordinate of CoC
F_c	Centrifugal force	$\boldsymbol{x_{CoM}}$	x-cordinate of CoM
F_F	Frictional force	$\boldsymbol{y_{CoC}}$	y-cordinate of CoC
F_g	Force of gravity	$\boldsymbol{y_{CoM}}$	y-cordinate of CoM
F_N	Normal force caused by friction	$\boldsymbol{z}$	z-cordinte in axial direction
$\boldsymbol{f}$	filling degree	$\boldsymbol{\alpha}$	Charge load fraction
$\boldsymbol{g}$	Acceleration due to gravity	ε	filling angle
$\boldsymbol{K}$	Total kinetic energy tensor	Δ	Delta
κ_m	Mean charge deflection	δ	Angle of repose
$\boldsymbol{k}$	Power law consistency factor	μ_i	Internal friction coefficient
$\boldsymbol{M}$	Charge mass condensed at CoM	μ_k	Coefficient of kinetic friction
$\boldsymbol{m_{tot}}$	Total mass of charge particles	μ_s	Coefficient of static friction
$N = n$	Mill rotational speed	$\boldsymbol{\mu_w}$	Wall friction coefficient
$N_c = \mathrm{n_c}$	Critical mill speed	ω	Angular velocity

$\boldsymbol{N_m}$	Mill speed	$\boldsymbol{\rho}$	Bulk density
N_o	Number of circulation counts	$\boldsymbol{\Omega}$	Mill rotational frequency
$\boldsymbol{P}$	Pressure	$\boldsymbol{\theta}$	Angular location
$\boldsymbol{P_{CoM}}$	Power drawn at the CoM	θ_c	Critical angle of repose
$\boldsymbol{P_{mech}}$	Mechanical power draw	$\boldsymbol{\theta_i}$	Angular location of the CoM
$\boldsymbol{P_{charge}}$	Charge power draw	$\boldsymbol{\tau}$	Stress tensor
$\boldsymbol{P_{loss}}$	Power losses	$\boldsymbol{\Phi}$	Total potential energy tensor
$\boldsymbol{R}$	Mill radius	$\boldsymbol{\zeta}$	Departure shoulder angle
$\boldsymbol{R_e}$	Radius to equilibrium surface	$\boldsymbol{\tau}$	Total potential energy tensor
$\boldsymbol{R_m}$	Radius to mill shell		

Appendix C: Data processing

In order to process the data from the PEPT experiments we developed matlab programmes that can be broadly divided into six sections.

I. Data access

As alluded to in chapter three data collected from PEPT experiments are stored in list mode on a computer and can be easily accessed for further processing. These files of raw PEPT data contain elements x, y, z, t, e, where t is the end time, e the error and x, y and z are Cartesian coordinates. The mill speed, in revolutions per minute, and the particular code (location) associated with each run must be manually edited in the file address before each run can be successfully loaded unto the programme.

II. Data streamlining

This stage involves preparation of data that was either a part of the experimental program or a direct result of the experiment. It essentially involves the following steps.

- Set mill speed,
- Set number of monitored particles,
- Set number of dimensions,
- Get mill centres in the PEPT camera coordinate system for the 300mm mill, slurry runs, glass beads and the X-ray mill,
- Set data as columns of values of t, x, y, z, e for all characters stepped by 2. That is, only even counts selected.

III. Generating the mill profile

As expected this section generates a front end view of the mill profile with a number of lifters depending on the dimensions of the laboratory mill used in the PEPT runs. The programme translates the mill centre to the origin of coordinates system and generates the mill profile from the X-ray mill shell. In the case of DEM simulation runs the compression ratio for the mill profile must be indicated.

IV. Generating the particle trajectory

This part is a bit tricky and further work is needed in this area with particular emphasis on determining the end point of each circulation as the end point of the particle trajectory is seen as not always monotonically increasing. In the present programme we implemented a smoothing spline to establish cycle behaviour for each circulation. This was done as follows.

- From data (x, y, z).
- Find CoC = (x_c, y_c).
- Translate mill centre (x_m, y_m) to (x_c, y_c) by using:
  - $x_1 = x_m - x_c$,
  - $y_1 = y_m - y_c$.
- Convert (x, y) to polar coordinates:
  - $R = \text{sqrt}(x^2 + y^2)$,
  - $\theta = y/x$.
- Find θ of first point as θ_1.
- Rotate all θ by θ_1:
  - ($\theta_{rot} = \theta - \theta_1$).

- Use the cycle behaviour of θ_{rot} to find the start and end points to each circulation.

We obtained a well behaved data for θ. If θ is seen monotonically increasing then this can be solved easily. However a more complicated case occurred in which θ is not monotonically increasing which required the following solution strategy to be implemented.

- Fit a smoothing spline to θ, using a very high smoothing factor,
- Find maximum and minimum points of smoothing spline,
- Then say we can find end points to circulation from the spline diagram,
- We noted that end points lie between consecutive minima and start points lie between consecutive maxima,
- Get any consecutive minima points as (m_1, m_2),
- Find all θ_{rot} between m_1 and m_2, as θ_{12} ,
- Then maxima of θ_{12} is end point.

Routine fails whenever the particle goes through the CoC, though the occurrence rate was not many at this stage. On closer examination it was observed that θ within a circulation is generally not monotonically increasing which makes it impossible to simply use the decrease in angular position to denote the end points to circulations. We believe further smoothing of the trajectory fields could minimize the occurrence rate. In order to solve this anomaly it may be necessary to construct a function that is monotonically increasing between the start and end points of each circulation and that may preserve the periodicity of the angular positions.

Other aspects related to this stage of the programme involved removing coordinates that fall outside the mill and this was carried out as follows.

- Find all radial positions less than the mill radius,

- Set zz equal to all radial positions less than the mill radius along the z-axis,
- Set yy equal to all radial positions less than the mill radius along the y-axis,
- Set xx equal to all radial positions less than the mill radius along the x-axis,
- Set tt equal to all radial positions less than the mill radius along the t-axis,
- Select data in specified chamber,
- Find all axial positions of the mill chamber along the x-axis.

The programme will plot mill trajectory data for all ball positions, showing the mill geometry profile and the number of tracked particles and produces a ball trajectory data line (line joining ball positions) in three dimensions. Using the coordinates of the location markers the charge could then be shifted back to into the mill.

V. Determining locations

The most important locations to be determined were the centre of mass (CoM) and the centre of circulation (CoC) described in this thesis. The centre of mass was determined simply as the mean of the ball positions in the x-y-z space. However, the CoC determination routine is more complex since it requires establishing three CoC locations each corresponding to the vertical, horizontal and radial equilibrium surfaces. In its simplest terms the programme will do the following.

- Set the number of CoC Domain Divisions to 100,
- Using ball position array illustrated in the previous section, mill radius, ball trajectory line and number of measured particles,

- Determine equilibrium mass flow points along each flow equilibrium surface and establish their values,
- Remove zeros from the mass flow points (when particle goes through CoC),
- Determine the three CoC positions along each flow equilibrium surface and establish their absolute count as CoC1, CoC2, CoC3,
- Find the combined CoC as the average of CoC1, CoC2 and CoC3.

Another way of finding the CoC location is to use the (ginput) function in matlab. It must be noted that this is user dependent.

VI. Calculations

This section uses the established data to implement some calculations involving the mill radius, number of measured particles, ball velocity and acceleration and the circulation rate values.

- The mill radius is the maximum z- position within the mill.
- The number of measured particles is equal to the row size of the data array.
- The ball velocity and accelerations are calculated using various finite differences and a Lagrange interpolation polynomial.
- Calculate circulation rate as per chapter five.